ANALYSIS OF THROMBI FROM ACUTE ISCHEMIC STROKE PATIENTS USING ADVANCED IMAGING TECHNIQUES

A Thesis Submitted to the College of
Graduate and Postdoctoral Studies
in Partial Fulfillment of the Requirements
for the Degree of Masters of Science
in the Department of Medicine (Dean's Office)
University of Saskatchewan
Saskatoon

By

VEDASHREE MEHER

PERMISSION TO USE

In presenting this thesis/dissertation in partial fulfillment of the requirements for a Postgraduate degree from the University of Saskatchewan, I agree that the Libraries of this University may make it freely available for inspection. I further agree that permission for copying of this thesis/dissertation in any manner, in whole or in part, for scholarly purposes may be granted by the professor or professors who supervised my thesis/dissertation work or, in their absence, by the Head of the Department or the Dean of the College in which my thesis work was done. It is understood that any copying or publication or use of this thesis/dissertation or parts thereof for financial gain shall not be allowed without my written permission. It is also understood that due recognition shall be given to me and to the University of Saskatchewan in any scholarly use which may be made of any material in my thesis/dissertation.

Requests for permission to copy or to make other uses of materials in this thesis/dissertation in whole or part should be addressed to:

Head of the College of Medicine (Deans' Office)
5D40 Health Sciences Building Box 19, 107 Wiggins Road
University of Saskatchewan
Saskatoon, Saskatchewan S7N 5E5
Canada

OR

Dean
College of Graduate and Postdoctoral Studies
University of Saskatchewan
116 Thorvaldson Building, 110 Science Place
Saskatoon, Saskatchewan S7N 5C9
Canada

DISCLAIMER

ABSTRACT

Background: Since cerebral thrombi are the proximate cause of acute ischemic stroke (AIS) and the primary target for current treatments, defining new thrombus characteristics associated with successful recanalization could help us improve treatment outcomes. We utilized Fourier-transform infrared spectroscopy (FTIR) and synchrotron-based X-ray fluorescence imaging (XFI) techniques, in combination with conventional histology and immunohistochemistry to analyze biochemical, elemental and histopathological composition of thrombi, respectively.

Methods: AIS patients who underwent endovascular therapy from September 2017 to January 2019 were recruited. One-half of all freshly retrieved thrombi were formalin-fixed paraffin embedded and stained with H&E, Masson's Trichrome, CD31, vWF and CD68 while the other halves were flash frozen in isopentane and analyzed using FTIR and XFI. Compositional findings were correlated with various clinical and interventional parameters collected prospectively, including National Institute of Health Stroke Scale (NIHSS), Thrombolysis in Cerebral Infarction (TICI) and modified Rankin Scale (mRS). Additionally, permeability to Isovue300 contrast agent was used as a biomarker to analyze thrombus perviousness.

Results: Twenty-eight patients were included. Retrospective analysis revealed that histological composition was not associated with pre-treatment NIHSS ($p = 0.19$), choice of thrombectomy

device ($p = 0.833$), 90-day mRS ($p = 0.892$) or 90-day NIHSS ($p = 0.512$). Additionally, stroke etiology did not alter histological composition of thrombi ($p = 0.437$). Patients in whom near-to-complete recanalization (TICI 2b-3) was achieved had thrombi composed of significantly higher proportions of erythrocytes than fibrin ($p = 0.01$). The choice of primary thrombectomy device, stentriever or aspiration, used during thrombus retrieval was not associated with recanalization outcomes ($p = 536$) or 90-day functional outcomes (mRS: $p = 0.363$; NIHSS: $p = 0.869$). XFI distribution maps demonstrated K and Fe to co-localize with erythrocytes; whereas, Ca and taurine to localize with fibrin. Lastly, measurement of thrombus permeability revealed that erythrocyte-rich thrombi were less pervious than fibrin-rich thrombi, and thrombus perviousness was associated with improved recanalization outcomes.

Conclusion: XFI has served as a novel technique to identify new markers involved in poor clinical outcomes. Characterizing thrombus composition, identifying targets, and correlating these findings with clinical information are key steps in improving our understanding of stroke treatment outcomes.

ACKNOWLEDGMENTS

I would like to thank all of my three supervisors: Dr. Roland Auer, Dr. Lissa Peeling, and Dr. Michael Kelly for encouraging me throughout the journey, and supporting me academically as well as financially. I owe gratitude to Dr. Valerie Verge (committee member) as well as Dr. Bogdan Popescu (committee chair) for their expertise and their helpful insights.

I would like to thank other team members including Dr. Jake Pushie, Nicole Sylvain, and Huishu Hou for mentoring me in several laboratory techniques as well as for providing me with continuous constructive feedback. I would also like to thank the clinical team members including Lilian Urroz, Sharleen Weese Maley, Ruth Whelan, Aaron Gardner, Aaron Huber, and Uzair

Ahmed for their guidance and support. In addition, I wholeheartedly thank Adi Manek, Anita Givens and other histotechnologists at the Saskatoon City Hospital pathology laboratory for their assistance with histology and immunohistochemistry techniques. I would like to thank the Canadian Lightsource Mid-IR beamline scientists, Stuart Read and Scott Rosendahl, as well as the Stanford Synchrotron Radiation Lightsource 10-2 and 14-3 beamline scientists, Sam Webb, Sharon Bone and Ross Arthur, for assisting me during beamtime and for helping me with data analysis.

Funding for this project is provided in part by the Saskatchewan Research Chair in Clinical Stroke Research, awarded to Dr. Michael E.B. Kelly. The Chair is funded by the Heart & Stroke Foundation, Saskatchewan; the Saskatchewan Health Research Foundation; and the University of Saskatchewan, College of Medicine. Funding for this project was also provided in part by the University of Saskatchewan's College of Medicine Research Award (CoMRAD), awarded to Dr. Lissa Peeling. Part of the research described in this thesis was performed at the Canadian Light Source, a national research facility of the University of Saskatchewan, which is supported by the Canada Foundation for Innovation (CFI), the Natural Sciences and Engineering Research Council (NSERC), the National Research Council (NRC), the Canadian Institutes of Health Research (CIHR), the Government of Saskatchewan, and the University of Saskatchewan. Use of the Stanford Synchrotron Radiation Lightsource, SLAC National Accelerator Laboratory, is supported by the U.S. Department of Energy, Office of Science, Office of Basic Energy Sciences under Contract No. DE-AC02-76SF00515. The SSRL Structural Molecular Biology Program is supported by the DOE Office of Biological and Environmental Research, and by the National Institutes of Health, National Institute of General Medical Sciences (P41GM103393). The

contents of this publication are solely the responsibility of the authors and do not necessarily represent the official views of NIGMS or NIH.

Finally, I would like to acknowledge my scholarships including the University of Saskatchewan, College of Medicine for awarding me a Health Sciences Scholarship, and a College of Medicine Graduate Student Award (CoMGRAD). The CoMGRAD was awarded in partnership with the James Regan Cardiology Research Award, for which I would like to express my sincere gratitude to the Reagan family.

PERMISSION TO REPRODUCE

DEDICATION

This dissertation is dedicated to my family and friends for their guidance and words of encouragement. I wholeheartedly thank my parents, Ravi Meher and Charu Meher, for instilling virtues of perseverance and commitment in me that have motivated me to strive for excellence. They are my role models who have served to inspire my hard work and determination. I owe special gratitude to my grandparents, my partner, Evan Dunlop, my sister, Swarali Meher, and my brother in-law, Waleed Raza for their love, endless support and patience. This achievement would not be possible without the support I have received from each one of them. I also dedicate this dissertation to my loving cats, Oreo and Rio for de-stressing me throughout my entire MSc journey and God for his guidance, and for providing me with the strength and power of mind.

TABLE OF CONTENTS

PERMISSION TO USE i
DISCLAIMER ii
ABSTRACT ii
ACKNOWLEDGMENTS …. iii
PERMISSION TO REPRODUCE v
DEDICATION v
TABLE OF CONTENTS vi
LIST OF TABLES viii
LIST OF FIGURES viii
LIST OF ABBREVIATIONS ix
Chapter One: General Introduction and Rationale 1
1.1 Stroke: brain infarct versus hemorrhage 1
1.2 Epidemiology and pathophysiology of stroke 6
1.3 Early work on thrombosis 7
1.3.1 Molecular mechanism: activation of the coagulation cascade and tissue factors 8
1.4 Current acute medical and surgical interventions for ischemic stroke 13
1.4.1 Tissue plasminogen activator 13
1.4.2 Endovascular Therapy 15
1.5 Importance of studying thrombus composition 23
1.6 Experimental imaging modalities for characterizing thrombi 26
1.6.1 Tissue preservation and fixation 26
1.7 Principles of histological stains and immunohistochemistry 29
1.7.1 Hematoxylin and Eosin Stain 30
1.7.2 Masson's Trichrome Stain 31
1.7.3 Chromogenic Immunohistochemistry 32
1.8 Principles of XFI 34
1.8.1 XFI beamline components 34
1.8.2 Sources of errors while quantifying samples using XFI 38
1.8.3 Benefits and limitations of Synchrotron-based XFI 39
1.9 Principles of Spectroscopy 40
1.9.1 X-ray absorption spectroscopy 40
1.9.2 Fourier-transform infrared spectroscopy (FTIR) – Mid Infrared spectroscopy beamline components 43

1.9.2.1 Globar versus Synchrotron source 46
1.10 Study goals, research questions, and hypothesis 46
Chapter Two: Methodology 48
2.1 Demographic and clinical characterization of patients 48
2.2 Acute intervention and mechanical thrombectomy procedure 50
2.2.1 Neurological examination and Stroke Score Assessment 50
2.2.1.1 NIHSS SCORE 50
2.2.1.2 ASPECTS SCORE 51
2.2.1.3 TICI SCORE 51
2.2.2 Endovascular therapy: thrombectomy procedure 52
2.2.3 Post-thrombectomy care and evaluation 53
2.3 Thrombus sample collection and processing 53
2.3.1 Paraffin embedding and sectioning 54
2.3.2 Flash freezing and cryosectioning 55
2.3.3 Histology 56
2.3.3.1 Hematoxylin and Eosin (H&E) – coverstainer process for paraffin sections 56
2.3.3.2 Masson's Trichrome – for paraffin sections 57
2.3.3.3 Hematoxylin and Eosin – manual process for frozen sections 58
2.3.3.4 Martius Scarlet Blue – manual process for frozen sections 58
2.3.4 DAB chromogen immunohistochemistry for paraffin sections 59
2.4 Histological analysis using ImageJ software 61
2.5 X-ray fluorescence imaging 64
2.5.1 10-2 beamline setup and data analysis tools 64
2.5.2 2-3 beamline setup and data analysis tools 67
2.5.3 14-3 beamline setup and data analysis tools 67
2.6 X-ray absorption spectroscopy 69
2.7 FTIR spectroscopic imaging 70
2.8 Statistical analysis 71
2.8.1 Use of parametric *versus* non-parametric tests 72
2.8.2 Statistical tests used in this study 75
Chapter Three: Results 79
3.1 Patient demographics 79
3.2 Histology results 81
3.2.1 Quantifying percent composition of erythrocytes and fibrin in thrombi 81
3.2.2 Distribution of erythrocytes, fibrin, platelets, endothelial cells, and macrophages 88

3.3 Correlations between clinical variables and thrombus composition 91
3.3.1 Assessing the effects of stroke etiology on thrombus composition 91
3.3.2 Accessing the effects of thrombus composition and occlusion location on stroke severity 92
3.3.3 Thrombus composition does not affect the choice of thrombectomy device used for achieving full recanalization. 95
3.3.4 Assessing the effects of thrombus composition, thrombectomy devices and recanalization status on 3-month functional outcomes 98
3.4 Correlations between elemental distribution, thrombus composition and clinical parameters . 103
3.4.1 XFI distribution maps 103
3.4.2 Spectroscopy: XAS and FTIR maps 107
3.4.3 Effects of stroke etiology on elemental composition and organic molecules in thrombi . 108
3.4.4 Effects of elemental composition and organic molecules on recanalization and 3-month functional outcomes 109
3.5 Thrombus perviousness 113
3.6 Summary of the results 115
Chapter Four: Discussion 118
4.1 Validity of classifying thrombi as red and white based on histopathology and etiology 119
4.2 Data trends and literature overview 123
4.3 Innovative contribution of this study 129
4.4 Limitations of this study 134
Conclusions and Future Direction 135
References 137

LIST OF TABLES

Table 1-1: Summary of tissue factors and enzymes of the coagulation cascade 13
Table 1-2: List of devices used in mechanical thrombectomy. 20
Table 1-3: Electromagnetic wave spectrum 35
Table 3-1: Patient demographics 80
Table 3-2: Raw data representing quantification of erythrocytes and fibrin 82
Table 3-3: Comparison between TICI and mRS scores. 101

LIST OF FIGURES

Figure 1-1: Computed Tomography Angiogram (CTA) 3
Figure 1-2: Cerebral angiography of arterial occlusion. 23
Figure 1-3: X-ray Fluorescence Imaging beamline components. 38

Figure 1-4: X-ray Absorption Spectroscopy beamline components. 42
Figure 2-1: Carotid Stenosis. 49
Figure 2-2: Flowchart of ImageJ analysis for histological quantification. 63
Figure 2-3: X-ray Fluorescence Imaging correlation plot 66
Figure 3-1: Histological examination of thrombi 90
Figure 3-2: Correlation between stroke etiology and thrombus composition 92
Figure 3-3: Correlation between stroke severity and thrombus composition. 94
Figure 3-4: Correlation between thrombus composition, EVT device choice and recanalization Success. 97
Figure 3-5: Correlation between the effects of various clinical parameters on 3-Month functional outcomes. 100
Figure 3-6: Correlation between procedural and functional outcomes. 102
Figure 3-7: Correlation between histological and elemental composition. 103
Figure 3-8: XFI elemental distribution pseudo coloured maps. 105
Figure 3-9: Bl 14-3 XFI maps representing low Z elements. 106
Figure 3-10: Bl 14-3 XFI sulfur distribution pseudo coloured map 106
Figure 3-11: Fe Spectroscopy 107
Figure 3-12: FTIR distribution map. 108
Figure 3-13: Correlating the effects of stroke etiology on elements and organic molecules. 109
Figure 3-14: Correlating elemental with clinical outcomes. 111
Figure 3-15: Correlating biochemical composition with clinical outcomes. 113
Figure 3-16: Effects of thrombus perviousness on clinical outcomes. 114

LIST OF ABBREVIATIONS

Alphabetical
A
AIS – Acute Ischemic Stroke
ACA – Anterior Cerebral Artery
ADAPT – A Direct Aspiration First Pass Technique
Ar (element) – Argon
ASPECTS – Alberta Stroke Program Early Computed Tomography Score
A.U – Absorbance Units
B
BA – Blooming Artifact
Bio-RED – Biomedical Research Ethics
BL – Beamline
Br – Bromine
C
Ca (element) – Calcium
Ca^{2+} or Ca^{++} – Ionized Calcium
Cl (element) – Chlorine
CCA – Common Carotid Artery
CD31 – antibody against endothelial cells
CD68 – antibody against macrophages
CLS – Canadian Light source

CT – Computed Tomography
CTA – Computed Tomography Angiogram
CuS (molecule) – Copper Sulfate
D
DAB – 3, 3'-Diaminobenzidine
DAWN – Diffusion Weighted Imaging or Computerized Tomography Perfusion Assessment With Clinical Mismatch in the Triage of Wake Up and Late Presenting Strokes Undergoing Neurointervention With Trevo
E
ECA – External Carotid Artery
EDTA – Ethylenediaminetetraacetic acid
ESCAPE – Emphasis on minimizing CT to recanalization times
EVT – Endovascular therapy
EXAFS – Extended X-ray Absorption Fine Structure
EXTEND-IA – Extending the time for Thrombolysis in Emergency Neurological Deficits with Intra-Arterial therapy
F
FDA **–** Food and Drug Administration
Fe (element) – Iron
FPA – Focal Plane Array
FTIR – Fourier transform Infrared Spectroscopy
H
H&E – Hematoxylin and Eosin
HCl – Hydrochloric Acid
He-Ne – Helium Neon
HIER – Heat Induced Epitope Retrieval
HMCAS – Hyperdense Middle Cerebral Artery Signs
HRP – Horseradish Peroxidase
HU – Hounsfield Units
I
IA-tPA – intraarterial tissue plasminogen activator
I (element) – Iodine
ICA – Internal Carotid Artery
ICH – Intracranial Hemorrhages
ICPMS – Inductively coupled plasma mass spectrometry
ID – Internal Diameter
IMS – Interventional Management of Stroke
IQR – Interquartile Range
IV-tPA – intravenous tissue plasminogen activator
G
GaP (molecule) – Gallium Phosphate
GUI – Graphical User Interface
K
K (element) – Potassium
KBr – Potassium Bromide

KCl – Potassium Chloride
L
LAA – Large Artery Atherosclerosis
LVO – Large Vessel Occlusion
M
MCA – Middle Cerebral Artery
MERCI – Mechanical Embolus Removal in Cerebral Ischemia
MRI – Magnetic Resonance Imaging
mRS - Modified Rankin Scale
MR CLEAN – Multicentre Randomized Control Trial for Endovascular Treatment for Acute Ischemic Stroke in Netherlands
MR RESCUE – Mechanical Retrieval and Recanalization of Stroke Thrombus using Embolectomy
MSB – Martius Scarlet Blue
MT – Masson's Trichrome
MW – Molecular Weight
N
NaN – Not a Number
NCCT – Non-contrast Computed Tomography
NECT – Non-enhanced Computed Tomography
NIHSS – National Institute of Health Stroke Scale
NIST – National Institute of Standards and Technology
O
OCT – Optimal Cutting Temperature
OD – Outer Diameter
P
P(element) – Phosphorous
PAR-1 – Protease activated receptor-1
PBS – Phosphate Buffered Saline
PCA – Posterior Cerebral Artery
PIER – Proteolytic Induced Epitope Retrieval
PIPS – Passivated Implanted Planar Silicon
PFA – paraformaldehyde
PROACT – Prolyse in Acute Cerebral thromboembolism
PSGL – P-selectin glycoprotein ligand
R
RbI (molecule) – Rubidium Iodide
RBC – Red Blood Cells
RCT – Randomized Controlled Trial
REVASCAT – Endovascular Revascularization With Solitaire Device Versus Best Medical Therapy in Anterior Circulation Stroke Within 8 Hours
RF – Radio frequency
ROI – Region of Interest
rtPA – recombinant tissue plasminogen activator
RUH – Royal University Hospital

S
S (element) – Sulfur
SD – Standard Deviation
SEM – Standard Error of Mean
Si (element) – Silicone
SAH – Subarachnoid Hemorrhage
SMAK – Sam's Microprobe Analysis Kit
SSRL – Stanford Synchrotron Radiation Lightsource
SWIFT – Solitaire with the Intention for Thrombectomy
SYNTHESIS – Systemic Thrombolysis for Acute Ischemic Stroke
T
TFPI – Tissue Factor Plasminogen Inhibitor
TICI – Thrombolysis in Cerebral Infarction
TIME – Thrombectomy in Middle Cerebral Artery Embolism
TNK – Tenectaplase
TOAST - Trial of Org 10172 in Acute Stroke Treatment
TREVO – Thrombectomy Revascularization of large vessel occlusion in acute ischemic stroke
TWS – Trainable WEKA Segmentation
V
vWF – von Willebrand Factor (antibody against platelets)
X
XANES – X-ray Absorption Near Edge Spectra
XAS – X-ray Absorption Spectroscopy
XFI – X-ray Fluorescence imaging
Z
Zn (element) – Zinc
ZnTe (molecule) – Zinc Telluride
Symbols
Absorbance – A
Absorptivity – ε
Arial Concentration – $\mu g/cm^2$
Concentration – c
Correlation coefficient – r
Degree Celsius – °C
Electronvolt – eV, gigaelectronvolt – GeV, megaelectronvolt – MeV
French – F
Gamma – γ
Hertz – Hz
Kilodalton – kDa
Milliradian – mrad
Microgram – μg, Micrometer – μm, Centimeter – cm
Phi – Φ
Probability value – p-value
Sample Size – n

Tissue thickness - l
Wavenumber – cm^{-1}

Chapter One: General Introduction and Rationale

1.1 Stroke: brain infarct *versus* hemorrhage

The brain serves as the hub of the nervous system in all vertebrate animals. The physiological function of the brain is to exert centralized control over all the organs to maintain homeostasis and behaviour via neurotransmitters and hormones [1]. Perception, motor functions of voluntary and involuntary muscles, arousal, motivation, coordination of breathing, blood circulation and heart rate, learning, and memory are just few of the many functions controlled by the brain. Broadly speaking, each of these functions are controlled by specific parts of the brain, including; frontal lobe, parietal lobe, temporal lobe, occipital lobe, cerebellum, and brainstem [1]. As the brain has a high metabolic rate, it receives approximately 15-20% of the total cardiac output [2], making it the body's most highly perfused and metabolically demanding organ [3]. The brain is the only organ that exclusively relies on the oxidative metabolism of glucose for its energy and function [4], and thus requires a high but constant blood flow.

Blood circulates through two parallel loops: pulmonary circuit and the systemic circuit [1]. In the pulmonary circuit, blood is transported between the heart and the lungs whereas in the systemic circuit, blood is transported between the heart and other tissues. In the systemic circuit, oxygen-rich blood flows from arteries branching off the heart and aorta into arterioles and then into capillaries where nutrients and oxygen diffuse into the surrounding tissue. Capillary beds generally connect arterioles to venules which then carry deoxygenated blood into the veins to drain it into the superior or inferior vena cavae of the heart. However, in the venous portal system, one capillary bed pools into another capillary bed before draining the venous circulation into the heart. Two such venous portal systems include the hypophyseal portal system and the hepatic portal system [1]. The hypophyseal portal system interconnects the hypothalamus and

adenohypophysis for the delivery of releasing and inhibiting hormones that stimulate and inhibit the anterior pituitary gland, respectively. Whereas, in the hepatic portal system, blood leaving the capillary beds of splenic, superior mesenteric and inferior mesenteric veins are drained into the hepatic portal system instead of directly travelling into the inferior vena cava. This ensures nutrient absorption, maintenance of nutrient balance and detoxification before the blood enters general circulation [1].

All blood vessels except capillaries, are made up of three histological layers. The outermost layer of the vessel is called tunica adventitia and is composed of connective tissue to provide integrity, support and shape to the vessel. The middle layer is called tunica media and is primarily composed of elastic fibres and smooth muscle cells to regulate vessel diameter (*i.e.* wall thickness) and carry out the functions of vasodilation or vasoconstriction. The smooth muscle layer varies in inverse proportion to the elastic tissue, depending on the size of the vessel. Thus, larger vessels have more elastic tissue and less smooth muscle to accommodate high pressure and shear stress as opposed to smaller vessels that diffuse into an organ and tend to have less elastic tissue and more smooth muscle cells. And lastly, the innermost layer is called tunica intima and is primarily composed of endothelial cell surface which lies on basal lamina [5].

The arterial supply to the cerebral hemispheres is derived from anterior and posterior circulations supplied by internal carotid arteries (arising from common carotid artery) and vertebral arteries (arising from subclavian artery), respectively [6]. The right common carotid artery originates from the brachiocephalic trunk off the aorta, while the left carotid artery originates directly from the aorta. Both common carotid arteries bifurcate into an internal carotid artery (ICA) and external carotid artery (ECA) **(Fig. 1-1)**.

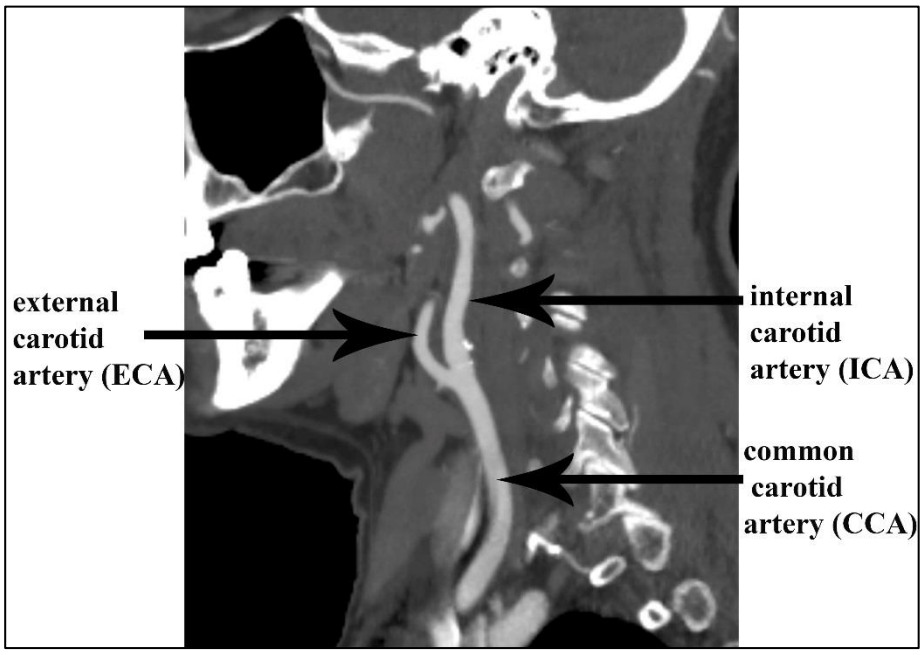

Figure 1-1: Computed Tomography Angiogram (CTA) CTA of the common carotid artery (CCA) bifurcating into the internal carotid artery (ICA) and external carotid artery (ECA).

Anterior and posterior circulations meet at the circle of Willis, an anastomotic ring from which all other major cerebral vessels arise, to supply the brain. The terminal branches of the ICA include the middle cerebral arteries (MCA) and anterior cerebral artery (ACA), where ACA are cross-connected via the anterior communicating artery. The ICA anastomoses with posterior cerebral artery (PCA) via the posterior communicating artery [6]. The posterior cerebral arteries form the posterior circulation by branching off the top of the basilar artery, which is itself formed by the only arterial confluence in the body, where left and right vertebral arteries meet and join anterior to the medulla oblongata [7]. The basilar artery gives rise to many branches including the superior cerebellar arteries, pontine arteries, and the anterior inferior cerebellar artery while each of the vertebral arteries branch into the posterior inferior cerebellar artery and contribute to the formation of a single anterior spinal artery.

The three main cerebral arteries (MCA, ACA and PCA) give rise to several small branches that supply deep structures of the brain [6]. The ACA supplies the anterior part of the brain, externally spanning from frontal to anterior parietal lobes. Deep structures supplied by the ACA

branches include: anterior segments of caudate nucleus, putamen and globus pallidus, anterior limb of the internal capsule, uncinate fasciculus, dorsal surface of the optic nerve, optic chiasm and optic tract, corpus callosum (rostral end), basal surface of the frontal lobe, pre-central, central and post-central gyrus [8]. The MCA supplies the lateral surface of the frontal and temporal lobes, portions of the parietal lobes and the insula. Deep structures supplied by the MCA branches include basal ganglia and internal capsule [6]. PCA supplies inferior and medial portions of the temporal and occipital lobes. Deep structures supplied by the PCA branches include: thalamus and posterior limb of the internal capsule [6].

The circle of Willis is arranged in a manner to create redundancy and generate abundant opportunities for collateral circulation to help perfuse the brain and obviate tissue death after a traumatic brain injury or during states of acute or chronic ischemia. Sometimes, even when the brain lesion persists, the tissue around the core of the infarct, known as the penumbra, is still salvageable and has the ability to recover. However, once the infarcted tissue dies, the tissue can no longer recover in function. Occlusions of the MCA or ICA can have severe clinical impacts. Some people have poor collaterals or incomplete circle of Willis while others have good functional collaterals. Thus, asymptomatic occlusions of the MCA or ICA vessels could be attributed to functional collaterals or built-in redundancy. Collateral circulation routes can be divided into primary and secondary pathways, wherein primary collaterals include communicating arteries while the secondary collaterals include the ophthalmic and leptomeningeal arteries.

As longevity has increased, cardiovascular and cerebrovascular diseases have now become the leading causes of death [9]. Stroke is a clinical syndrome, so-named due to the sudden onset of symptoms. It can be a consequence of ischemia, reduced blood supply, oxygen and nutrients to

the brain, leading to tissue death, termed necrosis. There are only two major classes of brain strokes; hemorrhagic and ischemic. In hemorrhagic stroke, arteries burst either due to aneurysms, weakened vessel walls or arteriovenous malformations, and bleed into or around the brain to cause swelling and increased intracranial pressure. In subarachnoid hemorrhages (SAH) blood leaks into the subarachnoid space either caused by a head trauma or rupture of an intracranial aneurysm whereas in intracerebral hemorrhages blood leaks directly into the brain, and can be due to an array of diseases including hypertensive arteriolosclerosis, amyloid angiopathy (primary hemorrhage) or arteriovenous malformations, aneurysms, neoplasia, cavernous angioma or coagulopathies (secondary hemorrhage) [10], [11]. On the other hand, ischemic strokes are caused by occluded vessels, either from a thrombus or embolus. When blood clots are formed *in situ*, in one of the intracranial arteries of the circle of Willis, the ischemic stroke is categorized as a thrombotic stroke and the blood clot is referred to as a thrombus [12]. If a blood clot forms elsewhere, and then migrates into the cerebral vasculature to block one of the vessels in the brain, the ischemic stroke is categorized as an embolic stroke and the blocking substance is referred to as an embolus [12].

Because each side of the brain controls the opposite side of the body, occlusions (thrombotic or embolic) in arteries supplying the left hemisphere result in right-sided deficits, while occlusions in arteries supplying the right hemisphere result in left-sided deficits. Deficits caused by ACA occlusions may include leg weakness, primitive grasp reflex and paratonic rigidity, gait apraxia, and partial frontal lobe behavioural abnormalities. MCA occlusions may present as face and arm weakness, hemiplegia, hemianesthesia, homonymous hemianopia, global aphasia, change in gaze preference, visual field and somatosensory deficits, motor hemiparesis, aphasia (speech difficulty caused by left MCA occlusions), and profound hemineglect (caused by right MCA occlusions).

PCA occlusions may present as homonymous hemianopia, hemisensory loss, memory loss, hemiparesis [6], alexia without agraphia, and prosopagnosia which is characterized by the inability to recognize faces.

1.2 Epidemiology and pathophysiology of stroke

Stroke is the second leading cause of death in the world, affecting approximately 33 million people world-wide each year [13]. Ischemic strokes account for approximately 87% of all stroke types, while intracranial hemorrhages (ICH) account for 10% and subarachnoid hemorrhages account for 3% of all stroke types [14]. However, as the lesion caused by hemorrhage is usually 20× bigger than the lesion caused by ischemia [15], hemorrhagic strokes result in higher mortalities than ischemic strokes [16]. In 2013, the prevalence of stroke in Canada was 1.15% wherein 405,000 Canadians were affected [17]. The incidence of first stroke is higher in men than women. Nevertheless, more women are afflicted by stroke than men each year [18]. An international, multicenter, case-control study that recruited participants from 22 countries showed that there are 10 common risk factors for stroke, including hypertension – the most prominent risk factor, diabetes, smoking, abdominal obesity, hyperlipidemia, lack of physical activity, alcohol consumption, poor diet, and psychological stress [19].

Ischemic arterial strokes are almost universally caused by embolism as opposed to *in situ* thrombosis. A system for categorizing ischemic stroke subtypes based on etiology has been developed for the Trial of Org 10172 in Acute Stroke Treatment (TOAST). TOAST classifies stroke etiology into five subtypes: 1) cardioembolism, 2) large artery atherosclerosis (LAA), 3) small vessel occlusion, 4) etiology of other determined cause (*e.g.* dissection), and 5) etiology of cryptogenic or undetermined cause [20]. However, emboli that travel to the brain almost always arise from either the heart (cardioembolism) or from the carotid artery bifurcation (artery-to-

artery embolism) [21]. Cardiac emboli arise due to: 1) cardiomyopathies such as hypokinetic or akinetic ventricles, atrial septal aneurysms, and atrial myxomas; or 2) valve disorders such as rheumatic mitral and aortic valve disease, bacterial endocarditis, fibrous/fibrinous endocardial lesions, and mitral annulus calcification; or 3) irregular heartbeats caused by atrial fibrillation [22]. Large artery atherosclerosis usually caused by plaque deposits composed of cholesterol, fat, and calcium, can lead to artery-to-artery emboli. Other less common embolic agents include air bubbles, cancerous cells, or infectious debris [23]. Cardiac-emboli have the highest rates of recurrence and in-hospital mortality [24], [25].

A systemic analysis indicated that there were 80 million stroke survivors in 2016 around the world [26]. Approximately 45% of these survivors are affected by long-term devastating physical disabilities [27] with an additional likelihood of one-third of the patients developing depression or other mental illnesses [18]. It is therefore not only important to determine risk factors and preventive measures for ischemic stroke but it is also important to investigate ways to improve post-stroke clinical outcomes that minimize impairments and disabilities.

1.3 Early work on thrombosis

Jean Cruveilhier, an eminent anatomist of the 19th century proposed that thrombosis occurred *de novo* as a consequence of vessel wall inflammation [28]. However, his contemporary, Rudolf Virchow conducted experiments to demonstrate that inflammation was indeed a secondary phenomenon to thrombosis and that thrombi (specifically in pulmonary embolism) travelled from venous circulation as opposed to *in situ* formation. Virchow was the first to coin the terms thrombosis and embolism. In an experiment, Virchow injected foreign objects (*i.e.* seeds, berries and coagulated blood) in the jugular vein of dogs and observed that the object was transported from peripheral circulation to the lung vasculature. He then attributed the occurrence of

obstruction to: 1) irritation to the vessels and its surroundings; 2) blood coagulation; and 3) interruption of blood stream [28], [29]. Virchow's findings that are now recognized as Virchow's triad describe the three factors (*i.e.* vessel wall damage, hypercoagulability and stasis) that contribute to the development of thrombosis and the conditions required for thrombus propagation. Even though Virchow's work referred to venous thrombosis, the same processes can be applied to arterial thrombosis [30].

1.3.1 Molecular mechanism: activation of the coagulation cascade and tissue factors

Formation of a thrombus is a natural physiological response when blood vessels are injured either by external or internal trauma that expose the endothelial surface [31]. When this happens, the site of vascular injury accumulates platelets and fibrin to form a thrombus and prevent further blood loss. However, thrombus formation does not always occur as a result of a vascular injury. For instance, patients with atrial fibrillation might suffer an ischemic stroke from thrombosis caused by either blood stasis or inherent hypercoagulability. Hemostasis is a process where thrombi are formed via a "platelet – plug" after a tissue injury to stop the bleeding [32]. During hemostasis, the initial platelet plug is formed by an interaction between platelets, the endothelium, tissue factors and leukocytes [31]. Hemostasis is defined in two phases: 1) primary hemostasis which involves the activation, adhesion, secretion, and aggregation of platelets [33], and 2) secondary hemostasis which is defined by the assembly of coagulation tissue factors which cleave fibrinogen into its activate form – fibrin [32]. Platelets, also known as thrombocytes are colourless, non-nucleated, disc-shaped cells that arise by differentiation from megakaryocytes [33] and were first discovered in 1866 by Giulio Bizzozero [34]. In response to a vascular injury, platelets interact with the subendothelial layer, the basal lamina or basement membrane, present under the tunica intima layer of the vessel wall. Platelets then undergo

morphological changes [refer to *section 1.1* for information on vessel wall structure]. The subendothelial layer contains collagen, von Willebrand factor (vWF), laminin, vitronectin and other adhesive proteins [32]. Vitronectin and vWF are also generated from platelet granules. Vitronectin mediates platelet adhesion and binds to plasminogen activator inhibitor to stabilize the formed thrombus and prevent it from undergoing lysis [35]. Platelet adhesion depends on shear stress in the circulation. Platelets adhere to collagen via vWF, a glycoprotein and carrier protein for factor VIII which is released by endothelial cells and deposited in the subendothelial layer during high shear stress, which further activates other cell adhesion molecules on platelets and integrins. Activated integrin receptors enable binding of fibrinogen, sustain platelet-platelet aggregation and adhere to vitronectin [36]. Platelet adhesion to collagen enables platelet granules to secret proteins that further sustain hemostasis [31]. There are two types of platelet granules: alpha granules and delta granules (dense granules). Alpha granules of platelets contain P-selectin, fibrinogen, labile tissue factors V and VIII, vWF, other angiogenic, anti-angiogenic and growth factors while dense granules essentially contain ATP, ADP, ionized Ca^{++} (factor IV), and serotonin [37], [38]. Platelets also contain cyclooxygenase that converts arachidonic acid into thromboxane A2 which enables vasoconstriction during a vascular insult and also mediates binding of the ADP molecules to the receptors of other circulating platelets to aid in platelet-platelet aggregation [39]. While platelets are the key players during hemostasis, the recruitment of other types of blood cells is also important for amplifying this process. For instance, under hypoxic conditions P-selectin secreted from platelets interacts with the P-selectin glycoprotein ligand 1 (PSGL-1) receptor present on neutrophils, monocytes and leukocytes, and recruit them to the injury site [36]. In addition, platelets also interact with endothelial cells under

inflammatory response. Calcium secreted by the dense granules, binds to the endothelial phospholipids and mediates the assembly of coagulation tissue factors for secondary hemostasis.

Secondary hemostasis involves the activation of the coagulation cascade. According to traditional classification, the coagulation cascade is divided into two pathways: the intrinsic pathway which is activated by an internal trauma and the extrinsic pathway which is activated by an external trauma that allows blood to escape from vessels (*eg.* skin abrasion). A balance between clotting and bleeding is maintained by interactions within coagulation (thrombus formation) and fibrinolytic (thrombus degradation) systems [31]. The coagulation system contains clotting factors which are precursors of proteolytic enzymes, known as zymogens (*i.e.* enzyme generators) that circulate in an inactive form in the blood until the intrinsic or the extrinsic pathways are activated [39]. An activated zymogen is denoted with the letter "a" [31]. Activation of the intrinsic pathway begins with the activation of tissue factor XII into XIIa, and downstream factors XI and IX while activation of the extrinsic pathway begins with the activation of tissue factors VII and VIII. Activation of factor XI into XIa is catalyzed by XIIa and the activation of IX into IXa is catalyzed by XIa. Both of these pathways converge into the common pathway where tissue factor X is activated into Xa by tenase complex involving catalyzing proteins IXa, VIIa and VIIIa. Factor Xa and Va form a prothrombinase complex and catalyze the conversion of prothrombin (factor II) into thrombin (factor IIa) enabling the assembly of other substrates. Thrombin cleaves arginine-lysine bonds in fibrinogen, thereby converting it to its active form – fibrin [39]. Fibrin polymerizes into a cross-linked fibrin thrombus with the help of factor XIIIa (fibrin stabilizing factor) which determines the stability of the thrombus. Table 1-1 summarizes all the tissue factors involved in the coagulation cascade.

Activated thrombin has several downstream targets. Thrombin amplifies the activation of factors V, VIII and IX via a positive feedback loop. Thrombin induces inflammation by mobilizing P-selectin and producing chemokines, cytokines, cyclooxygenase-2 and prostaglandins, and enables the expression of endothelial adhesion molecules to allow leukocyte recruitment [39], [40]. Thrombin also cleaves protease activated receptor-1 (PAR-1) to further stimulate platelet activation, secretion and aggregation [41]. Activation of tissue factors by tissue factor catalyzing enzymes require platelet-dependent calcium ions (tissue factor IV). In response to thrombin and collagen, platelet activation causes externalization of phosphatidylserines in the phospholipid bilayer of platelets resulting in Ca^{++} ion production and generation of phosphatidylserine microvesicles which contain thrombogenic factors important for sustaining the coagulation cascade. Ca^{++} is also involved in stabilizing factor VIII by linking protein chains within the tissue factor as well as anchoring the protein chains to vWF. Ca^{++} also acts as a linker when tenase and prothrombinase complexes are formed where serine proteases of the tissue factors are linked to the phospholipids on platelets [42].

Procoagulants initiate the clotting cascade in response to a tissue injury, while circulating anticoagulants naturally aid in dissolving the formed thrombi. Several naturally occurring anticoagulants target different tissue factors to inhibit the coagulation process. For instance, tissue factor plasminogen inhibitor (TFPI) inhibits the activation of factor X and also subsequently inhibits the activation of factor VII via feedback inhibition while antithrombin majorly inhibits thrombin and factor Xa [31]. Antithrombin activity is enhanced in the presence of heparin cofactor II. Alternatively, thrombin interacts with thrombomodulin on endothelial surface which switches its activity from cleaving prothrombotic substrates to cleaving protein C [41]. Anticoagulants such as protein C and protein S are vitamin K-dependent serine proteases

wherein protein S acts as a cofactor to protein C to inactivate labile factors V and VIII [32]. In addition, endothelial cells release prostacyclin (vasodilator) and nitric oxide to decrease P-selectin secretion and reduce platelet aggregation [40]. Under normal conditions, a perfect balance is maintained between procoagulants and anticoagulants where blood thrombi are formed in response to a tissue injury to prevent us from bleeding out, but are also naturally dissolved to prevent vessel obstruction [31]. Thus, some of the tissue factors involved in activating the coagulation cascade are simultaneously involved in activating the fibrinolytic pathway. For instance, factor XIIa converts prekallikrein into kallikrein enabling kallikrein to convert kininogen into kinin (*eg.* Bradykinin) and mediate vasodilation. Kallikrein and plasminogen activator secreted by leukocytes and endothelial cells, cleave plasminogen into plasmin [39] enabling fibrin degradation and exposure of D-dimer antigens [43]. On the contrary, antithrombin can also inactivate kallikrein and plasmin to initiate coagulation [44]. Plasmin can also be inactivated by a serine protease inhibitor – α_2-antiplasmin.

Table 1-1: Summary of tissue factors and enzymes of the coagulation cascade. List of all tissue factors (represented in roman numerals), and enzyme catalysts (indicated in red) involved in activating the intrinsic, extrinsic, and common pathways in the coagulation cascade.

Intrinsic Pathway Factors		**Extrinsic Pathway Factors**	
Inactive form	**Active form**	**Inactive form**	**Active form**
XII (Hageman Factor) → XIIa Serine protease		VII (Stable factor proconvertin) → VIIa Tissue factor/trauma	
XI (Plasma antecedent) → XIa XIIa		VIII (anti-hemophilic factor) → VIIIa Thrombin	
IX (Christmas factor) → IXa IXa, Ca^{2+}			
Common Pathway Factors			
Inactive Form		**Active Form**	
X (Stuart-Prower factor) → Xa IXa, VIIa and/or VIIIa (tenase complex), Ca^{2+}			
II (Prothrombin) → IIa (Thrombin) Xa and/or Va (prothrombinase complex), Ca^{2+}			
I (Fibrinogen) → Ia (Fibrin) Thrombin (IIa), Ca^{2+}			
XIII (Fibrin stabilizing factor) → XIIIa Thrombin (IIa), Ca^{2+}			
- Thrombin also activates thrombomodulin and with protein S catalyst, protein C is activated. Furthermore, thrombin can activate factors V and VIII in a positive feedback manner while protein C can inhibit VI and VIII - Antithrombin (vitamin K independent glycoprotein) can inhibit thrombin, Xa, IXa, XIa, kallikrein and plasmin [44]			

Table adapted from [39]

1.4 Current acute medical and surgical interventions for ischemic stroke

1.4.1 Tissue plasminogen activator

Under normal physiological conditions, hemostatic disruptions caused by vascular injuries can be naturally fixed by physiological anticoagulants (mentioned in the previous section). However,

under pathological conditions such as thrombosis, hemostatic disruptions require additional acute management and appropriate treatment. There are several drug treatments available that target different aspects of the coagulation cascade. Drugs including Aspirin, Plavix (Clopidogrel), Dipyridamole, Tirofiban, Abciximab (Reopro), and Eptifibatide use different modes of mechanisms to inhibit platelet aggregation [45], [46]. For instance, aspirin works by irreversibly inhibiting cyclooxygenase-dependent conversion of arachidonic acid into thromboxane and it also inhibits prostaglandins, consequently reducing the effects of edema during thrombosis. Clopidogrel works by blocking the ADP receptors on platelets while Dipryidamole works by inhibiting the uptake of adenosine which causes adenosine accumulation, and results in inhibition of platelet aggregation. Tirofiban, Abciximab and Eptifibatide competitively bind to glycoprotein IIb/IIIa receptors to prevent the binding of fibrinogen and vWF [45]. On the other hand, drugs such as Rivaroxaban (Xarelto), Apixaban, Dabigatran (Pradaxa), and heparin target thrombin inactivation [45], [46]. Rivaroxaban (Xarelto) and Apixaban are selective direct inhibitors of factor X of the coagulation cascade while Dabigatran (Pradaxa) is an hirudin analog that directly binds to thrombin and prevents the conversion of fibrinogen into fibrin [46]. Heparin on the other hand is an indirect thrombin inhibitor as it binds to antithrombin enzyme, activates it to then inhibit thrombin. Warfarin is another anticoagulant but acts as a vitamin K antagonist to inhibit γ-carboxylation of vitamin K-dependent synthesis of several tissue factors including factor II, VII, IX, and X [31].

Until recently, one of the most prominent drug treatments for AIS was, the administration of intravenous thrombolytic drug, recombinant tissue-plasminogen activator (rtPA). Tissue-plasminogen activator works by cleaving arginine-valine bonds in plasminogen and converting it into plasmin [45]. The Food and Drug Administration (FDA) approval of tPA in 1996 [47] as a

first line approach to treating AIS patients, revolutionized stroke care [48]. Similarly, another mainstay treatment for AIS included streptokinase, alteplase, reteplase or urokinase administration. However, due to several drawbacks associated with rtPA such as its short treatment window of 4.5 hrs (tPA efficacy between 3-4.5hrs was proved in the European Cooperative Acute Stroke Study – ECASS III clinical trial) [49], [50] and contra-indications list including ICH, hyper/hypoglycemia, hypertension, thrombocytopenia and history of anticoagulant use [51], only 3-8.9% patients receive this drug in North America [47], [52]. In fact, in Canada the administration of thrombolytics between 1999 and 2000 was reportedly only 1.4% [53]. In addition, the recanalization success for large vessel occlusions is very low [54]. Another type of tissue plasminogen activator, Tenecteplase (TNK) which is a FDA approved drug for myocardial infarction, is now being expanded into treating AIS. TNK is more resistant to plasminogen activator inhibitor and has shown better outcomes for 3-month functionality and reduced intracranial bleeding than tPA [55]. Despite the development of various thrombolytic drugs, the recanalization rates obtained by IV thrombolysis are slim and also pose higher risks for ICH compared to mechanical strategies [56].

1.4.2 Endovascular Therapy

Endovascular therapy was primarily developed to expand the treatment window, improve recanalization rates and prevent intracranial hemorrhage [57]. Endovascular therapy (EVT), in the form of mechanical thrombectomy is a highly effective technique, whereby the thrombus is mechanically retrieved often via the femoral artery [58]. However, for those patients that present with aorta-iliac femoral disease, a radial or brachial approach might be more appropriate than going through the femoral artery. In addition, due to safety concerns, direct carotid puncture is a less popular approach while performing EVT [59]. In recent years, with technological advances,

EVT has demonstrated an improvement in the health outcomes of AIS patients and has also shown superiority over other treatment options for stroke patients with large vessel occlusions [60], [61], [62].

In 1980s, microcatheters were used for intra-arterial delivery of thrombolytics at the occlusion site. In the subsequent years, Prolyse in Acute Cerebral Thromboembolism (PROACT) trials tested the efficacy of a new thrombolytic drug, prourokinase < 6 hrs after symptom onset in patients with M1 and M2 occlusions. PROACT II was not approved by the FDA as the significance for good clinical outcomes measured by Modified Rankin Scale mRS < 2 for the treatment and placebo groups was ($p = 0.04$) with a higher occurrence of ICH observed in the treatment group [63]. Following that, trials testing intravenous administration of Eptifibatide and Abciximab showed no significant differences between the treatment and placebo groups [64]. While the PROACT II trial was negative, it did stimulate the development of alternative techniques that focused on disrupting the thrombus rather than dissolving it. The first EVT clinical trial conducted in 2003 called Thrombectomy in Middle Cerebral Artery Embolism (TIME) yielded negative results [57]. Other clinical trials including Interventional Management of Stroke (IMS I, II and III) combined the use of IV-tPA and IA-tPA with EKOS ultrasound disruption of thrombi but did not achieve promising results either [65]. In 2004, Concentric Medical Inc. developed a first generation thrombectomy device called Mechanical Embolus Removal in Cerebral Ischemia (MERCI) retriever [57] which was approved by the FDA based on the 510K pathway. The MERCI retriever was tested in the MERCI and Multi-MERCI non-randomized, multi-centre clinical trial where patients with NIHSS ≥ 8 were recruited and treated 8 hrs after onset. However, because the recanalization rates were close to the mortality rates, the efficacy of the MERCI retriever was questionable. Recanalization rates of 46% were obtained

with MERCI alone while recanalization rates of 60.8% were achieved when MERCI was combined with IA-tPA [66]. In 2008, Penumbra developed the Penumbra Aspiration System to aspirate the thrombus via a vacuum pump. The Penumbra system showed better 90-day clinical outcomes than MERCI but the mortality rates were still high [64].

The off-label use and success of detachable stent-retrievers, such as Solitaire (Medtronic Inc., Irvine, California, USA) and Trevo (Stryker Inc., Michigan, USA) marked the development of 2nd generation thrombectomy devices. These devices tested in clinical trials such as Solitaire with the Intention for Thrombectomy (SWIFT) and Thrombectomy Revascularization of large vessel occlusion in acute ischemic stroke (TREVO) trials showed statistically significant improvements in recanalization, mRS scores ≤ 2, mortality rates, and ICH rates compared to the MERCI retriever [67]. However, clinical trials testing the efficacy of EVT over IV-tPA, Mechanical Retrieval and Recanalization of Stroke Thrombus using Embolectomy (MR RESCUE), IMS III, and Local versus Systemic Thrombolysis for Acute Ischemic Stroke (SYNTHESIS), failed to show EVT superiority over IV-tPA [68], [69]. MR RESCUE reported good functional outcomes of 12.5% *versus* 18.5%, $p = 0.368$ whereas IMS III reported 42.65% *versus* 40.18%, $p = 0.553$ and SYNTHESIS reported 41.99% *versus* 46.4%, $p = 0.397$ [70]. Limitations of each of the studies were identified including, lack of patient screening, recruitment of patients despite the absence of large vessel occlusion, use of 1st generation devices, and delayed door-to-needle time. Despite the drawbacks, these trials led to the use of CTA as a standardized means for screening EVT-eligible patients [59]. In 2014, introduction of large bore and flexible aspiration catheter enabled the development of a direct aspiration first pass technique (ADAPT) which gained popularity for its simplicity, cost-effectiveness, shorter procedural times and rapid recanalization times [71], [72]. In 2015, 5 clinical trials showed promising results in the development of EVT.

Multicentre Randomized Control Trial for Endovascular Treatment for Acute Ischemic Stroke in Netherlands (MR CLEAN) was the first randomized control trial (RCT) to publish positive results. In this study, 89% of the patients received IV-tPA prior to EVT, patients were treated 6 hrs after onset, patients eligible had an NIHSS > 2 and the clinical outcomes were measured using an odds ratio [73]. Endovascular treatment for Small Core and Anterior circulation Proximal occlusion with Emphasis on minimizing CT to recanalization times (ESCAPE) was the second RCT and in this study 76% of the patients received IV-tPA prior to EVT, patients were treated 12 hrs after onset, and had an NIHSS > 6 and ASPECTS > 5. ESCAPE was the only study to show statistically significant reduction in mortality rates (10.4% *versus* 19.0%, $p = 0.04$), and earliest median reperfusion time [62, 74]. Extending the time for Thrombolysis in Emergency Neurological Deficits with Intra-Arterial therapy (EXTEND-IA) was the third RCT where patients were treated 6 hrs after onset. The inclusion and exclusion criteria were highly stringent; however, this study showed excellent reperfusion success and functional independence in 71% of the patients [75]. SWIFT-PRIME was the fourth clinical trial and in this study 88% of the patients received IV-tPA prior to EVT, patients were treated 6 hrs after onset and even though this study showed functional independence in only 60% of the patients, it reported the highest success rate for reperfusion [76]. Lastly, in the clinical trial Endovascular Revascularization With Solitaire Device Versus Best Medical Therapy in Anterior Circulation Stroke Within 8 Hours (REVASCAT), patients who were ineligible for receiving IV-tPA with an NIHSS and ASPECTS > 6 were recruited and treated 8 hrs after onset [60]. All of these 5 clinical trials proved the efficacy of EVT to be superior to IV-tPA for establishing higher functional independence (mRS 0-2): MR CLEAN (43.7% *versus* 28.2%, $p = 0.001$), ESCAPE (53.05% *versus* 29.3%, $p = 0.001$), EXTENDIA (71% *versus* 40%, $p = 0.009$), SWIFT-PRIME

(60.2% *versus* 35.5%, *p = 0.001*) and REVASCAT (43.7% *versus* 28.2%, *p = 0.021*) [70]. In addition, these 5 clinical trials also contributed to: mandating clinical imaging for screening EVT–eligible patients, showed improved clinical outcomes with an increased treatment window, showed increase in functional independence and decrease in ICH despite the combined use of thrombolytics, and showed significant reduction in mortality rates [66]. The most recent clinical trial, Diffusion Weighted Imaging or Computerized Tomography Perfusion Assessment With Clinical Mismatch in the Triage of Wake Up and Late Presenting Strokes Undergoing Neurointervention With Trevo (DAWN) tested the efficacy of EVT at 24 hrs [77].

Even though the long-term clinical outcomes are improved via EVT compared to IV-tPA [78], it is still not clear as to which deployment technique and device combination is the most effective for quick thrombus retrieval. In an ideal scenario the thrombus can be retrieved quickly and efficiently; however, interventionists occasionally have to perform multiple passes to extract the thrombus using multiple approaches and sometimes are still unable to completely restore intracranial flow. There are different classes of mechanical thrombectomy devices that work to achieve recanalization (blood restoration) via different biomechanical mechanisms [79]. The table below summarizes the different devices used during thrombectomy (table 1-2)

Table 1-2: List of devices used in mechanical thrombectomy. Provides a summary and information of the most commonly used devices during endovascular therapy at Royal University Hospital, Saskatchewan

Category	Device Name	Measurements	Purpose	Company [Ref]
Guide catheters	Neuron Max 088	Sheath length – 6F Lumen – .088inch	Provides support through the aortic arch until the cervical region (ICA) and delivers primary device through the lumen.	Penumbra [https://www.penumbrainc.com/wp-content/uploads/2016/12/4900C_NeuronMAX_Flex_Comparison_Ordersheet_USA.pdf]
	Neuron Max 070	Sheath length – 6F Lumen – .070 inch		
	Neuron Max 053	Sheath length – 6F Lumen – .053 inch		
Micro-catheters	Velocity	Length – 160cm ID – .025inch OD – 2.95F proximal 2.60F distal	Used for facilitating coaxial delivery of the penumbra reperfusion catheters.	Penumbra [https://www.penumbrainc.com/neuro-device/velocity-system/]
Microwires	Synchro 2 standard	Total length – varies (200 or 300cm) Distal segment – 35cm OD for guidewire – .036mm (proximal/distal)	Microwires are intended to provide maximum flexibility, atraumatic entry into delicate vasculature, radiopacity, shapeability, torque transmission, and lubrication through its hydrophilic coating.	1. Stryker Neurovascular [https://www.strykerneurovascular.com/us/products/access/synchro-guidewires] 2. Boston Scientific [https://www.bostonscientific.com/content/dam/bostonscientific/pi/portfolio-group/PI-92202-AD_Fathom_Brochure.pdf]
	Fathom	Total length – varies (140, 180, 200, 215 cm Nitinol tip length – 25cm Distal floppy tip – 10cm or 20cm Proximal/Distal OD – .016 inches Tip shape – Straight or angled		
Reperfusion catheter	ACE 068	Length – 132cm Inner lumen – .068 inch	ACE reperfusion catheters are designed to provide optimal trackability through tortuous	Penumbra [https://www.penumbrainc.com/wp-content/uploads/2016/12/10667A_ACE68_Science-of-Aspiration_Brochure_USA.pdf]
	ACE 064	Length – 132cm Inner lumen – .064 inch nitinol distal lumen/.068 inch proximal		

	ACE 060	Length – 132cm Inner lumen – .060 inch nitinol distal lumen/.068 inch proximal	vessels. Ace catheter attach to the aspiration tubing and provides greater aspiration power.	
	5MAX	Length – 132cm OD – 6F proximal 1.67mm distal ID – .064inch proximal .054inch distal	Max reperfusion catheters, similar to the ACE reperfusion catheters are intended to attach to aspiration tubing and an automated vacuum to aspirate the thrombus efficiently.	Penumbra [https://www.penumbrainc.com/wp-content/uploads/2016/12/10667A_ACE68_Science-of-Aspiration_Brochure_USA.pdf]
	3MAX	Length – 153cm OD – 4.7F proximal 1.27mm distal ID – .043inch proximal .035inch distal		
Stent-retrievers	Solitaire Platinum device	Length (scaffolding + pushwire) – 130cm Diameter – 6mm Nitinol retrieval – 40mm	Overlapping stent-retriever are comprised of a nitinol scaffolding retrieval zone attached onto a metal pushwire to provide rigidity when delivered through a microcatheter.	Medtronic [https://www.medtronic.com/us-en/healthcare-professionals/products/neurological/revascularization-stroke/solitaire.html]
	Trevo XP	Diameter – 4mm Retrieval length – 20mm	Provides full length of radiopacity for efficient and easy placement using 360° large cells, and soft distal tip.	Stryker [https://www.strykerneurovascular.com/products/ais/trevo-xp-provue-retriever]

	3D Separator	Total Length – 26mm Diameter – 45mm	Has four intraluminal chambers with petals designed to extract the thrombus faster with minimal vessel wall contact.	Penumbra [https://tinyurl.com/y494fx9w]
Angiograph catheter	5F VER (vertebral) Catheter	Length – 100cm Diameter – .038inch	Angiographic catheter used for diagnostic purposes.	Cordis [https://tinyurl.com/y63pd6yj]

Abbreviations: F = French, ICA = internal carotid artery, ID = internal diameter, OD = outer diameter

During thrombectomy, fluoroscopy is used for guiding instruments through the patient's arteries to retrieve the thrombus. Other clinical imaging modalities such as standard computed tomography (CT) scan, computed tomography angiogram (CTA), and magnetic resonance imaging (MRI) are utilized to triage patients. Shown below is an image of a cerebral angiogram showing right MCA occlusion **(Fig. 1-2)**.

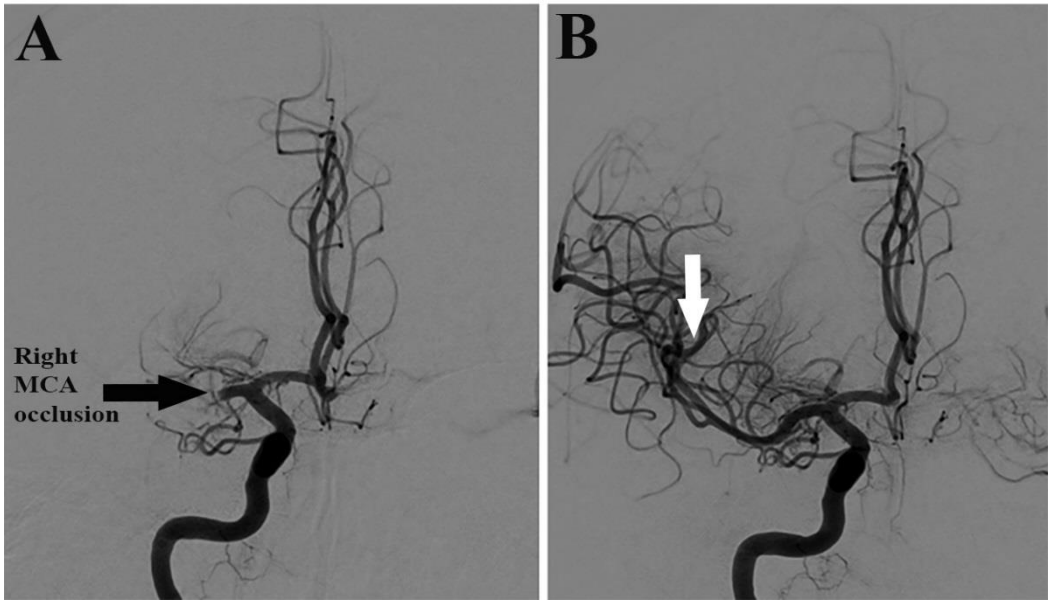

Figure 1-2: Cerebral Angiography of Arterial Occlusion. Cerebral angiography performed using Isovue300 contrast agent to capture images before (A) and after (B) mechanical thrombectomy. Complete restoration of blood flow through the right MCA is indicated by the white arrow.

1.5 Importance of studying thrombus composition

Infarction maturation after ischemia depends on four factors: 1) time from onset until complete infarct maturation, 2) volume of tissue affected, 3) brain structures affected (neurons, interneurons, myelinated fibres), and 4) interindividual differences including recanalization rate, thrombus size, thrombus length, location of vessel blockage, systemic blood pressure, blood volume, collateral flow status, temperature, serum glucose, and thrombus characteristics [80]. The phrase "time is brain" is popularly emphasized while treating a patient with cerebral

ischemia because the brain cells begin to die even before the thrombus is removed or blood flow is restored. The forebrain contains 22 billion neurons and 157 trillion synapses. With normal aging, 31 million neurons are lost each year while with stroke, 1.9 million neurons are lost every minute [80]. Since the thrombus is the primary target of most acute treatments: chemical and mechanical [81], understanding the composition and identifying targets within the thrombi could greatly facilitate the development of new and effective treatment strategies to retrieve them in a time-efficient manner, and minimize post-stroke damage. Even though the Solitaire system has shown efficient, safer and favourable outcomes including; increase in recanalization success and 90-day functionality, and decrease in procedural time, mortality rates and symptomatic ICH rates than MERCI, [82] mechanical thrombectomy performed by Solitaire and/or aspiration techniques still fails to achieve complete recanalization in 15-30% of proximal occlusion strokes [83]. Moreover, the number of passes made during thrombectomy is directly proportional to intra-arterial damage that occurs. Additionally, the longer the devices are lodged in the vessels during retrieval, the more the chances of further coagulation (distal embolization) and vascular trauma (vessel perforation, rupture) are increased [56].

Clinical imaging modalities (CT, CTA and MRI) serve to identify various aspects of ischemia including; collateral flow status, occlusion location, early vessel signs and thrombus signs, infarct size, and brain regions affected however, these techniques do not reveal any information on the texture, gross pathological appearance, or cellular components characterizing thrombi. Since thrombi are the proximate cause of ischemic stroke and the immediate target for current treatments, identifying targets within the thrombus can provide us with greater insights to further improve interventional and long-term clinical outcomes.

The earliest studies to conduct histological evaluation, analyzed thrombo-emboli from post-mortem samples [84]. Marder *et al.* was the first group to perform systemic analysis on thrombo-emboli freshly retrieved from the cerebral vasculature [85]. Along with Marder *et al.*, several other studies acknowledged the presence of fibrin, platelets, erythrocytes, endothelial cells, neutrophils and monocytes to be present in all thrombi [85], [86] [87]. Despite the presence of common components, the quantitative proportions and distribution patterns of these histological components differed from one thrombus to the next. Histological characterization was important for three reasons:

1) to identify the age of the thrombus based on the presence of histological biomarkers and distinctive distribution patterns [88]. A study showed that endothelial cells and organized fibrin were biomarkers for > 3 day old thrombi whereby, older thrombi had decreased thrombolytic responsiveness [89];

2) to determine if the source of origin could predict thrombus histology based on erythrocyte, fibrin and platelet ratios. It has been previously reported that thrombi originating from a cardiac source were rich in erythrocytes due to their development under low shear stress and low blood flow while thrombi originating from an arterial source were rich in platelets and fibrin due to their development under high shear stress and high blood flow [85]; and

3) to understand whether individual thrombus structures play a role in treatment failures. For instance, many studies have reported fibrin as the primary cause for reduced thrombolytic susceptibility to streptokinase [89] as well as rtPA [90], [91]. Similarly, *in vitro* studies have reported an association between thrombus composition and choice of an ideal thrombectomy device used during retrieval, indicating the role of composition and texture in device-thrombus interaction [92], [93]. In fact, studies have shown that organized fibrin-rich thrombi contribute to

hard/rigid texture that make mechanical retrieval difficult [92], [94] and therefore, these thrombi require increased maneuvers and retrieval attempts [95]. Nevertheless, treatment failures might depend on other factors besides composition including length of the thrombus. Riedel *et al.* reported that IV-tPA responsiveness was very low for thrombi > 8 mm in size [58].

This study aims to use conventional histochemical techniques to identify tissue morphology in freshly retrieved thrombi, and provide new insight into thrombus composition by characterizing the distribution of elements and organic molecules using synchrotron-based X-ray fluorescence imaging (XFI) and Fourier-transform infrared spectroscopy (FTIR) techniques, respectively to identify new compositional markers and correlate these findings with clinical and interventional parameters that could potentially aid in improving EVT outcomes.

1.6 Experimental imaging modalities for characterizing thrombi

Prior to applying any experimental imaging techniques including histology, immunohistochemistry, XFI or FTIR that characterize components in the tissues, it is critical to prepare samples correctly. Fresh tissue samples are delicate and damage easily. Thus, to maintain cell morphology and tissue architecture it is essential to preserve, fix, and section the samples properly. Principles of preservation, fixation and imaging modalities used in this study are thus critical, and are elaborately explained in the sections below.

1.6.1 Tissue preservation and fixation

Tissues can be preserved through cryopreservation using liquid nitrogen or isopentane, or through chemical fixation using aldehyde, acetone, or alcohol-based fixatives [96].

Cryopreservation is the maintenance of biological tissues at cryogenic temperatures. At temperatures between 0°C and -25°C, enzymatic activities within the cells are slowed down. At temperatures below -40°C, all physiochemical reactions cease and at temperatures below -196°C,

tissues preserve for longer periods of time [97]. Freshly retrieved tissues contain water within their cells. Pure frozen water exists in three forms; hexagonal crystalline, cubic crystalline, and vitreous form [98]. Cryopreservation can be accomplished either by slow freezing or by vitrification/rapid freezing. In slow freezing, samples are preserved uniformly from the outside to the inside at 1°C/min [99]. However, this technique forms hexagonal and cubic crystals most distally from the freezing surface which expand upon solidification. Thus, slow frozen sections undergo "Swiss cheese effect", a freezing artifact that results in multiple holes in the sections. On the other hand, in vitrification, intracellular water does not have time to form ice-crystals as the tissues are directly transformed from an aqueous phase to solid glass-state keeping the water in a vitreous form and preventing expansion upon solidification [99]. Rapid or flash freezing is commonly done using liquid nitrogen or isopentane (2-methylbutane). Usually, samples that are rapidly frozen, are placed in an optimal cutting temperature (OCT) embedding matrix, composed of 10.24% polyvinyl alcohol, 4.26% polyethylene glycol and 85.5% non-reactive ingredients which prevent the samples from cracking while being flash frozen [100]. Because liquid nitrogen is the coldest liquid (-196°C) and has a low specific heat constant, when it comes in contact with OCT it forms a vapour barrier causing the inner core of the tissue sample to freeze slowly and unevenly. Similarly, when isopentane is chilled with dry ice it only attains a temperature of -78.5°C which also results in slow freezing of the inner core and increases the risk of ice-crystal formation. Thus, to get around this issue, the most effective way to cryopreserve a sample, as done in this study (for utilizing XFI and FTIR techniques), is by flash freezing the sample in isopentane that is chilled using liquid nitrogen instead of dry ice. Even though cryopreservation is a relatively quicker process and a highly effective technique for preserving labile biomolecules

than chemical fixation, tissues still get damaged in this process as temperatures fall from 37°C or room temperature to -196°C [97].

With chemical fixation, cell morphology is better maintained than in cryopreservation as chemical fixation minimizes cellular and structural damage. There are different classes of fixatives that can be used during chemical fixation including: 1) cross-linking fixatives such as aldehydes, 2) precipitating fixatives such as alcohols and acetone which are also sometimes used for fixing cryosections, 3) oxidizing fixatives such as osmium tetroxide, 4) mercurials such as B-5 and Zenker's fixative, and 5) picrates such as picric acid and Bouin's fluid [101]. Aldehydes are the most widely used fixatives [102]. They create covalent bonds crosslinking proteins, mostly lysine residues within the tissue. Proteins also get anchored to the cytoskeleton which adds rigidity to the tissue. Specimens are commonly fixed in formaldehyde for histology, or glutaraldehyde for electron microscopy. In this study (for utilizing histological techniques), specimens were fixed in formaldehyde (30.031g/mol MW). Formaldehyde (H-CHO) naturally exists in gaseous state. However, in aqueous solutions formaldehyde is combined with water to form methylene hydrate ($HO\text{-}CH_2\text{-}OH$). A study by Sompuram *et al.* showed that, at a molecular level formaldehyde reacts with an amine group on an arginine residue within the tissue protein which forms an intermediate iminium ion which then reacts with tyrosine residues via a covalent bond, thereby implicating a Mannich reaction [103]. Usually for histological studies, the formalin used contains 37-40% of formaldehyde combined with 60-63% of water. Furthermore, paraformaldehyde, an insoluble powdered polymer of methylene hydrate molecules can be easily hydrolyzed into formaldehyde in the presence of heat (60°C) and OH^- ions [102].

After the fixation step is complete, cryopreserved specimens are sectioned in a -20°C cryostat while formalin-fixed samples are infiltrated with a liquid agent such as resin or paraffin that

solidifies [96], and then sectioned in a microtome. Steps involved in processing tissues for histological staining, immunohistochemistry, X-ray fluorescence imaging, and Fourier transform infrared spectroscopy are described below.

1.7 Principles of histological stains and immunohistochemistry

Staining techniques were developed in the seventeenth century by pioneers such as Van Leeuwenhoek who used natural substances such as plants, insects, and saffron to dye plant and animal tissues [104]. As later techniques developed, different histological stains were devised to study various types of cellular components.

A thrombus is a clump of coagulated materials that circulate in the blood. The two major blood components include plasma and formed elements [1]. The plasma consists of proteins including albumin (66.5 kDa MW), globulins (93-1193 kDa MW), fibrinogen (~340 kDa MW), enzymes, electrolytes, nutrients, blood gases (O_2, N_2, and CO_2), and hormones. The formed elements are composed of erythrocytes (red blood cells), thrombocytes (platelets) and leukocytes (white blood cells). A hematopoietic stem cell gives rise to myeloid progenitor and lymphoid progenitor cells. The myeloid cell differentiates into thrombocytes, erythrocytes, and myeloblasts. The myeloblasts further give rise to neutrophils, eosinophils, basophils or monocytes. The lymphoid stem cell gives rise to natural killer cells (large lymphocytes) and small lymphocytes which further differentiate into a T-cell lymphocyte or a B-cell lymphocyte. Neutrophils, eosinophils, and basophils contain secretory granules in their cytoplasm and therefore are called granulocytes, while monocytes and lymphocytes are called agranulocytes. Granulocytes and agranulocytes together are classified as white blood cells [1].

As mentioned earlier, previous histological evaluations have characterized the presence of several biological components in thrombi including platelets, monocytes, erythrocytes,

leukocytes and fibrin [85], [86]. Based on their biological components, thrombi have been classified as either red thrombi (*i.e.* rich in erythrocytes and possibly from a cardiac source) or white thrombi (*i.e.* rich in fibrin and possibly from an arterial source) [85], [87]. In this study, two histological stains: Hematoxylin and Eosin, and Masson's trichrome were used for identifying the distribution of fibrin, erythrocytes, and leukocytes. On the other hand, to stain for platelets, monocytes and endothelial cells, immunohistochemistry techniques were used.

1.7.1 Hematoxylin and Eosin Stain

Hematoxylin and Eosin (H&E) is a combination of two stains: Hematoxylin and Eosin. This combination was introduced by Wissowzky in 1876 [105]. Hematoxylin is extracted from a logwood tree, *Hematoxylum Campechianum*, and was first used by Wilhelm von Waldeyer-Hartz in 1863 [106] as a nuclear stain. The active colour in hematoxylin is hematein. When the hematoxylin solution is prepared, sodium iodate is added to catalyze the oxidization of hematoxylin into hematein. Because hematein is anionic, it acts as a weak dye to bind the negatively charged DNA and therefore is combined with aluminum salts to form a cationic stain and bind to the phosphate backbone of DNA via electrostatic forces and covalent bonds [107]. Other additives in the solution include ethanol and glacial acetic acid which are used for dissolving the dye and increasing selectivity for nuclear staining, respectively.

There are two staining systems for Hematoxylin: progressive and regressive [108]. In the progressive method, such as Gill's or Mayer's, tissues are stained for a specific amount of time while in the regressive method, such as Harris's which is used in this study, tissues are overstained in the solution and then differentiated in acid alcohol to remove excess stain. Differentiation in the acidic solution also stains the nucleus red which is why tissues are blued using alkaline-based reagents such as aqueous lithium carbonate that stains the nucleus dark-

purple or blue [108]. Eosin is used as a counterstain to hematoxylin. Eosin is an acidic, anionic dye that binds to positively charged molecules such as proteins, connective tissues and red blood cells. The solution is made by dissolving the dye in ethanol and adding acetic acid to intensify the stain. Hematoxylin stains white blood cells dark-purple, while eosin stains the fibrin as well as red blood cells bright pink and eosinophil granules red.

H&E is the gold standard stain used to begin tissue examination in pathology, but does not contrast different types of tissues and cells resulting in insufficient cytoplasmic and extracellular structure differentiation [109]. Thus, to distinctively identify cellular structures and take into consideration other key factors of the coagulation cascade such as platelets, macrophages and endothelial cells, special stains such as Masson's trichrome [105] or immunohistochemical tools are utilized.

1.7.2 Masson's Trichrome Stain

Masson's trichrome (MT) protocols evolved from the formulations used by Claude L. Pierre Masson in 1929 [110]. Prior to staining with the three primary trichrome stains, tissues are fixed in mordant Bouin's solution and stained with Weigert's iron hematoxylin. Weigert's iron hematoxylin is used as a nuclear stain and contains ferric chloride, hydrochloric acid, hematoxylin, and ethanol to resist decolouration from the following acidic dyes. Ferric chloride acts as a mordant and oxidizer for hematoxylin [111]. MT is a combination of three stains: Beibrich scarlet-acid fuchsin which is an acidophilic dye and stains erythrocytes bright-red, phosphomolybdic/phosphotungstic acid which is used for differentiation and displacement of red dye from fibrin fibres, and aniline blue which is applied to stain the fibrin fibres blue [112]. Furthermore, acetic acid is used for differentiating and intensifying aniline blue.

1.7.3 Chromogenic Immunohistochemistry

Immunohistochemistry is a technique for selectively identifying antigens within cells and tissues using specific antibodies. Antibodies also known as immunoglobins, are Y-shaped monomeric glycoproteins that have specific affinity for biomolecules called antigens [113]. The antibody contains an antigen-binding site called paratope while the antigen contains an antibody binding site called epitope. Epitopes could be composed of a specific amino acid sequence (linear structure) or could be in the form of a tertiary structure [114]. When antibodies are developed to target antigens, the analytical validity depends on two factors; 1) sensitivity (the smallest amount of antigen detectable), and 2) specificity (the ability of the antibody to selectively recognize and bind to the desired antigen, and not others) [114]. Antibodies can be monoclonal or polyclonal. Both monoclonal and polyclonal antibodies are developed by injecting a protein into a host organism. This initiates an immune response where the host generates antibodies against the injected protein. Monoclonal antibodies are derived from single B-lymphocyte cell lineages to react with a single epitope while polyclonal antibodies are produced by repetitive stimulation and multiple B-lymphocyte cell lineages (B plasma cells, B memory cells) to react with multiple epitopes on the antigen. Antibodies are then purified from blood serum extractions [113], [115]. While monoclonal antibodies provide great specificity and reproducibility, they are less sensitive. On the other hand, polyclonal antibodies provide higher sensitivity and are more resistance to pH changes but are less reproducible and tend to increase background noise.

Immunohistochemistry assays consists of five key steps: tissue fixation and processing (as previously mentioned), antigen epitope retrieval, blocking, immunolabelling and detection, and counterstaining.

Antigen retrieval – For formalin fixed paraffin embedded tissues, antigen retrieval is a necessary step to open up the cross-linked methylene bridges formed by formaldehyde fixation that mask epitopes via Mannich reactions [103]. Protein cross-links can be broken by heat or enzymatic treatment. Heat induced epitope retrieval (HIER) is implemented using either of these methods: 1) water-bath method where sections are incubated in a 97°C water bath containing the retrieval working solution, 2) microwave method where sections are placed in a microwaveable vessel containing the retrieval working solution, and 3) high pressure method where sections are placed in a pressure cooker containing the retrieval working solution. There are different types of retrieval working solutions, including citrate buffer solution, Phosphate Buffered Saline (PBS) solution, Ethylenediaminetetraacetic acid (EDTA) solution, Tris-EDTA, and Tris-HCl solution. On the other hand, proteolytic induced epitope retrieval (PIER) is implemented by incubating sections in proteolytic enzymes such as trypsin, proteinase K, pepsin etc. [116], [117].

Blocking – This step blocks endogenous enzymes, prevents non-specific antibody binding and reduces background signal. Blocking can be achieved using protein blocking reagents such as serum (goat, donkey, chicken) and bovine serum albumin, or avidin-biotin reagents or peroxidase blocking reagents [115].

Immunolabelling and Detection – There are two detection methods: direct and indirect. The direct method is a one-step process where the primary antibody reacting with the antigen is labelled with an enzyme substrate such as horseradish peroxidase (HRP) or alkaline phosphatase [118]. This is a simple and specific method but attains a lower signal amplification and lower sensitivity. On the other hand, the indirect method is a two-step process where the primary antibody reacting with the antigen is labelled with a secondary antibody [119]. For instance, if the primary antibody is mouse anti-human (*i.e*. the antibody is raised in a mouse against a human

antigen), the secondary antibody could be goat anti-mouse (*i.e.* the antibody is raised in a goat against a mouse antigen so as to identify the mouse primary antibody). The secondary antibody is then conjugated with a HRP enzyme substrate. Sometimes secondary antibodies are biotinylated, in other words, conjugated with biotin molecules that recruit avidin proteins to amplify the signal further [118], [120]. In both methods, the antigen-antibody-HRP complex is then tagged with a chromogenic substrate such as 3, 3'-diaminobenzidine (DAB) which is oxidized by hydrogen peroxide to yield an insoluble brown pigment that precipitates at the antigen site, a technique developed by Nakano and Pierce in 1960s and described by Sternberger and colleagues in 1970 [121], [122]. DAB is effective as a single label or as a second color for multiple antigen labeling. Sections stained with DAB can be viewed using a light microscope and can be stored for a long time. On the contrary, in fluorescence microscopy, antigen-antibody-HRP complex are tagged using different fluorophores instead of DAB molecules that absorb and emit at different wavelengths when viewed under a fluorescence microscope.

1.8 Principles of XFI

1.8.1 XFI beamline components

The electromagnetic spectrum consists of gamma rays, X-rays, ultraviolet, visible, infrared (near, mid and far infrared), microwaves and radio waves. Gamma rays and X-rays have shorter wavelengths, higher energy and higher frequencies. They are both types of ionizing radiation due to their abilities to ionize atoms. On the other hand, microwaves and radio waves have longer wavelengths, lowest energy and lowest frequencies [123]. A wavelength is defined as the distance between adjacent crests and troughs of a light wave while frequency measures the number of waves that pass a given point per second. Table 1-3 represents the electromagnetic spectrum with specific wavelength and frequency range.

Table 1-3: Electromagnetic wave spectrum with specific wavelength and frequency range.

Range	Wavelength (m)	Frequency range (Hz)
Gamma rays	10^{-12}	$>10^{19}$
X-ray	10^{-9} - 10^{-11}	10^{17}- 10^{19}
Ultraviolet	1×10^{-7}-10^{-9}	10^{14}-10^{17}
Visible light	7×10^{-7}- 4×10^{-7}	$4.3\times10^{14} – 7.5\times10^{14}$
Near Infrared	$7.5\times10^{-7} – 2.5\times10^{-6}$	$1\times10^{14} – 4\times10^{14}$
Mid-infrared	$3\times10^{-6} – 8\times10^{-6}$	$3\times10^{13} – 1\times10^{14}$
Far-infrared	$1.5\times10^{-5} – 0.001$	$3\times10^{11} – 2\times10^{13}$
Microwave	0.01-1×10^{-5}	10^{9}-10^{12}
Radio wave	>0.01	$<10^{9}$ Hz

Synchrotron radiation is generated at experimental facilities such as the Canadian Lightsource (CLS), Stanford Synchrotron Radiation Lightsource (SSRL) and National Synchrotron Lightsource (NSLS). Synchrotron radiation is generated as a result of ultra-relativistic particles (usually electrons) accelerating through a magnetic field. At the CLS, electrons are generated by an electron gun (hot filament) and are drawn by an electromagnetic field into a linear accelerator (LINAC) where they are accelerated to 250 MeV using Radio Frequency (RF) Cavities and are then transferred to the booster ring in bunches where the electron bunches are then imparted with additional energy from microwave fields generated in the RF cavity to reach a total energy of 2.9 GeV. Electrons are then injected into the storage ring where they orbit [124]. Electrons prefer to travel in a straight line; however, their path is bent by bend magnets or insertion devices – (undulators or wigglers) in the storage ring which causes the electrons to radiate photons in the form of synchrotron radiation. When emitting light, the energy lost by the electrons are replaced by the RF cavities. As the electrons turn, they produce a bright collimated light that goes straight into the "front end" of the beamline [124]. Typical XFI beamline components may include: 1) monochromator, a device that separates different wavelengths of light using either optical

dispersion (as prism) or grating (as diffraction) so that a single energy range can be selected and the wavelengths that are not required can be filtered out, 2) slits and micro-focus optics that define the horizontal and vertical dimensions of the beam, 3) an upstream detector (ion chamber – I_0) that is filled with a gas mixture to absorb 20-40% of the incident beam (measures initial photon flux), 4) a downstream detector (ion chamber – I_1) that detects the beam transmitted through the sample (attenuated photons) and thereby absorbs 20-40% of the transmitted beam, 5) a X-ray fluorescence detector that detects fluorescence signal from the sample, 6) a precision stage to mount samples on, 7) windows to allow monochromatic beam to pass, and 8) shutters that turn off the beam to downstream enclosures. Photoelectric effects, coherent scattering, Compton scattering, pair production, and photodisintegration are few of the factors that contribute to X-ray attenuation as X-rays interact with matter [125]. Figure 1-3 illustrates a schematic representation of the X-ray fluorescence imaging beamline at SSRL.

When the incident X-ray energy is above the absorption edge of an element, it can excite and eject a core electron as a photoelectron (photoelectric effect) and create a core hole [125]. To stabilize the atom, the core-hole is filled by a neighbouring electron that transitions from an outer shell into the core space, emitting an X-ray fluorescence photon. The emitted fluorescence photon is detected by the X-ray fluorescence detector placed in the beamline [124]. Most atoms comprise of various electron shells (K, L, M, N…). X-ray fluorescence emissions are characterized using these shells. Additionally, alpha, beta and gamma designations are also used for denoting specific electron transitions from higher orbitals. For instance, a transition from L→K shell is referred to as K_α or M→K shell is referred to as K_β or M→L shell where the energy is referred to as L_α. Further designations are made as α_1, α_2, β_1 or β_2 to account for any higher or lower binding electrons present within the inner orbits of the shells. For instance, $K_{\alpha 1}$

and $K_{\alpha 2}$ emission lines arise from the decay of $2_{p3/2}$ and $2_{p1/2}$ electrons to the $1_{s1/2}$ orbit, respectively [126]. Thus, the emitted photons generate an X-ray emission spectrum where each element has a distinct spectral peak identifying it. Electrons transitioning from the *p* orbital to the innermost *s* orbital result in narrower spectral peaks while electrons transitioning from furthermost orbitals into the *s* orbital result in wider spectral peaks. The X-ray fluorescence emission spectrum is collected for each data point from a multichannel analyzer using a fast analog-to-digital convertor.

For the purposes of this study, we used an energy of 13,450 eV, an energy just below the K absorption edge of bromine (Br) which enabled us to map the distribution of elements from aluminum (Al) to Selenium (Se). In addition to the K-edge energy of Br, we also used a L_{α}-edge energy to map the distribution of iodine (I). The L_{α}-edge was used as iodine has a higher K-edge energy than Br. Along with mapping physiologically relevant elements, we were also interested in mapping iodine because every ischemic stroke patient is administered Isovue-300, an iodine based contrast agent during pre-procedural imaging as well as during the thrombectomy procedure. Thus, we used the contrast agent permeability as a biomarker to study thrombus perviousness where we associated increased iodine concentration with increased thrombus permeability.

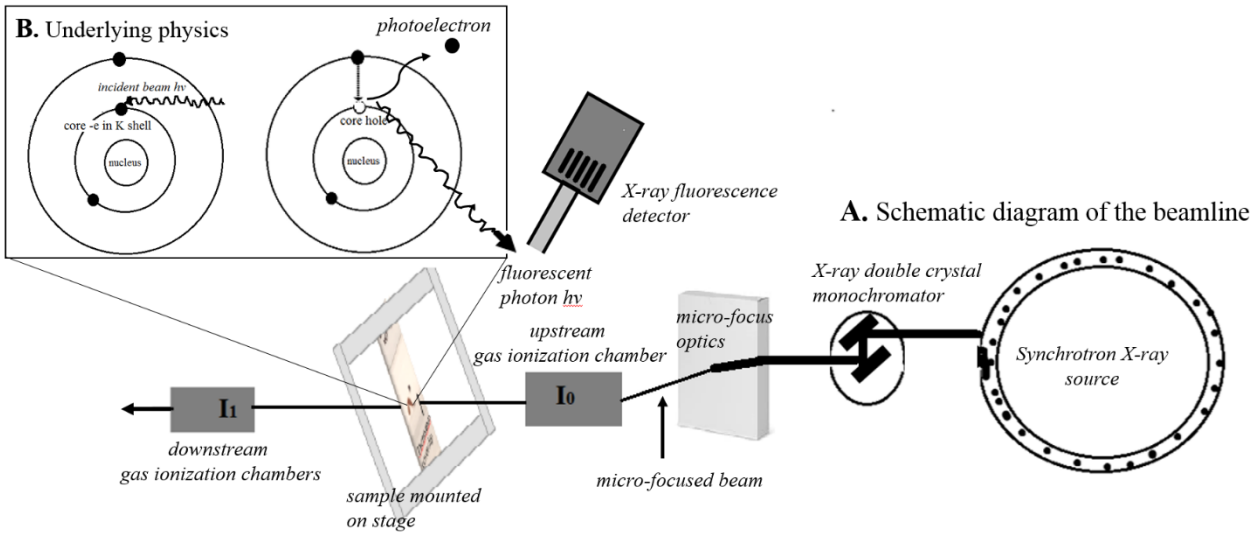

Figure 1-3: X-ray fluorescence imaging beamline components. (A) Simplified schematic diagram of the apparatus for conducting XFI at Stanford Synchrotron Radiation Lightsource. The beam is typically generated by a synchrotron radiation source and passes through downstream optical components shown in the schematic. The beamline is equipped with an X-ray double crystal monochromator, gas ionization chambers, XFI fluorescence detector and a precision stage to mount the samples on. (B) Schematic diagram of the underlying physics. The incident X-ray beam hits the sample and ejects the excited core electron as a photoelectron creating a core hole. The core hole is filled by an electron from an outer shell subsequently releasing a fluorescent photon. The fluorescent photons are detected by the XFI fluorescence detector. Figure adapted from Pushie *et al.* 2014 [127].

1.8.2 Sources of errors while quantifying samples using XFI

There are several factors that should be accounted for to achieve reliable quantification. Samples must be standardized and prepared under same conditions to achieve the same sample thickness when sectioned. Calibration foils must be run during each beamtime to detect any current fluctuations and the foils must not be damaged. Beamline settings must be standardized across beamtimes where the samples should be mounted at the same distance from the detector. Furthermore, parameters including resolution, dwell time and flux must be kept constant during each beamtime. Resolution measures the clarity in the number of pixels used to display an image. Low resolution images are often referred to as pixelated or blurry. Resolution depends on spot size (size of the beam) and step size (size of the pixel) whereby, if the spot size > step size,

the tissue is oversampled while if the spot size < step size, the tissue is under sampled [128]. Dwell time measures the amount of time spent scanning each pixel while the flux measures the amount of photons emitted. Increase in dwell time or flux, can oversaturate the detector.

1.8.3 Benefits and limitations of Synchrotron-based XFI

There are several advantages of using synchrotron-based XFI imaging over conventional laboratory-based techniques. For instance, XFI enables us to quantify elemental concentration and visualize the distribution of multiple elements simultaneously. Furthermore, based on the preliminary spectrum, we can combine fluorescence imaging with micro X-ray absorption spectroscopy to visualize specific molecular forms/oxidation states of a single element. XFI techniques are far more beneficial than histological stains developed to characterize different molecular states of elements such as; von Kossa for Ca^{2+}, an indirect calcium stain where silver nitrate reacts with calcium phosphate in the presence of illumination resulting in precipitation of silver phosphate; Perls' Prussian blue for ferric iron (Fe^{3+}); and modified Turnbull for ferrous iron (Fe^{2+}) [129]. When performing histology, samples undergo rigorous steps during fixation, processing and staining which potentially risk washing out elemental components. On the other hand, XFI techniques measure intact tissues with minimal to no pre-treatment, thereby eliminating the risk of losing any information on labile elements and molecules. Additionally, XFI can detect elements in very small samples with high sensitivity and resolution. Compared to benchtop sources, synchrotron-generated beam is: 1) extremely bright which reduces dwell time and increases the scanning speed, 2) monochromatic which yields in robust quantification, and 3) tuneable which probes chemical speciation [130]. That being said, XFI techniques have certain limitations as well. While hard X-ray beamlines show distinct spectra for high Z (atomic number) elements, emission lines for some of the low Z elements such as Ca and K overlap.

Similarly, for low Z elements, the penetration depth of the beam is limited and only enables surface mapping.

1.9 Principles of Spectroscopy

1.9.1 X-ray absorption spectroscopy

X-ray absorption spectroscopy (XAS) techniques have proven useful for determining the local geometric and electronic structure of molecules to understand chemical speciation of a particular element [131]. XAS can deduce the local structure of atoms because the wavelengths are on the same order of magnitude as the atom-atom separation in molecules. Because the ionization of core electron requires high energy in the X-ray range and spectroscopy requires a continuous energy-spectrum, XAS techniques are conducted using synchrotron sources. However, one of the primary concerns of XAS techniques include photo-oxidation/photo-reduction induced damage of the samples due to high beam intensity [127]. Similar to the principles of XFI, in XAS, the synchrotron beam is absorbed by an electron in the core shell (1s or 2p), thereby ejecting the core electron as a photoelectron *via* the photo-electric effect into an unbound state called continuum or is excited and promoted to a higher unoccupied level. XAS is element-specific because each element has a unique absorption edge. The absorption edge is the energy required to ionize the atom at its core level causing a steep increase in the absorption [131]. When the core electron is ejected, the core hole is filled by an electron from a higher energy state that falls into the vacant spot, thereby either releasing a photon (fluorescence emission) or emitting an Auger electron [124].

XAS measures the transitions from core electronic states to the excited states and the continuum. These measured transitions are represented by two main regions in the XAS spectrum, X-ray absorption near-edge spectra (XANES), and extended X-ray absorption fine structure (EXAFS).

The range of XANES lies between the threshold energy (E_0), energy at which the photoelectron is ejected to a continuum, and where EXAFS begins. XANES represent the fingerprint region that provides chemical information about the oxidation states in addition to the symmetry and local geometry around the absorbing atom [132]. On the other hand, EXAFS provide information on specific chemical species present in the sample and are sensitive to: 1) the distance between the absorber atom and the backscatterer atoms, 2) to the number of electrons around the backscatterer atoms, and 3) number of backscatterer atoms of a particular type. However, EXAFS do not provide information on the geometry of the molecule or distinguish between similar backscatterer atoms. EXAFS oscillations are produced by constructive and destructive interference patterns that arise from the interactions between the absorbing atom and the photoelectron waves backscattered by neighbouring atoms [131]. The amplitude of the EXAFS oscillations are directly proportional to the size and number of backscatterer atoms. To extract information from EXAFS on bond distances as well as number and types of backscatterer atoms, the EXAFS can be Fourier-transformed [133].

The spectroscopy beamline 7-3 at SSRL consists of similar beamline components as XFI beamline, with a few additional components [134]. The beamline is equipped with a 30-element Germanium solid-state detector (*Mirion technologies Inc., Canberra, Australia*) placed at a 90° angle to the incoming X-ray beam to reduce the detection of scattered radiation and measure the primary fluorescence excitation spectrum. Unlike the XFI beamline, the XAS beamline does not use a fixed incident energy as each element has a unique absorption edge. Thus, the monochromator and 30-element Ge detector needs to be calibrated and optimized for each element separately. Furthermore, a set of elemental filters and Soller slits are placed between the sample and the Ge detector to filter out elastic scatter and Compton radiation scatter, and prevent

oversaturation of the detector by blocking most of the stray fluorescence. It is essential to select an X-ray filter with an element that has an atomic number of one less than the sample (Z-1). The sample is placed in an Oxford He cryostat. There are 3 gas ionization chambers used at the 7-3 beamline to monitor the beam at different positions. The first chamber (I_0) is placed before the sample to measure initial beam flux, the second chamber (I_1) is placed between the sample and the metal foil to measure transmitted beam flux and the third chamber (I_2) is placed after the metal foil to absorb as much of the remaining beam as possible. The metal foil is used for calibrating the monochromator energy and prevent it from drifting. In addition to the ionization chambers, the beamline is also equipped with Passivated Implanted Planar Silicon (PIPS) detectors to monitor fluorescence. Figure 1-4 illustrates a schematic representation of the spectroscopy beamline 7-3 at SSRL.

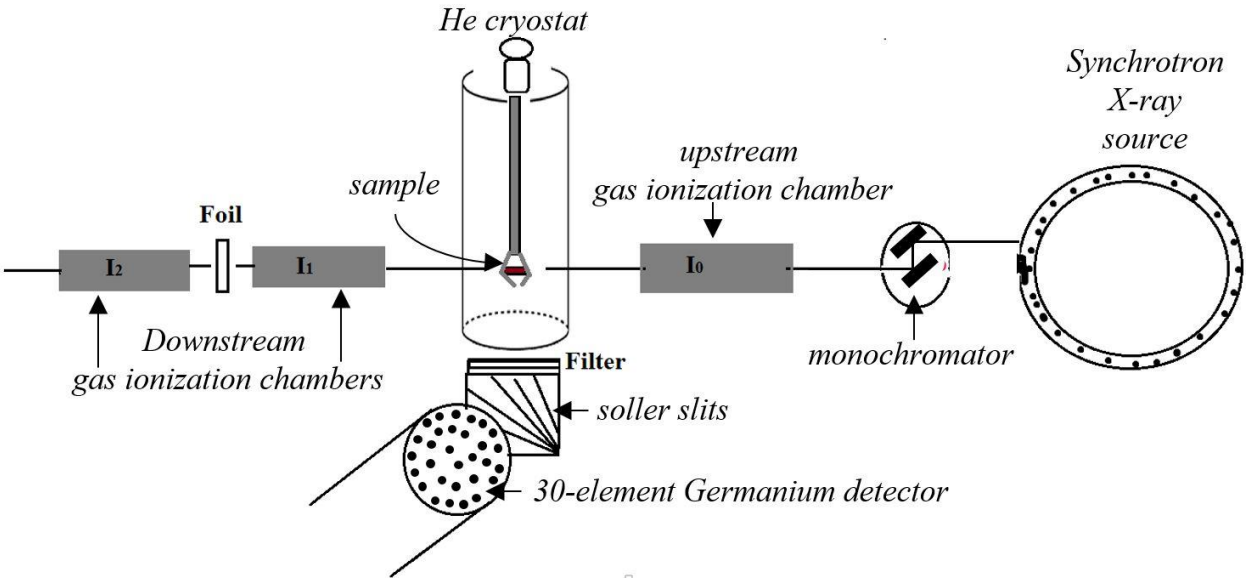

Figure 1-4: X-ray absorption spectroscopy beamline components. Simplified schematic diagram of the apparatus for conducting XAS at the 7-3 beamline at Stanford Synchrotron Radiation Lightsource. The beam is generated by a synchrotron radiation source and passes through the downstream optical components shown in the schematic. The beamline is equipped with an X-ray double crystal monochromator, 30-element Ge solid state detector, gas ionization chambers, Oxford He cryostat, filters, foils and Soller slits. Figure adapted from [https://www-ssrl.slac.stanford.edu/mes/XAFS/INDEX.HTML].

1.9.2 Fourier-transform infrared spectroscopy (FTIR) – Mid Infrared spectroscopy beamline components

Infrared imaging for this study was conducted at the Mid-IR spectroscopy beamline at the Canadian Lightsource (CLS). The beamline includes Fourier transform infrared (FTIR) spectrometer and microscope which supplies diffraction-limited spatial resolution at a wide range of energy in the mid infrared range (*i.e.* 3-50 μm) [135]. This wide energy range is a fingerprint region used for molecular identification. Imaging at this beamline can be conducted by either using a globar source or a synchrotron source. A globar is a thermal light source with a silicon carbide rod that is electrically heated up to 1,000-1,650°C [135] to produce radiation.

The beam goes through 1) collimator, a device that produces parallel beams of rays, and 2) aperture wheel which enables users to select a slit size that adjusts the beam size and spectral resolution. Narrower slits may be useful for lowering background but could result in undersampled spectra while wider slits may be used for coarse scans but would compromise resolution.

Once the slit size on the aperture wheel is selected, and the beam passes through it, the beam gets focused and narrow. It hits a collimating mirror that directs the beam onto a straight path into a FTIR interferometer. The FTIR interferometer is an optical instrument that measures wave interference of two beams. The interferometer contains beam splitters, which are devices designed to split the beam into two. The material generally used for a beam splitter is potassium bromide (KBr) [135]. Using KBr mirrors have few advantages including, they have a wide wavelength range for infrared radiation transmission, they prevent large absorption within the range, and they have a small refractive index. Interferometers contain a fixed mirror and a moving mirror [135]. As the beam passes through the beam splitter and splits into two beams,

one of the beams hits the moving mirror while the other beam hits the fixed mirror. The beam bounces back and forth and as a result, some of the rays are lost along the way. Eventually, the two beams bouncing back and forth from the mirrors combine to create either constructive or destructive interference patterns. Constructive patterns are formed when the two waves are in phase with each other and additive, thereby intensifying the wave. In addition, in constructive wave patterns, the distance from the beam splitter to the moving mirror is equal to the distance from the beam splitter to the fixed mirror. On the other hand, destructive patterns are formed when two waves are out of phase and therefore the resulting additive wave is less intense. To measure the mirror distance and the exact energy calibration, the interferometer has a built- in helium-neon (He-Ne) laser to send measurements to its own separate detector [135]. Once the rays pass through all the optical components, the resulting beam is focused, collimated, and combined. The beam hits the sample mounted under the microscope. The microscope is attached to a Focal Plane Array (FPA) detector. The FPA detector is cooled using liquid nitrogen to detect photons with higher sensitivity at infrared wavelengths.

Molecules within the sample vibrate at 6 different vibration modes including; 1) symmetrical stretching, 2) asymmetrical stretching, 3) wagging, 4) rocking, 5) bending, and 5) twisting [136]. Molecules with N number of atoms have 3N-5 vibrational modes if they are linear molecules and 3N-6 vibrational modes if they are non-linear molecules [136]. When infrared radiation matches the frequency of the vibrational modes, the bonds between the molecules absorb the wavelength and go into a higher energy vibrational state.

Because the samples are measured in transmittance mode, the FPA detector detects photons that are transmitted through the sample rather than detecting photons that have been absorbed by the

bonds. According to Beer-Lambert law, absorbance (*A*) and transmittance (*T*) are measured as follows [135]:

$$A = \varepsilon l c$$
$$T = 10^{\varepsilon l c}$$

where molar absorptivity is denoted by ε, tissue thickness is denoted by l and tissue concentration is denoted by c. Absorption of photons is directly proportional to all three parameters.

The spectral peaks produced are representative of the functional groups that are present in the samples. In other words, different functional groups present in organic molecules absorb specific wavelengths which are measured in wavenumber (cm^{-1}) where 1 μm = 1,000 nm = 10,000 cm^{-1}. Molecules absorbed in the mid-IR range have spectral peaks that range from 4000-200 cm^{-1}. We were specifically interested in analyzing the distribution of lipids – 1715-1755 cm^{-1} (>C=O stretching of lipid esters), glutamate – 1565-1590 cm^{-1}, amide I band – 1610-1710 cm^{-1} (C=O hydrogen bonded symmetrical stretching), amide II – 1520-1560 cm^{-1} (C-N stretching or N-H and CH_2 bending vibrations), platelets – 2905-2944 cm^{-1} (–CH_2 symmetrical stretches of lipid acyl chains in platelets), fibrinogen – 1390 cm^{-1}, and cholesterol esters – 2960 cm^{-1} (C-H asymmetrical stretching of methyl groups found in fatty acids, phospholipids and cholesterol esters) [137]. These molecules were mapped as they are physiologically relevant for blood composition and are known to be affected during ischemia. The spectral range for each of these peaks were determined either by directly identifying the peaks present in the samples using Orange software or by using reference peaks from previous literature in which bands pertaining to fibrinogen, hemoglobin, erythrocyte membrane lipids (cholesterol ester) and other plasma proteins were identified in whole blood samples and its constituents [137].

1.9.2.1 Globar *versus* Synchrotron source

The development of FTIR was followed by the development of IR spectrometers over three generations. The FTIR spectrometer was a third generation model which was defined by an inbuilt interferometer [135]. The FTIR spectrometer and microscope at the Mid-IR beamline at the CLS are setup to function with either a synchrotron or a globar radiation source. FTIR performed with a synchrotron source generates 100-1000× higher brightness and yields in smaller regions to be probed as opposed to a globar source. In addition, other advantages of using a synchrotron source includes pulsed time structure, higher degree of polarization, and improved signal-to-noise [138], [139]. While the synchrotron does provide more advantages than a globar source, it does have some disadvantages as well. For instance, technical issues that result in beam shut-down affect experiments and data collection, and since raster scanning is time consuming, it is only practical to scan smaller regions. For samples that are scanned at a spatial resolution of ≥ 20 μm, the globar source is sufficient for providing good resolution, sensitivity and brightness [138].

1.10 Study goals, research questions, and hypothesis

The aim of this study was to characterize thrombus composition using multimodal imaging tools which combined conventional histochemical techniques with advanced-synchrotron based XFI and FTIR techniques to answer the following research questions:

1. Does stroke etiology influence thrombus composition?
2. Does thrombus composition affect stroke severity, recanalization success, choice of thrombectomy device, and 90-day functional outcomes?
3. Does choice of thrombectomy device and recanalization success affect 90-day functional outcomes?

4. Does elemental or organic biochemical composition of thrombus correlate with stroke etiology or 90-day functional outcomes?
5. Does thrombus perviousness correlate with stroke etiology or clinical parameters?

We hypothesized that; 1) there is no significant difference in composition between cardioemboli and artery-to-artery emboli, 2) thrombus composition would not be one of the factors in affecting stroke severity or EVT outcomes, 3) ADAPT would work better in retrieving erythrocyte-rich thrombi, and 4) artery-to-artery emboli would have higher distribution of heavier biological elements such as Fe, and Cu. To investigate the proposed research questions, we analyzed the composition of freshly retrieved thrombi using multiple imaging techniques including; X-ray fluorescence imaging, Fourier transform infrared spectroscopy, conventional histology and immunohistochemical techniques, and retrospectively correlated compositional findings with clinical and interventional outcomes.

Chapter Two: Methodology

2.1 Demographic and clinical characterization of patients

Between September 2017 and January 2019, we enrolled 28 patients with AIS who received EVT at Royal University Hospital (RUH), Saskatoon, Saskatchewan Canada. The study protocol was approved by the Biomedical Research Ethics (Bio-RED) Board of University of Saskatchewan (internal ID 17-196). For this particular study, the inclusion criteria included participants with AIS ≥18 years old, in whom intracranial hemorrhage had been ruled out. Patients gave informed consent for the study prior to hospital discharge. If patients were unable to give consent, a family member consented on their behalf. However, we attempted to reconsent the patient when they became able to sign.

During clinical evaluation, information on stroke presentation, including date, time, and symptoms of stroke onset, were collected. There are two common sources of origin for thrombo-emboli that cause ischemia, proximal arteries (artery-to-artery embolism) or the heart (cardioembolism). For some patients that presented at the emergency with an unknown cause (*i.e.* etiology) of stroke, the CTA was used to identify the possible cause: if carotid stenosis (*i.e.* narrowing of the carotid) was observed on the CTA, the etiology for ischemia was considered to be an artery-to-artery embolism; if carotid stenosis was not observed, the etiology for ischemia was considered to be cardioembolism **(Fig. 2-1)**. In addition, the patient's medical records were reviewed to determine stroke etiology. Conditions such as atrial fibrillation, valvular heart disease, large artery atherosclerosis, or any other condition of immediate concern to stroke were all taken into consideration. We also collected every participant's smoking status, medical history, and medication history from 30 days prior to hospitalization until they were discharged. All medications were documented. If participants were administered specific pre- or post-

procedural medications, including anti-coagulants, thrombolytics, or platelet aggregating inhibitors, this information was collected. We collected information on the location of large vessel occlusion, collateral flow status, thrombus density sign, surgical outcomes including the type of interventional technique performed (*i.e.* angioplasty, direct contact aspiration and use of stentrievers) and all surgical devices used during each approach. Specific stroke scores including their Thrombolysis In Cerebral Infarction (TICI), Alberta Stroke Program Early Computed Tomography Score (ASPECTS), pre- and post-treatment National Institute of Stroke Scale (NIHSS), and 90-day modified Rankin Scale (mRS) were collected as well.

Figure 2-1: Carotid Stenosis. Computed Tomography Angiography (CTA) performed on patient using Isovue300 contrast agent. Angiogram shows carotid stenosis (indicated by arrow). Angiograms were used for identifying stroke etiologies for those patients who we had no information on at the time of admission. Presence of stenosis indicated artery-to-artery embolism and absence high grade stenosis indicated presumed cardioembolism.

2.2 Acute intervention and mechanical thrombectomy procedure

2.2.1 Neurological examination and Stroke Score Assessment

Emerging laboratory work and neurological assessment was performed for all stroke patients arriving in RUH. During neurological examination, patients were assigned a pre-treatment National Institute of Stroke Scale (NIHSS) score. Following that, pre-procedural Non-Contrast Computed Tomography (NCCT) was performed to rule out hemorrhagic strokes and assign an Alberta Stroke Program Early Computed Tomography Score (ASPECTS). Furthermore, pre-procedural CTA confirmed the presence and location of large vessel occlusion, and collateral flow status. Additionally, Thrombolysis In Cerebral Infarction (TICI) scores were collected post-recanalization. All the clinical and radiographic scales used in the study patients are defined below.

2.2.1.1 NIHSS SCORE

The NIHSS scores range from 0 to 42, where a score of 1 is defined as a minor stroke whereas a score of 42 is defined as a severe stroke. The NIH scale assesses and scores a number between 0 and 4, 0 indicating normal functioning and 4 indicating complete impairment, in each of the following categories; level of consciousness, horizontal eye movements (gaze), visual fields, facial palsy, arm movements, leg movements, limb ataxia, sensory deficits, aphasia (language), dysarthria (slurred speech), and neglect (extinction and inattention) [140]. The final NIHSS scores are calculated by adding scores from each individual category. For bar graphs showing correlations between stroke severity and clinical outcomes, a NIHSS of 10 was used as a cut-off score because, previous studies had shown a score ≥ 10 as a cut-off point for differentiating a minor-to-moderate stroke from a moderate-to-severe stroke [141], [142].

2.2.1.2 ASPECTS SCORE

ASPECTS is a 10-point quantitative scoring system used for evaluating the volume of cerebral infarction on NCCT. The score was developed to assess early ischemic changes in regions distributed over the MCA territory. To compute the ASPECT score, 1 point is subtracted from the initial score of 10 for every region involved. The 10 regions assessed are: 1- frontal operculum (M1), 2- anterior temporal lobe (M2), 3- posterior temporal lobe (M3), 4- anterior MCA territory (M4), 5- lateral MCA territory (M5), 6- posterior MCA territory, 7- caudate, 8- lentiform nucleus, 9- internal capsule, and 10- insular cortex [143]. Variations in the ASPECTS scoring system arise when assessing lesions in the posterior circulation. For example, 1 point is deducted for lesions of the thalami, occipital lobes, and cerebral hemispheres, and 2 points are deducted for lesion of the midbrain or pons [144]. Refer to *section 1.1* for detailed information on the cerebral vasculature. Different institutions employ different modalities for assessing ASPECTS. For example, a study by Molina *et al.* assessed ASPECTS using diffusion-weighted imaging [145] while a study by Campbell *et al* used infarction volume on cerebral blood flow by perfusion CT [75].

2.2.1.3 TICI SCORE

TICI is intended to standardize scoring of the angiographic outcomes by evaluating reperfusion and recanalization success in response to thrombolytic therapy [146]. The evaluation categories span from no perfusion to complete perfusion where, grade 0 indicates no reperfusion; 1 indicates incomplete or partial reperfusion with no distal flow; 2a indicates incomplete or partial reperfusion with incomplete (< 50%) distal flow; 2b indicates incomplete or partial reperfusion with incomplete (> 50%) distal flow; 2c indicates near-to-complete reperfusion; and 3 indicates full reperfusion with complete distal flow. Even though the TICI scoring system is criticized for

its internal inconsistencies and arbitrary scale, it is still widely used and accepted in medical literature [146].

For bar graphs showing correlations between TICI and other clinical outcomes, TICI scores were grouped in either of the two categories (TICI 1-2a or TICI 2b-3) to differentiate incomplete or partial recanalization from near-to-complete recanalization. Participants in whom no recanalization (TICI 0) was obtained, were excluded from this study as there was no thrombus sample retrieved from those patients to analyze.

2.2.2 Endovascular therapy: thrombectomy procedure

To be eligible for mechanical thrombectomy, AIS patients had to meet specific clinical and radiographic inclusion criteria including; 1) NIHSS > 5, 2) ASPECTS > 5, and 3) confirmation of large vessel occlusion on CTA. Of all the patients enrolled in this study, who had a large vessel occlusion, 14.3% (4 out of 28) of AIS patients received IV-tPA prior to mechanical thrombectomy. CTA was performed using Isovue300 (Iopamidol injection 61%; *Bracco Diagnostics Inc.*), an iodine-based contrast agent. Prior to starting the thrombectomy procedure, patients were either administered local anaesthesia - lidocaine with conscious sedation, or a general anesthesia.

Thrombectomy procedure: In all cases, a right 5 French femoral artery sheath and a 5 French diagnostic catheter was placed over a 0.35” wire into the affected parent artery. After running diagnostic angiography, the diagnostic catheter was exchanged for a 6F sheath (Neuron Max; Penumbra Inc., California USA), to provide robust intracranial support. A Velocity microcatheter (Penumbra Inc., California USA), and Synchro 2 standard or Fathom microwires (Neurovascular, Michigan, USA; and Boston Scientific, USA) were advanced into and across the occluded vessel. In some cases, small doses of intra-arterial verapamil were infused to prevent

catheter-induced vasospasm. Thrombectomy was performed using either stentrievers or direct contact aspiration. Commonly used stent-retrievers included: Platinum Solitaire Revascularization device 6×40mm or 4×40mm (Medtronic Inc., Irvine, California, USA), Trevo XP 6×25mm (Stryker Inc., Michigan, USA), and Penumbra 3D Separator (Penumbra Inc., California, USA). For aspiration, a large bore aspiration catheter, Ace 68 (Penumbra Inc., California, USA) was placed at the thrombus face. The catheter was attached to the aspiration tube and Pump MAX vacuum (Penumbra Inc., California, USA). If aspiration alone was unsuccessful, then a combination technique called Solumbra was used. In this technique, the stent-retriever was delivered through the reperfusion catheter [147]. All procedures were performed using biplane angiography and roadmapping. To secure closure of the femoral artery, StarClose SE Vascular Closure System was used. The retrieved thrombus sample was then sent to the laboratory for further analysis within 30-60 minutes of retrieval.

2.2.3 Post-thrombectomy care and evaluation

Some patients received anticoagulants or anti-platelet drugs such as heparin, Clopidogrel (Plavix), Abciximab (Reopro) or verapamil (calcium channel blocker) post-thrombectomy. Long-term clinical conditions for patients were assessed using the modified Rankin Scale (mRS) and NIHSS, 90 days after discharge by means of a hospital visit by a neurologist, who was not aware of the treatment assignments, and who had specific training and certification in stroke outcome assessment. Modified Rankin Score (mRS) evaluated their neurologic disability which was scored from 0 to 6, where a score of 0 meant no symptoms while 6 indicated death.

2.3 Thrombus sample collection and processing

Freshly retrieved thrombi were cut in half where one half of the thrombus was brought to the pathology department (RUH and City Hospital, Saskatchewan, Canada) to be formalin fixed,

paraffin embedded and stained with H&E, Masson's Trichrome, factor VIII/von Willebrand factor (vWF), CD31, and CD68. The other half of the thrombus was transported to our laboratory where we flash froze the thrombus in 2-methylbutane (isopentane) and stored it at -80°C until sectioning. The flash frozen samples were serially cryosectioned for XFI and FTIR analysis. Since both XFI and FTIR techniques measure labile elements and molecules, it was essential to flash freeze and leave the samples untreated, unlike paraffin embedded sections, to prevent any alterations or changes in biochemical information. Alternatively, for histological analysis, we used the paraffin sections produced by the pathology laboratories in RUH or City Hospital, rather than cryosections because cellular morphology was better preserved in paraffin sections.

2.3.1 Paraffin embedding and sectioning

Fresh thrombus samples were fixed in 10% formalin for 2 hours, placed in embedding cassettes, and embedded in paraffin wax. To remove water from within the cells, the samples were dehydrated in 70% ethanol, 1 change, 1 hour, 95% ethanol, 2 changes, 1 hour each and 100% ethanol, 3 changes, 1 hour each. Alcohol and wax are insoluble together. Thus, alcohol must be replaced with an intermediate solvent which is miscible in both alcohol as well as paraffin wax. The intermediate solvent is called a clearing agent because it imparts transparency on the tissue due to its high refractive index [148]. The samples were cleared in Xylene, 2 changes, 1 hour each. Lastly, to infiltrate wax into the cells, tissues were incubated in liquid wax at 60°C, 3 changes, 1 hour each.

Once the tissues were completely infiltrated in wax, embedding blocks were prepared for sectioning, by orienting the tissue and pouring molten wax into the mold over the tissue sample. Once the wax block hardened, paraffin blocks were sectioned using a microtome. Ribbons of

5μm thick sections were floated in a 40-45°C water bath and sections were mounted on slides and dried overnight in a 35°C oven.

Prior to performing any histology or immunohistochemistry, paraffin embedded sections were deparaffinized in xylene and hydrated by incubating in 100% ethanol, 70% ethanol and then distilled water.

2.3.2 Flash freezing and cryosectioning

As previously mentioned, for the purposes of this study, freshly retrieved thrombi were processed in two ways, where one half of the thrombus was formalin fixed, and paraffin embedded to preserve cellular morphology while the other half was flash frozen to prevent the loss of labile biochemical information.

Samples were placed in an OCT embedding matrix prior to flash freezing to prevent fragmentation and sectioning artifacts. 2-methylbutane (Fisher; 03551-4) was used as a flash freezing agent, as it froze the samples quicker than liquid nitrogen alone and prevented ice-crystal formation. The samples were flash frozen within 30-60 minutes after being retrieved out of the patients and cryosectioned at -20°C using a cryomicrotome (Avantik) at 7μm thickness for histology (H&E), and FTIR analysis, and 30 μm for XFI. Sections produced for histology and FTIR analysis were stored in a -80°C freezer while sections produced for XFI analysis were stored at room temperature until imaging. Even though cryosections were mainly produced for FTIR and XFI analysis, we were keen to determine whether thrombus components such as erythrocytes or fibrin contributed to specific distribution patterns or co-localization of elements and macromolecules. Thus, adjacent sections to FTIR and XFI were stained with H&E and Martius Scarlet Blue.

Note: The flashing freezing window was established by conducting an experiment which tested the effects of different freezing time-points, including; 5 mins, 15 mins, 30 mins, 1 hr, and 2hrs on the quality of our samples. While literature recommended for blood samples to not sit at room temperature for more than 15 mins, as it compromised blood integrity, processing the thrombus sample within 15 mins of retrieval was not feasible for us. Thus, taking transportation and preparation times into account, we established 30-60 mins as our flash-freezing window.

2.3.3 Histology

Histology and immunohistochemistry techniques on paraffin sections were performed by the histology technicians in RUH or City Hospital pathology laboratory. 5μm paraffin sections were stained with H&E, and Masson's Trichrome and immunolabelled with factor VIII/vWf for platelets (rabbit polyclonal anti-human; Dako Agilent), CD31 for endothelial cells (mouse monoclonal anti-human; Dako Agilent), and CD68 for macrophages (mouse monoclonal anti-human; Dako Agilent M 0876). Histology on frozen sections were performed in our laboratory. 7 μm frozen sections were stained H&E and Martius Scarlet Blue. Detailed protocol of all the histological stains and immunohistochemistry performed on paraffin and frozen sections are given below.

2.3.3.1 Hematoxylin and Eosin (H&E) – coverstainer process for paraffin sections

After deparaffinization, sections were placed in Hematoxylin (S330230-5; Agilent) for 45 seconds to stain the nuclei, then rinsed in distilled water for 1 min and stained blue in a blue buffer for 1 min (IBF-100; Agilent) to convert the soluble red stain within the nucleus into an insoluble blue stain. Sections were then washed in tap water and differentiated in 70% alcohol for 1 min, followed by counterstaining in Eosin for 1.5 mins to stain the cytoplasm and

erythrocytes. Finally the sections were dehydrated in 4 changes of 100% ethanol, and cleared using Histoclear (NDIHS-200, Diamed), and then coverslipped.

> **Note:** Histoclear was used as an alternative to xylene as it prevented tissue brittleness, rendered fine details in nuclear morphology and improved H&E staining by yielding a brighter Eosin background [148].

2.3.3.2 Masson's Trichrome – for paraffin sections

After deparaffinization, sections were fixed in Bouin's solution for 12 minutes at 56°C, then rinsed in tap water to remove any excess yellow residues from the fixative and washed in distilled water for 2 minutes at 42°C. The entire staining process was automated using the Artisan Link process (AR17311-2; Agilent). Sections were incubated in Weigert's A/Weigert's B iron hematoxylin solution for 10 minutes to stain nuclear chromatin, then washed in tap water followed by a quick rinse in distilled water. Next, the sections were stained in Biebrich scarlet-acid fuchsin for 2 minutes to stain acidophilic cytoplasm and erythrocytes and differentiated in phosphomolybdic-phosphotungstic acid solution for 12.5 minutes at 40°C. Lastly, the sections were stained in aniline blue for 10 minutes at 35°C to stain fibrin, then washed in distilled water and differentiated in acetic acid for 3 minutes. Finally, the sections were dehydrated through 95% ethanol, 100% ethanol, then cleared in xylene and mounted using a resinous mounting media such as cytoseal.

> **Note:** the differentiation step in phosphomolybdic-phosphotungstic acid solution enabled a substitution reaction whereby the phosphomolybdic-phosphotungstic acid taken up by the fibrin was replaced by aniline blue to stain fibrin in blue.

2.3.3.3 Hematoxylin and Eosin – manual process for frozen sections

The H&E protocol used for staining frozen sections was different than that used for the paraffin sections wherein, the frozen sections were thawed and fixed in 4% paraformaldehyde (PFA) (J.T. Baker; S898-09) for 5 mins, then washed in 0.1M phosphate buffered saline (PBS) for 15 mins and stained in modified Harris hematoxylin (C.I. 75290) for 4 mins. The sections were then rinsed in 0.5% acid alcohol to remove excess hematoxylin and stained in 1.54% saturated aqueous lithium carbonate for 5 seconds to enhance blueing, followed by rinsing in running tap water for 3 mins. The sections were then counterstained in Eosin Y (C.I. 45380) working solution for 30 seconds which was prepared by adding 1 part stock solution (1.25% Eosin Y in 70% ethanol containing 1% glacial acetic acid) to 4 parts 70% ethanol. The sections were dehydrated through 70% ethanol; 95% ethanol (Commercials Alcohol; 001-02-17N), 100% ethanol (Commercials Alcohol; 106-02-17N), and then cleared in xylene (Fischer; X5-4). Samples were mounted in resinous mounting media, cytoseal (Richard-Allan Scientific; 8310-4).

2.3.3.4 Martius Scarlet Blue – manual process for frozen sections

The MSB stain was an alternative stain to the Masson's trichrome used on frozen sections for staining erythrocytes and fibrin. Sections were thawed and fixed in 4% paraformaldehyde for 5 mins, then washed in 0.1M PBS for 10 mins, followed by a quick rinse in distilled water. The sections were stained in modified Harris hematoxylin stain for 5 mins, then rinsed in 95% alcohol for 5 seconds to remove excess hematoxylin and then stained with 0.2% Martius yellow (Aldrich; 377767-25G) in 95% ethanol containing 2% phosphotungstic acid (Fischer Scientific; 12501-23-4) for 2 minutes to stain erythrocytes. The sections were then rinsed in distilled water and stained with 1% crystal ponceau 6R (Sigma; C0644-5G) in 2% glacial acetic acid (BDH; AC500-78) for 10 mins to stain fibrin, followed by a quick rinse in water and differentiation in

1% phosphotungstic acid for 5 minutes. The sections were rinsed in water and stained with 0.5% methyl blue (C.I. 42780; Fischer Scientific; 28983-56-4) in 1% glacial acetic acid for 2 minutes to stain collagen. Finally, the sections were dehydrated through 70% ethanol; 95% ethanol, 100% ethanol, and then cleared in xylene (Fischer; X5-4). Samples were mounted in resinous mounting media, cytoseal (Richard-Allan Scientific; 8310-4).

> **Note:** The MSB stain did not work on frozen sections despite our multiple attempts to modify and optimize the protocol with different incubation times, as well as using different types of fixatives including: 4% PFA, 10% formalin, acetone, methanol, and PFA vapours. Similarly, H&E stain did not work on the frozen sections. Most of the erythrocytes were being washed off in the solutions, compromising cellular features and misleading our interpretation. Furthermore, we also attempted to optimize the staining protocols on whole blood smears collected from mice to eliminate confounders, including product quality (which ensured that the staining products worked), and hemolysis (which determined if the stains only worked on whole blood cells as opposed to hemolyzed cells present in a thrombus). Despite optimizing the protocol with various tweaks, all attempts were unsuccessful. Thus, histological results of frozen sections were not included in the analysis and thesis. Instead, we solely used paraffin sections for correlating histological findings with clinical and interventional outcomes, as well as with XFI and FTIR outcomes. However, there was a limitation to this approach. The paraffin sections were not adjacent to the frozen XFI or FTIR sections. Nevertheless, since the paraffin and frozen sections belonged to the same thrombus, all analyses were performed in an extrapolative manner.

2.3.4 DAB chromogen immunohistochemistry for paraffin sections

All immunostaining procedures were performed on the Autostainer link instruments using Dako

EnVision Flex + detection system. After deparaffinization, and rehydration, sections underwent heat-induced epitope retrieval (HIER) using an enzyme pre-treatment procedure (water-bath method). Target retrieval solution (30 ml of 50× concentrate; EnVision Dako; K8004) was diluted with 1470 ml distilled water to obtain 1:50 dilution (*i.e.* 1.50L working solution containing Tris/EDTA buffer, pH 9). Agilent PT link tank was filled with 1.5 L of target retrieval working solution to ensure that all slides were completely immersed. The solution was preheated to 85°C. Deparaffinized, hydrated sections were incubated in the retrieval working solution of pH 9 at 97°C for 20 minutes. Sections were allowed to cool in the PT link tank to 85°C, and then rinsed in EnVision Flex wash buffer (K8007), 1:20 dilution containing Tris-buffered saline solution with Tween 20, pH 7.6, for 5 minutes.

After the HIER procedure, sections were blocked for 5 minutes using the ready-to-use zFLEX peroxidase-blocking reagent (SM801) to reduce non-specific background staining, which was then followed by a buffer rinse. Factor VIII/vWF and CD68 were immunolabelled using the Flex protocol whereas CD31 was immunolabelled using the Flex+ Mouse Linker protocol. Sections were applied with the following primary antibodies:

- Monoclonal mouse anti-human CD68 (M0876) diluted to 1:250 in ready-to-use antibody diluent (K8006)
- FLEX monoclonal mouse anti-human CD31 (IR61061-2) prediluted
- FLEX polyclonal rabbit anti-human vWF (IR52761-2) prediluted

Flex + Mouse linker protocol included an additional step after primary antibody incubation, where sections were treated with secondary antibody mouse linker for 15 minutes prior to polymer labelling as opposed to the Flex protocol where sections were directly labelled with polymer after completing their incubation in the primary antibody. The polymer-labelling step

was performed for 20 minutes using the ready-to-use zFLEX/HRP reagents (SM802) which consisted of a dextrane backbone to link up peroxidase molecules to the antibody molecules and amplify the detection signals. Sections were then rinsed in wash buffer several times for 5 minutes and treated with zFLEX DAB + Chromogen substrate working solution for 10 minutes which was prepared by adding 1 drop of concentrated DAB chromogen (EnVision Dako; DM827) in 1 ml substrate buffer containing hydrogen peroxide (EnVision Dako; SM803). Finally, the sections were counterstained with hematoxylin using the coverstainer process, and mounted using an aqueous mounting medium.

All the histology and immunohistochemistry slides were viewed and photographed using a Nikon light microscope (Royal University Hospital, Department of Pathology and Laboratory Medicine, Saskatchewan, Canada).

2.4 Histological analysis using ImageJ software

To classify a thrombus as either red (RBC rich) or white (fibrin rich), Masson's trichrome stained sections were quantified using ImageJ software [https://imagej.net/Fiji], where predominant regions stained with fibrin and erythrocytes were separated into red, blue and green channels using the software's trainable WEKA segmentation plugin [https://imagej.net/Trainable_Weka_Segmentation]. All images were acquired using the Nikon microscope under identical conditions where the automatic exposure and white balance were turned off. The images captured from the light microscope were stored in the 24-bit RGB and 1280 (width) × 960 (height) resolution.

In ImageJ (version 3.2.28), once the Masson's trichrome stained image was opened, the image was processed using the trainable WEKA segmentation (TWS) plugin. In the new trainable WEKA segmentation dialog box, the following steps were applied. First, three separate classes

were created: RBC regions, background, and fibrinous regions. Using different selection tools, regions of interest (ROIs) were traced and added into their respective classes. Traces for RBC regions were highlighted in red, background was highlighted in green, and fibrinous regions in purple. Then, we employed the "Gaussian blur" and "Differences of Gaussian" features to reduce image noise. All the other default training features were kept the same. Next, a probability map of each pixel belonging to its respective class was displayed as a 32-bit hyperstack representing the three channels (background, RBC traces, fibrin traces) in a black-white-gray colour hue.

Thresholding ROIs on the 32-bit hyperstack – Each of the 32-bit channels were manually adjusted using the "threshold" feature. The same threshold values were applied to every image.

RBC regions: upper slider – 0.45
lower slider – 1e30

Fibrinous regions: upper slider – 0.50
lower slider – 1e30

After thresholding each channel, the background pixels were set to not-a-number by selecting "set to NaN", which allowed us to convert the image into a binary black-white image which eliminated gray overlapping areas. The binary images could now be used for an area-based analysis to independently measure ROIs representing areas covered by red blood cells and fibrin **(Fig. 2-2)**. Raw values obtained for each thrombus were entered into an excel spreadsheet and converted into a percentage value (table 3-2) using the following formula:

$$\% \text{ RBC} = \text{RBC measured ROIs/total area} \times 100$$

$$\% \text{ Fibrin} = \text{Fibrin measured ROIs/total area} \times 100$$

The total area was obtained by adding the RBC and fibrin ROIs. Thrombi were classified as red if % RBCs > % Fibrin, or white if % RBCs < % Fibrin. In the case where patients had multiple fragments occluding their vessels, each of those fragments were sectioned serially, and labelled as section 1 (s1), section 2 (s2), section 3 (s3), and so on. During quantification, each of the

sections were separately quantified, and then added together to obviate bias, as shown in table 3-2. One of the patients (Pt 24) had two strokes in one day where one thrombus was retrieved from the left MCA and the other thrombus was retrieved from the right MCA. Even though the thrombi were retrieved from the same patient, they were treated as two separate samples. The quantification procedure was not blinded.

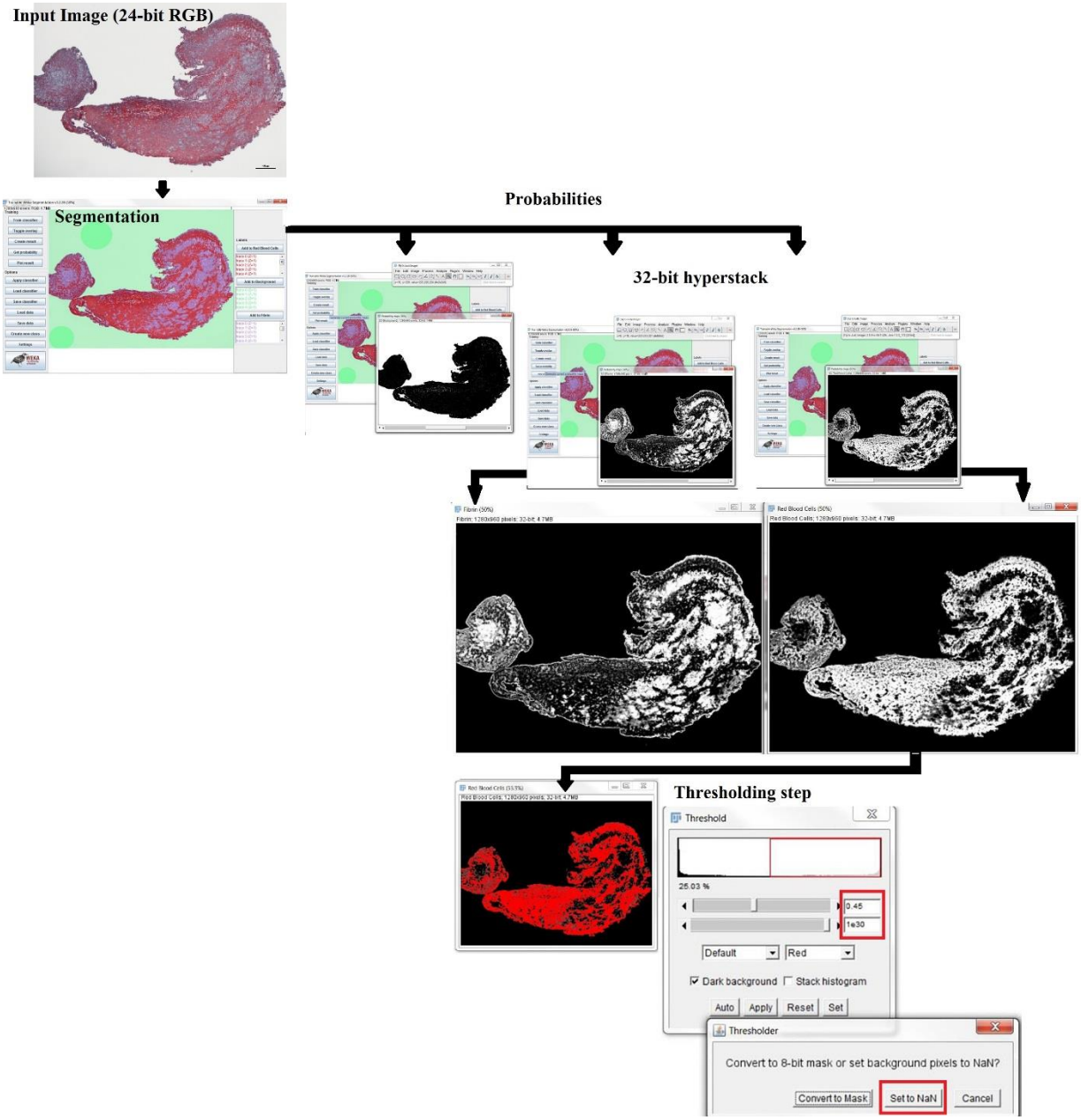

Figure 2-2: Flowchart of ImageJ analysis for histological quantification. A step-by-step protocol for quantifying regions of erythrocytes and fibrin on Masson's trichrome stained

sections of cerebral thrombi using the trainable WEKA segmentation plugin in ImageJ software. Traces for RBC regions were highlighted in red, background was highlighted in green, and fibrinous regions in purple.

2.5 X-ray fluorescence imaging

Samples were sectioned at 30 μm and collected on metal-free plastic Thermanox coverslips (Thermo Scientific). XFI took place at the SSRL where three imaging beamlines, 10-2, 2-3 and 14-3, were utilized. Beamline 10-2 was used to produce hard x-ray maps at an energy of 13,450 eV for mapping elements from Al-Se. Beamline 2-3 also used an incident energy of 13,450 eV to map elements from Al-Se at a higher resolution. Beamline 14-3 was utilized to produce soft x-ray maps at two different energies: 4,100 eV was used for mapping Al-Ca while 2,510 eV was used for mapping different sulfur species. Data for XFI was analyzed using Sam's Microprobe Analysis Kit (SMAK) [https://www.sams-xrays.com/smak] and ImageJ.

2.5.1 10-2 beamline setup and data analysis tools

An incident energy of 13,450 eV, just below the K-edge of Br, was used to map the distribution of a wide range of elements at their physiological concentrations including P, S, Cl, K, Ca, Fe, Cu, Zn, and I. Even though Na and Mg are biologically relevant elements, they were too low to observe in these experiments. The beamline set-up was similar to that described previously by Pushie *et al.* 2018 [149]. The beamline was running with SPEAR3 storage ring operating on a top-up mode at an energy of 3 GeV and current of 500 mA. All the data for this study was collected over two separate beamtimes. During one of the beamtimes, we used a 1-element detector, and collected fine scans at 200 ms dwell time and 30 μm stepsize. During our subsequent beamtime, we used a silicon vortex 4-element array detector (Hitachi High-Technology Science America, Inc., Northridge, CA) and collected fine scans at 100 ms dwell time and 30 μm stepsize. Beamline 10-2 employs a 33-pole, 1.27-Tesla wiggler, and 1.5 mrad

angular acceptance. The beamline used a Si(111) double crystal monochromator at phi=90° with a 1.2 m long horizontally and vertically collimating Rh coated bent cylindrical mirror (M_0). The beam was microfocused using a pinhole of 35 μm, set at an angle of 34°. The motor and ion channels were calibrated prior to the start of data collection. Samples were placed in an ambient temperature and mounted horizontally on a precision stage which was placed at a 45° angle to the silicon-drift vortex detector. For every sample, we collected coarse scans prior to the fine scans to assess the quality of the sample, measure X-Y coordinates required for fine scans, and estimate the amount of time required to run a fine scan for each sample.

Data was directly acquired from the SSRL server and analyzed using the SMAK software. Using this software, binned spectra of interested elements were fitted using the multichannel analyzer spectrum to yield in more accurate elemental quantification and improve signal-to-noise [149] especially for K and Ca. The K_α fluorescence emission lines for K and Ca overlap contributing to a falsely high measurement for Ca which is caused by X-ray fluorescence photons from areas with high K [149]. The fitted data was then quantified using calibration standards deposited on a 6.3 μm mylar film which enabled us to convert fluorescence intensities into areal concentrations ($\mu g/cm^2$). When elements of interest were fitted using the multichannel analyzer spectrum, we also included argon as one of the elements as argon is abundantly present in the atmosphere and should be accounted for during fitting. Elements mounted on the calibration standards had the following concentrations: Ca (CaF_2 foil, 56.8 $\mu g/cm^2$); K and Cl (KCl foil, 98.8$\mu g/cm^2$); Fe (Fe foil, 56$\mu g/cm^2$); Cu and S (CuS_x foil, 74.9$\mu g/cm^2$ and 21.0 $\mu g/cm^2$, respectively); Zn (ZnTe foil, 45.8$\mu g/cm^2$); P (GaP foil, 47.0 $\mu g/cm^2$); and I (RbI foil, 49.0 $\mu g/cm^2$).

In order to quantify the concentration of elements present in the sample, it was important to mask any background pixels contributing to false counts and only select the pixels representing the

sample. In SMAK, under correlation plots, we plotted sulfur and chlorine columns; however, any two columns can be plotted against each other. To select pixels representing the sample and mask any background pixels, a red polygon was traced over the region of interest. The pixels that were left out from the polygon (white arrow) indicated background pixels **(Fig. 2-3).** When the mask was applied to the image display, it only showed areas of the map where the selected correlation existed.

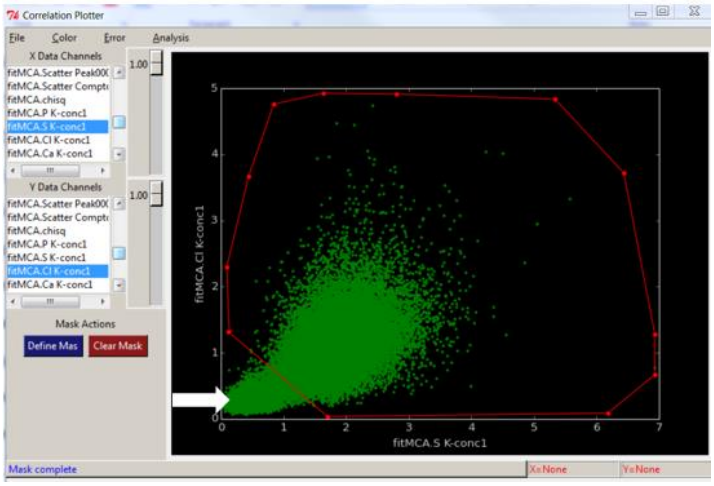

Figure 2-3: X-ray fluorescence imaging correlation plot. A correlation plot of sulfur and chlorine used for masking background pixels (white arrow) and selectively highlighting pixels that represent only the sample (red dotted polygon) in Sam's Microprobe Analysis Kit (SMAK).

A total concentration count (mean values) was acquired and the quantified data was exported into an excel spreadsheet and correlated with clinical outcomes. Along with the quantified data, heat maps were produced to visually assess regions containing high and low concentrations of elements present within the samples using rainbow pseudo-coloured maps. To obtain XFI heat maps, each of the previously fitted and quantified maps were smoothed using the blur feature which took Gaussian distribution of the area. The "filter size" was set to 5 which defined how many pixels were combined into one using 5×5 pixel area and the "std.dev" was set to 0.8. For each of the blurred maps exported to ImageJ as text images, the threshold intensities were set to the same values, and the final image panels were created using ImageJ and Adobe Photoshop CC 2018 (Adobe Systems, San Diego, USA).

2.5.2 2-3 beamline setup and data analysis tools

Higher resolution images of specific regions in the thrombus samples were captured using beamline 2-3 at an incident energy of 13,450 eV to image the distribution of P, S, Cl, K, Ca, Fe, Cu, Zn, and I. The beamline was running with SPEAR3 storage ring operating on a top-up mode at an energy of 3 GeV and current of 200 mA. Beamline 2-3 employs a 33-pole, 1.3-Tesla bend magnet, and 0.75 mrad angular acceptance. The beamline used a water cooled Si(111) double crystal monochromator at phi=90° with Kirkpatrick-Baez (K-B) mirrors directly imaging the bending magnet source. The microfocused beam size was approximately 2×2 microns. The motor and ion channels were calibrated prior to the start of data collection. Samples were placed in an ambient temperature and mounted horizontally on a metal stage which was placed at a 45° angle to the vortex silicon drift detector (Hitachi High-Technology Science America, Inc., Northridge, CA). For every sample, we collected coarse scans prior to the fine scans. Fine scans were collected at 100 ms dwell time and 2 μm stepsize.

All the data acquisition and analysis steps were similar to those described in the previous section where each of the binned elemental spectra were first fitted using the multichannel analyzer spectrum and then quantified using the calibration standard foils (mentioned in *section 2.5.1*), deposited on a 6.3 μm mylar film which enabled us to convert fluorescence intensities into areal concentrations (μg/cm^2). The quantified maps were then imported into ImageJ as text images where they were then applied with a jet colour scheme and set at the same threshold intensities. The final image panels were generated using Adobe Photoshop CC 2018.

2.5.3 14-3 beamline setup and data analysis tools

The beamline source was comprised of a bending magnet and employed a water-cooled Si(111) double crystal monochromator at phi=90° with a flat, bent, vertically collimating, Si-Ni coated

M_0 mirror and a toroidal, bent, 1.2 m Ni-coated M_1 mirror. Samples of 30 μm thickness collected on Thermanox coverslips were mounted on a circular metal disc and placed at 45° angle to the Vortex detector filled with liquid nitrogen. The samples are placed in a helium environment to reduce the relative oxygen content to < 0.5% and avoid X-ray attenuation of lower atomic elements (P-Ca) due to absorption by Ar, N_2 or O_2, and create an environment with zero humidity to maintain tissue integrity [150]. Prior to setting up samples, all the motors were aligned to ensure consistent current flux in the ion channels. In addition, the monochromator was calibrated using a sulfur standard at an energy of 2469.2 eV. For every sample, we collected coarse scans prior to the fine scans. Coarse scans were collected with a dwell time of 50 ms and stepsize of 200 μm while fine scans were collected with a dwell time of 100 ms and stepsize of 20 μm. An energy at the calcium edge, 4100 eV, was used for mapping the distribution of low Z elements: P, S, Cl, K, and Ca. Unlike beamline 10-2, beamline 14-3 uses a low incident energy to provide accurate quantification for low Z elements and prevent overlapping of the K and Ca spectral K-edge lines. In addition, since we were interested in mapping different sulfur species including sulfonic acid, sulfoxide and organic sulfate esters, we collected sulfur maps at various energies including; 2465 eV, 2469.85 eV, 2470.8 eV, 2470.55 eV, 2473.5 eV, 2475 eV, 2478.2 eV, 2479.8 eV, and 2510 eV (total sulfur map) [150].

Data was directly acquired from the SSRL server. Chemically specific sulfur images were produced using SMAK. All of the energies were imported into SMAK and smoothed using the blur feature which took Gaussian distribution of the area. The “filter size” was set to 5 which defined how many pixels were combined into one using 5×5 pixel area and the “std.dev” was set to 0.8. The background fluorescence map collected at 2465 eV was subtracted from each of the remaining energies. The newly generated channels were fit using standard model compounds

where the normalized fluorescence intensity values for the model compounds, sulfoxides (methionine sulfoxide), sulfonic acid (taurine) and O-linked sulfate ester (dextran sulfate), were recorded from Hackett *et al*. (Table S1) [150]. On the other hand, Ca maps were processed in the same manner as the 10-2 data, where the binned spectra for low Z elements (P, S, Cl, K and Ca) were fitted using the multichannel analyzer spectrum [149]. The fitted data was then quantified using the same calibration standards mentioned in the previous sections. To obtain heat maps, each of the quantified channels were imported as text images into ImageJ where the same threshold intensities were applied to every map represented by the jet colour scheme. The final image panels were generated using Adobe Photoshop CC 2018.

2.6 X-ray absorption spectroscopy

XAS spectroscopic analysis was conducted at SSRL using beamline 7-3 which utilizes an energy range between 5,000-35,000 eV to detect chemical forms for elements from Al-Se. However, we were only interested in analyzing the different oxidation states of Fe present in these thrombi since Fe is the most abundant element in erythrocytes. Thus, for Fe spectroscopy, we used an incident energy of 7,112 eV (Fe K-edge). The beamline was running with SPEAR3 storage ring operating on a top-up mode at an energy of 3 GeV and current of 100 or 200 mA. Beamline 7-3 employs a 20-pole, 2-Tesla wiggler, and 0.8 mrad beam. The experimental and beamline setup was adapted from George GN *et al*. [151]. The beamline was equipped with a 1 m long vertically collimating Si, Rh-coated bent mirror (M_0) placed upstream of the Si(220) double crystal monochromator at phi=90°. Samples were placed in 1 mm×12 mm plastic cuvettes which were wrapped with metal-free plastic Teflon tape and stored at -80°C. During data acquisition samples were placed in an Oxford Instruments CF1204 He cryostat at a 45° angle. For Fe spectroscopy, calibration was performed using a standard cuvette (300 µl of Fe citrate) and a Fe metal foil. The

monochromator and the detector were optimized for each element separately. The beam size was established based on the sample size, 1 mm×8 mm for the bigger cuvettes and 0.5 mm×6 mm for the smaller cuvettes. 30-element Ge detector was windowed using Ge30 plus software. Data analysis including calibration, averaging, splining and normalization of XANES was performed using the EXAFSPAK tool kit [https://www-ssrl.slac.stanford.edu/exafspak.html]. An X-environment, Xming [https://sourceforge.net/projects/xming/] was required to display the windows for running EXAFSPAK.

2.7 FTIR spectroscopic imaging

Samples for infrared imaging were sectioned at 7μm, collected on calcium fluoride (CaF_2) discs (Crystran, UK) and stored at -80°C until imaging. Mid-infrared beamline at the Canadian Light Source (CLS) was used for imaging the distribution of organic molecules. Samples were placed on the stage under a purge chamber to remove residual water vapour and increase the amount of light. Scans were collected after 15 minutes of purge. Globar-FTIR spectroscopic imaging was performed with a Cary 620 FTIR Microscope (Agilent Technologies, Inc.) fitted with an upper 15× magnification objective with a numerical aperture of 0.4. The microscope was equipped with a 128×128 FPA detector with the following parameters specified; speed = 2.5 kHz, interferogram sampling interval = 4, and 4 aggregated pixels for 15× magnification and 1 aggregated pixel for high resolution. This arrangement produced 2×2 binning for 15× magnification and 1×1 binning for high resolution. Images were acquired at a spectral resolution of 4 cm^{-1}. After correcting for non-uniformity, 64 scans of a background area were collected for subsequent background subtraction. After collecting background images, the region of interest was scanned.

Data for FTIR was analyzed and semi-quantified using Orange software (version 3.15.0) [https://orange.biolab.si/download/#windows]. In orange, once the workflow was opened, spectrum range for the following peak areas of interest were setup; lipids (1715-1755 cm^{-1}), glutamate (1565-1590 cm^{-1}), $–CH_2$ symmetrical stretches of lipid acyl chains in platelets (2905-2944 cm^{-1}), amide I bands (1610-1710 cm-1), amide II bands (1520-1560 cm^{-1}), C-H asymmetrical stretches of $–CH_3$ groups in cholesterol esters (2960 cm^{-1}), and fibrinogen (1390 cm^{-1}). Each sample files (.dmt format) were loaded one tile at a time and the preprocessed peak areas were automatically applied to each tile. For quantification, we manually selected multiple regions of interest (ROIs) from the edges as well as from the middle regions of the sample. The second derivative spectra were vector normalized and generated using 13 smoothing points Savitzky-Golay function [152] and inverted by multiplying the spectra with a value of -1. All the pixels in the selected ROIs were averaged for each peak area in absorbance units (A.U.) and represented in a table with their respective standard deviations. All the data tables were exported into an excel spreadsheet for further analysis. FTIR distribution maps were generated as .txt files using the program Datpush v2.0 [Pushie MJ, © 2018] where each individually extracted energy channel was imported into ImageJ, applied with the BGY colour scheme and set to the same threshold intensities. The final image panels were generated using Adobe Photoshop CC 2018.

2.8 Statistical analysis

Prior to performing statistics, it is important to choose an appropriate type of study design. Choosing the right study design determines the way in which a study is conducted, especially for ensuring appropriate sampling and data analysis that is intended to achieve reliable results as well as answer the research questions proposed in the study [153]. The two primary types of study designs include: experimental studies and observational studies. In scientific research,

experimental studies can be further categorized into controlled trials (randomized or non-randomized controlled trials) or uncontrolled trials while observational studies can be categorized into cohort studies, case-control studies or cross-sectional studies [154].

2.8.1 Use of parametric *versus* non-parametric tests

Statistics are used for presenting meaningful interpretations of the data, validating the hypothesis and providing correct conclusions for the study [155]. When data is interpreted, the *p*-value, an arbitrarily set value, determines the significance of the results and tests the validity of the predicted hypothesis. $P < 0.05$ means that there is less than 5% probability that the results obtained are due to chance alone, and the test is considered statistically significant [156]. Therefore, all statistical tests are designed to interpret the *p* value among other parameters such as: correlation coefficient (*r*) which provides evidence for how strongly two variables are associated with each other and indicates how changing one variable, changes the direction of the other variable without implying any prediction for the outcome variable; Odd's Ratios (OR) which measures an association between treatment and outcome variables to identify the odds that the outcome would occur; and 95% confidence intervals (CI) which provide a range of values to estimate precision of the mean.

Parametric and Non-parametric tests are two broad categories in statistics that encompass different types of tests that are designed to discover the trends in a population and state a general observation for the population (*e.g.* effects of drugs on a population) using a sample from the population. Because we use sample estimates to draw conclusions about a population, we use statistical procedures to estimate and validate the mean, standard deviation, and proportions [157]. Because we are interested in testing how far the sample mean of the data is from the true population mean, we use standard error of the mean (SEM) as opposed to using standard

deviation (SD) because SEM measures variability and dispersion of a sample mean around the true population mean, assuming that the data is normally distributed. An important distinction between parametric and non-parametric statistics is that parametric tests assume that the sample is normally distributed while non-parametric tests make no such assumptions and are therefore called “distribution-free”. In addition, parametric tests analyze group means while non-parametric tests analyze group median. Choosing the most appropriate statistical test depends on the following factors: 1) sample size, 2) types of variables, 3) type of study design (paired or unpaired), and 4) whether or not assumptions pertaining to that particular statistical test are satisfied [158], [159].

1. **Sample size (n):** for sample size < 25, non-parametric tests are better suited while for n > 25, parametric tests give stronger and valid results [160]. In general, parametric tests yield 5% more statistical power compared to non-parametric tests, but can only be used when the data is normally distributed [161]. Thus, in cases where the sample size is small, but the data is normally distributed, parametric tests have higher validity, and greater power to detect differences.
2. **Variable Types:** An independent variable, also known as a predictor variable, is a variable that is controlled or manipulated in a study to observe its effects on the dependent variable, which is also known as a response or outcome variable. The independent or the dependent variable can be measured either on a continuous or categorical level. A continuous variable can have infinite number of values between two given values as opposed to a categorical variable which only has a finite number of categories or distinct groups. A continuous variable can be further categorized as an interval or ratio variable. An interval variable is a measurement where the difference

between two values is considered meaningful and where the scale is void of true zero (examples: temperature in °C). On the other hand, a ratio variable encompasses the same properties as an interval variable; however, it is not void of absolute zero (examples: age, weight, height). Similarly, a categorical variable can be further categorized as an ordinal or a nominal variable. An ordinal variable is organized into ordered categories, where assigning ranks to the categories have meaning (*e.g.*: ranks such as 1^{st}, 2^{nd}, 3^{rd}, or educational experience which occurs in an order such as elementary school graduate, high school graduate, college graduate and so on). A nominal variable, is one that cannot be ordered or measured (*e.g.* sex, colours, marital status).

Before choosing a statistical test, one must identify the types of variable being investigated to answer the research question.

3. **Type of study design:** In scientific experiments, data analysis often involves comparing two or more sets of data. If the data is obtained from a single subject at different time points (*e.g.* comparing blood pressure values before and after administering a drug), the data is considered to be paired or dependent. If the data is obtained from different subjects and the results of two or more groups are compared (*e.g.* comparing blood pressure values of subjects who were given a drug to the blood pressure values of subjects in the control group), the data is considered to be unpaired or independent.
4. **Assumptions:** Assumptions in statistics play an important role in choosing appropriate tests. When assumptions are violated, the power of that test decreases as a result of type I and type II errors, consequently leading to either overestimation or underestimation of the results. The following are few of the commonly used assumptions in research studies

i. Assumption of normality: Data that is normally distributed shows symmetry around the centre and follows a bell-shaped curve. The Central Limit Theorem states that, as the sample size gets larger, the sample mean tends to approach normal distribution. Normality can be tested using skewness and kurtosis, where the values should range within ±2 and ±7, respectively, or Shapiro-Wilk test or Kolmogorov-Smirnov test where the *p* value should be greater than 0.05 to satisfy this assumption.

ii. Assumption of homogeneity of variance: This assumption assesses if the two groups of variables have equal variances. To satisfy this assumption, Levene's test could be used where a *p* value greater than 0.05 indicates equality in variances.

iii. Assumption of linearity: This assumption assesses if the two variables have a straight-line relationship. Usually when assumptions of normality and homogeneity of variances are met, the assumption of linearity is automatically taken care of.

2.8.2 Statistical tests used in this study

All statistical analyses were performed using IBM SPSS software (version 25.0; Armonk, NY, USA: IBM Corp). The baseline characteristics/study demographics are summarized as mean (with standard deviation [SD]), or median (with interquartile range). The sample size used for this entire study, including analysis of both frozen and paraffin samples, was n = 28.

In the case where we were investigating the correlation between stroke etiology and thrombus composition **(Fig. 3-2)**, we used a parametric test because the data showed nothing against normality (Shapiro-Wilk's test: $p > 0.05$). Statistical differences between the means were

compared using 2-tailed independent samples *t*-test. This was an appropriate test as the independent variable, stroke etiology, was categorical (nominal) while the dependent variable, thrombus composition, was measured on a continuous scale.

In the case where we were investigating correlations between stroke severity and thrombus composition **(Fig 3-3)**, we used binary logistic regression to compare means across the two groups as the independent variable, thrombus composition, was measured on a continuous scale while the dependent variable, NIHSS score, was dichotomous and measured on an ordinal level. On the other hand, the 2-tailed independent samples *t*-test was used to determine statistical differences within each of the NIHSS groups independently which were normally distributed. In addition, for investigating correlations between stroke severity and occlusion location, where the independent variable, occlusion location, and the dependent variable, NIHSS score, were both categorical, we used Fisher's exact test, the non-parametric counterpart of the Chi-Square test.

In the case, where we were investigating variables that were correlating the effects of thrombus composition on EVT device and recanalization success **(Fig. 3-4 A–B)**, we used binary logistic regression, as the independent variable, thrombus composition, was measured on a continuous scale while the dependent variables, EVT devices and TICI scores, were measured on a nominal and ordinal level, respectively. However, to compare means within groups independently, which were normally distributed, we used 2-tailed independent samples *t*-test. In addition, for investigating correlations between EVT device and recanalization success **(Fig. 3-4C)**, where the independent variable, EVT device, and the dependent variable, TICI score, were both categorical, we used Fisher's exact test.

In the case where we were investigating the effects of thrombus composition on 90-day mRS and NIHSS **(Fig. 3-5A–B)**, we used 2-tailed independent samples *t*-test to compare means within

each individual group, since the data was normally distributed. We used ordinal regression to express correlations between EVT device, TICI scores and mRS scores **(Fig. 3-5 C, E)** and determine whether recanalization status obtained or devices chosen during thrombectomy had an effect on the functional outcome. Because the dependent variable, mRS scores, had three categories, ordinal regression was an appropriate test. On the other hand, we used Chi-Square test to express correlations between TICI scores, effects of longer procedural time and attempts with mRS scores **(table 3-3 and Fig 3-6 A, B)**.

In the case of expressing the effects of thrombus composition on elemental composition **(Fig 3-7)**, we used non-parametric Mann-Whitney U-test, where the independent variable, thrombus type, was categorical (nominal) while the dependent variable, elemental composition, was measured on a continuous scale.

In the case where we were investigating the effects of stroke etiology on elemental and organic biochemical composition **(Fig 3-13 A-C)**, we used the Mann-Whitney U-test, a non-parametric version of independent samples *t*-test, as the data was not normally distributed and the dependent variables, elemental and biochemical composition, were measured on a continuous scale while the independent variable, etiology, was measured on a nominal categorical level.

Binary logistic regression was used in the case where we were expressing the effects of elemental composition and organic biochemical composition on recanalization success **(Fig. 3-14 A and Fig. 3-15 A-C)**. The 2-tailed independent samples *t*-test was used to compare means between elemental composition and mRS scores **(Fig. 3-14 B)** (data showed normality), and ordinal regression was used to compare means between organic biochemical composition and mRS scores **(Fig. 3-15 D-F)**.

The Mann-Whitney U-test was used for measuring thrombus perviousness and stroke etiology **(Fig. 3-16 B)**. Lastly, the correlation between thrombus perviousness and recanalization outcome was tested using binary logistic regression **(Fig. 3-16C)**.

Chapter Three: Results

3.1 Patient demographics

Twenty-eight patients were included in the analysis (13 men and 15 women; mean age ± standard deviation, 71.2 ± 15.4 years). The patient and treatment characteristics including their ASPECTS, pre-treatment NIHSS, 90-day NIHSS and 90-day mRS are summarized in table 3-1. 39.2% (11/28) of the patients had left middle cerebral artery (MCA) occlusion, 50% (14/28) of the patients had right MCA occlusions, and 10.7% (3/28) of the patients had basilar artery occlusions. 25% (7/28) of the patients had a smoking history, either previous or current. 14.3% (4/28) of the patients received intravenous tissue plasminogen activator (tPA) before thrombectomy, and 35.7% (10/28) of the patients received anti-platelet drugs post-thrombectomy. 71% (20/28) of the patients were treated with stentrievers, which included either stenting alone or the Solumbra technique, while 29% (8/28) of the patients were treated with aspiration alone (ADAPT technique). 7.1% (2/28) of the patients had a TICI score of 1-2a, and 92.9% (26/28) patients had a TICI score of 2b-3. **(Table 3-1)**.

Table 3-1: Patient Demographics. Summary of the study population and demographics collected from September 2017 until January 2019.

	Total
Sample size	n = 28
Mean Age (years ± SD)	71.2 ± 15.4 years
Sex	
Males	13
Females	15
Active Smoking Status	7
Stroke Etiology	
Cardioembolic	17
Arterial	11
Occlusion location	
Left MCA/ICA	11
Right MCA/ICA	14
Basilar	3
Intervention Drugs	
Intravenous tPA (thrombolytic)	4
Reopro (anti-platelets)	8
Plavix (anti-platelet)	2
TICI	
0 – no reperfusion	0
1-2a – incomplete reperfusion	2
2b-3 – near-to-complete reperfusion	26
90 day mRS	
mRS 0-2 No symptoms-minor disabilities	15
mRS 3-5 moderate-severe disabilities	4
mRS 6 Dead	9
Thrombectomy Devices	
Stentriever	20
ADAPT	8
Pre-Treatment NIHSS*	Median 17, IQR 7.5 (19-11.5)
90-day NIHSS	Median 0.5 , IQR 10 (10-0)
ASPECTS	Median 8, IQR 3 (10-7)

SD = standard deviation, MCA = Middle Cerebral Artery, ICA = Internal Carotid Artery, tPA = tissue plasminogen activator, NIHSS = National Institute of Health Stroke Scale, IQR = interquartile range, TICI = Thrombolysis In Cerebral Infarction, ASPECTS = Alberta Stroke Program Early Computer Tomography Score, mRS = Modified Rankin Scale.

*3 of 28 participants (pt 22, pt 26, and pt 28) were not accounted for in the median and IQR counts of NIHSS as their pre-treatment NIHSS scores were not collected. NIHSS and ASPECTS, are presented using their respective median values and interquartile range (IQR) [162]

3.2 Histology results

3.2.1 Quantifying percent composition of erythrocytes and fibrin in thrombi

As mentioned in the Methods section, each thrombus sample was cut in half where half of the sample was formalin-fixed while the other half was flash frozen. Four of the 28 formalin-fixed samples were misplaced during sample transportation to the laboratory and therefore were eliminated from all histological analysis including ImageJ classification of red and white thrombus proportions. However, the other halves of these 4 samples that were flash frozen were still processed and analyzed using synchrotron and IR imaging modalities. Thus, for histological analysis only 24 of the 28 thrombi were stained with Masson's trichrome to visualize the distribution of erythrocytes and fibrin, and thereby quantitatively classify these thrombi as either red or white. Even though previous studies have histologically characterized thrombi and confirmed the presence of inflammatory mediators, platelets, macrophages, white blood cells, RBCs, and endothelial cells [85], [87], [163], it was still important for us to confirm the presence of these components, to visualize the distribution of different cells simultaneously on adjacent sections, and to validate the classification of thrombi using a standardized software technique. Table 3-2 contains the raw data obtained by quantifying regions of erythrocytes and fibrin on the Masson's trichrome stained images. 62.5% (15/24) thrombi were identified as red thrombi. Additionally, retrospective analysis of thrombi revealed that the 4 patients that received IV-tPA had thrombi classified as red thrombi (*i.e.* %RBCs > % fibrin).

Table 3-2: Raw data representing quantification of erythrocytes and fibrin. Data shows quantitative characterization of thrombi as red or white based on percent composition of erythrocytes and fibrin obtained by measuring red and blue areas on the Masson's trichrome sections using trainable WEKA segmentation plugin in ImageJ software. White thrombi define fibrin-rich clots while red thrombi define erythrocyte-rich clots.

Thrombus ID	Region highlighted	Count	Particle Area	Particle Avg Size	%Area	% composition	Type of thrombus
015 s1	RBC-rich area	525	23615	44.981	1.922	23615/131640 **=17.94%**	white
	Fibrin-rich area	624	108025	173.117	8.791	108025/131640 82.06%	
	Total Area s1		23615+ 108025 **=131640**				
015 s2	RBC-rich area	958	35860	37.432	2.918	20.67%	white
	Fibrin-rich area	723	137654	190.393	11.202	79.33%	
	Total Area s2		173514				
s1 + s2	RBC-rich area		59475			19.49%	white thrombus
	Fibrin-rich area		245679			80.51%	
	Total Area		305154				
016 s1	RBC-rich area	215	45116	209.842	3.672	70.88%	red
	Fibrin-rich area	1044	18536	17.755	1.508	29.12%	
	Total Area s1		63652				
016 s2	RBC-rich area	531	51679	97.324	4.206	51.28%	red
	Fibrin-rich area	1022	49093	48.036	3.995	48.72%	
	Total Area s2		100772				
016 s3	RBC-rich area	656	302107	460.529	24.586	84.39%	red
	Fibrin-rich area	2191	55879	25.504	4.547	15.61%	
	Total Area s3		357986				
s1 + s2 + s3	RBC-rich area		398902			76.36%	red thrombus

	Fibrin-rich area		123508			23.64%	
	Total Area		522410				
017 s1	RBC-rich area	223	29176	130.834	2.374	47.49%	white
	Fibrin-rich area	396	32259	81.462	2.625	52.51%	
	Total Area s1		61435				
017 s2	RBC-rich area	362	42440	117.238	3.454	59.28%	red
	Fibrin-rich area	1125	29156	25.916	2.373	40.72%	
	Total Area s2		71596				
s1 + s2	RBC-rich area		71616			53.83%	red thrombus
	Fibrin-rich area		61415			46.17%	
	Total Area		133031				
019	RBC-rich area	248	79898	322.169	6.502	60.61%	red thrombus
	Fibrin-rich area	154	51916	337.117	4.225	39.39%	
	Total Area		131814				
020 s1	RBC-rich area	1739	234368	134.772	19.073	64.13%	red
	Fibrin-rich area	3504	131078	37.408	10.667	35.87%	
	Total Area s1		365446				
020 s2	RBC-rich area	856	131355	153.452	10.69	60.23%	red
	Fibrin-rich area	2845	86726	30.484	7.058	39.77%	
	Total Area s2		218081				
020 s3	RBC-rich area	200	19196	95.98	1.562	47.67%	white
	Fibrin-rich area	559	21072	37.696	1.715	52.33%	
	Total Area s3		40268				
s1 + s2 + s3	RBC-rich area		384919			61.71%	red thrombus
	Fibrin-rich area		238876			38.29%	
	Total Area		623795				
021 s1	RB- rich area	401	330474	824.125	26.894	85.74%	red
	Fibrin-rich area	935	54941	58.76	4.471	14.26%	
	Total Area s1		385415				

021 s2	RBC-rich area	114	155821	1366.851	12.681	69.80%	red
	Fibrin-rich area	636	67431	106.024	5.488	30.20%	
	Total Area s2		223252				
s1 + s2	RBC-rich area		486295			79.90%	red thrombus
	Fibrin-rich area		122372			20.10%	
	Total Area		608667				
023 s1	RBC-rich area	922	142666	154.735	11.61	53.57%	red
	Fibrin-rich area	2201	123639	56.174	10.062	46.43%	
	Total Area s1		266305				
023 s2	RBC-rich area	1282	150516	117.407	12.249	43.26%	white
	Fibrin-rich area	1178	197400	167.572	16.064	56.74%	
	Total Area s2		347916				
s1 + s2	RBC-rich area		293182			47.73%	white thrombus
	Fibrin-rich area		321039			52.27%	
	Total Area		614221				
*024_1	RBC-rich area	1024	59805	58.403	4.867	26.69%	white thrombus
	Fibrin-rich area	644	164297	255.12	13.371	73.31%	
	Total Area		224102				
*024_2	RBC rich area	1845	341515	185.103	27.793	71.93%	red thrombus
	Fibrinous area	3326	133278	40.072	10.846	28.07%	
	Total Area		474793				
025	RBC-rich area	863	193798	224.563	15.771	65.31%	red thrombus
	Fibrin-rich area	2002	102920	51.409	8.376	34.69%	
	Total area		296718				
026	RBC-rich area	516	125422	243.066	10.207	73.57%	red thrombus
	Fibrin-rich area	1313	45056	34.315	3.667	26.43%	
	Total area		170478				
027 s1	RBC-rich area	337	32071	95.166	2.61	19.44%	white

	Fibrin-rich area	475	132881	279.749	10.814	80.56%	
	Total area s1		164952				
027 s2	RBC-rich area	993	114066	114.87	9.283	39.13%	white
	Fibrin-rich area	2006	177471	88.47	14.443	60.87%	
	Total area s2		291537				
027 s3	RBC-rich area	827	205680	248.706	16.738	59.47%	red
	Fibrin-rich area	1339	140163	104.677	11.406	40.53%	
	Total area s3		345843				
s1 + s2 + s3	RBC-rich area		351817			43.85%	white thrombus
	Fibrin-rich area		450515			56.15%	
	Total area		802332				
028 s1	RBC-rich area	1255	185042	147.444	15.059	64.79%	red
	Fibrin-rich area	4028	100542	24.961	8.182	35.21%	
	Total area s1		285584				
028 s2	RBC-rich area	1027	39951	38.901	3.251	33.88%	white
	Fibrin-rich area	1144	77967	68.153	6.345	66.12%	
	Total area s2		117918				
028 s3	RBC-rich area	2945	82575	28.039	6.72	34.83%	white
	Fibrin-rich area	2799	154499	55.198	12.573	65.17%	
	Total area s3		237074				
028 s4	RBC-rich area	423	179743	424.924	14.628	87.82%	red
	Fibrin-rich area	2893	24925	8.616	2.028	12.18%	
	Total area s4		204668				
s1 + s2 + s3 + s4	RBC-rich area		487311			57.65%	red thrombus
	Fibrin-rich area		357933			42.35%	
	Total area		845244				
029	RBC-rich area	593	145759	245.799	11.862	70.41%	red thrombus
	Fibrin-rich area	2778	61246	22.047	4.984	29.59%	
	Total area		207005				

030	RBC-rich area	1267	212592	167.792	17.301	71.79%	red thrombus
	Fibrin-rich area	1605	83549	52.055	6.799	28.21%	
	Total area		296141				
031 s1	RBC-rich area	843	285344	338.486	23.221	77.84%	red
	Fibrin-rich area	3179	81213	25.547	6.609	22.16%	
	Total area s1		366557				
031 s2	RBC-rich area	107	65907	615.953	5.364	92.03%	red
	Fibrin-rich area	958	5706	5.956	0.464	7.97%	
	Total area s2		71613				
031 s3	RBC-rich area	1235	86429	69.983	7.034	63.12%	red
	Fibrin-rich area	1728	50491	29.219	4.109	36.88%	
	Total area s3		136920				
s1 + s2 + s3	RBC rich area		437680			76.11%	red thrombus
	Fibrinous area		137410			23.89%	
	Total area		575090				
034	RBC-rich area	588	55687	94.706	4.532	60.42%	red thrombus
	Fibrin-rich area	1217	36477	29.973	2.969	39.58%	
	Total area		92164				
037 s1	RBC-rich area	1041	62242	59.791	5.065	50.35%	red
	Fibrin-rich area	1416	61369	43.34	4.994	49.65%	
	Total area s1		123611				
037 s2	RBC-rich area	565	91225	161.46	7.424	47.14%	white
	Fibrin-rich area	1697	102289	60.276	8.324	52.86%	
	Total area s2		193514				
037 s3	RBC-rich area	663	37569	56.665	3.057	39.29%	white
	Fibrin-rich area	1549	58054	37.478	4.724	60.71%	
	Total area s3		95623				
s1 + s2 + s3	RBC-rich area		191036			46.28%	white thrombus

	Fibrin-rich area		221712			53.72%	
	Total area		412748				
038	RBC-rich area	767	376835	491.31	30.667	79.35%	red thrombus
	Fibrin-rich area	1366	98081	71.802	7.982	20.65%	
	Total area		474916				
039	RBC-rich area	1098	102847	93.668	8.37	60.15%	red thrombus
	Fibrin-rich area	2931	68126	23.243	5.544	39.85%	
	Total area		170973				
040	RBC-rich area	768	61043	79.483	4.968	43.23%	white thrombus
	Fibrin-rich area	981	80176	81.729	6.525	56.77%	
	Total area		141219				
044 s1	RBC-rich area	1387	191939	138.384	15.62	42.21%	white
	Fibrin-rich area	1497	262741	175.512	21.382	57.79%	
	Total area s1		454680				
044 s2	RBC-rich area	985	224353	227.77	18.258	47.66%	white
	Fibrin-rich area	963	246382	255.848	20.051	52.34%	
	Total area s2		470735				
s1 + s2	RBC-rich area		416292			44.98%	white thrombus
	Fibrin-rich area		509123			55.02%	
	Total area		925415				
045 s1	RBC-rich area	179	240944	1346.056	19.608	54.82%	red
	Fibrin-rich area	1349	198561	147.191	16.159	45.18%	
	Total area s1		439505				
045 s2	RBC-rich area	190	74682	393.063	6.078	33.29%	white
	Fibrin-rich area	269	149679	556.428	12.181	66.71%	
	Total area s2		224361				
s1 + s2	RBC-rich area		315626			47.54%	white thrombus
	Fibrin-rich area		348240			52.46%	

	Total area		663866				
046 s1	RBC-rich area	538	90046	167.372	7.328	27.47%	white
	Fibrin-rich area	984	237789	241.655	19.351	72.53%	
	Total area s1		327835				
046 s2	RBC-rich area	466	48585	104.26	6.39	22.06%	white
	Fibrin-rich area	564	171609	304.271	22.571	77.94%	
	Total area s2		220194				
Average	RBC-rich area		138631			25.30%	white thrombus
	Fibrin-rich area		409398			74.70%	
	Total area		548029				

*Pt 24 had two strokes on the same day. s1 = section 1, s2 = section 2, s3 = section 3

3.2.2 Distribution of erythrocytes, fibrin, platelets, endothelial cells, and macrophages

While histological examination is important to identify cellular characteristics and components that make up thrombus integrity, it is also important to identify their gross morphology. The top panel in figure 3-1 showed representative cases of dark red and pinkish thrombi along with their characteristic texture wherein, the thrombi either had a jelly-like elastic texture or a dry rigid texture **(Fig. 3-1 top panel)**. Difference in the appearance of colour was potentially due to factors such as: amount of atmospheric exposure (oxidation), hemolysis, and erythrocyte:fibrin ratio. We did not perform any further analysis on thrombus texture, and we did not correlate the gross morphology of the thrombus to its histological composition. The gross morphology and texture of thrombi were briefly mentioned as a mean to show the different types of thrombi retrieved.

All histological stains and immunohistochemistry for 24 samples were performed on adjacent sections for comparative analysis. Hematoxylin and Eosin was the routine principle stain performed on the samples to identify the presence of different cells **(Fig. 3-1 A-D).** H&E showed

extensive distribution and infiltration by neutrophils **(D)** throughout the thrombi, thereby indicating acute inflammation. Qualitative assessment indicated higher neutrophil distribution in fibrin-rich areas than erythrocyte-rich areas. Some thrombi also showed the presence of eosinophils **(C).** Masson's trichrome stained fibrin in blue and erythrocytes in red. Some thrombi had organized layers of fibrin with erythrocytes trapped in between **(Fig. 3-1 F).** Traditionally thrombi with alternating layers of fibrin and erythrocytes were characterized as "layered" while thrombi that appeared with patterns of fibrin:platelet bands interspersed with deposits of polymorphonulcear cells and erythrocytes were characterized as "serpentine". Some thrombi had densely packed erythrocytes in the core, with fibrin strands densely organized in the periphery **(Fig. 3-1 E)** while some thrombi had loosely organized fibrin. CD68 stained positive for macrophages **(Fig. 3-1 G-H)**, showing macrophage infiltration with no specific distribution patterns. However, aggregates of brown granular amorphous debris were frequently observed in fibrin rich areas. Factor VIII/vwF were used for immunolabelling platelets **(Fig. 3-1 I, J)** while CD31 was used as a marker for endothelial cells **(Fig. 3-1 K, L)**. Both platelets and endothelial cells co-localized in fibrin-rich areas. In addition, aggregates of platelets and endothelial cells appeared to form patterns of sinuous bands along fibrin rich regions **(Fig. 3-1 J, L)**. There were no cholesterol crystals, lipid component calcifications, intramural hemorrhage, and sheared intima of the vessel wall or smooth muscle cells observed in any of the thrombus samples.

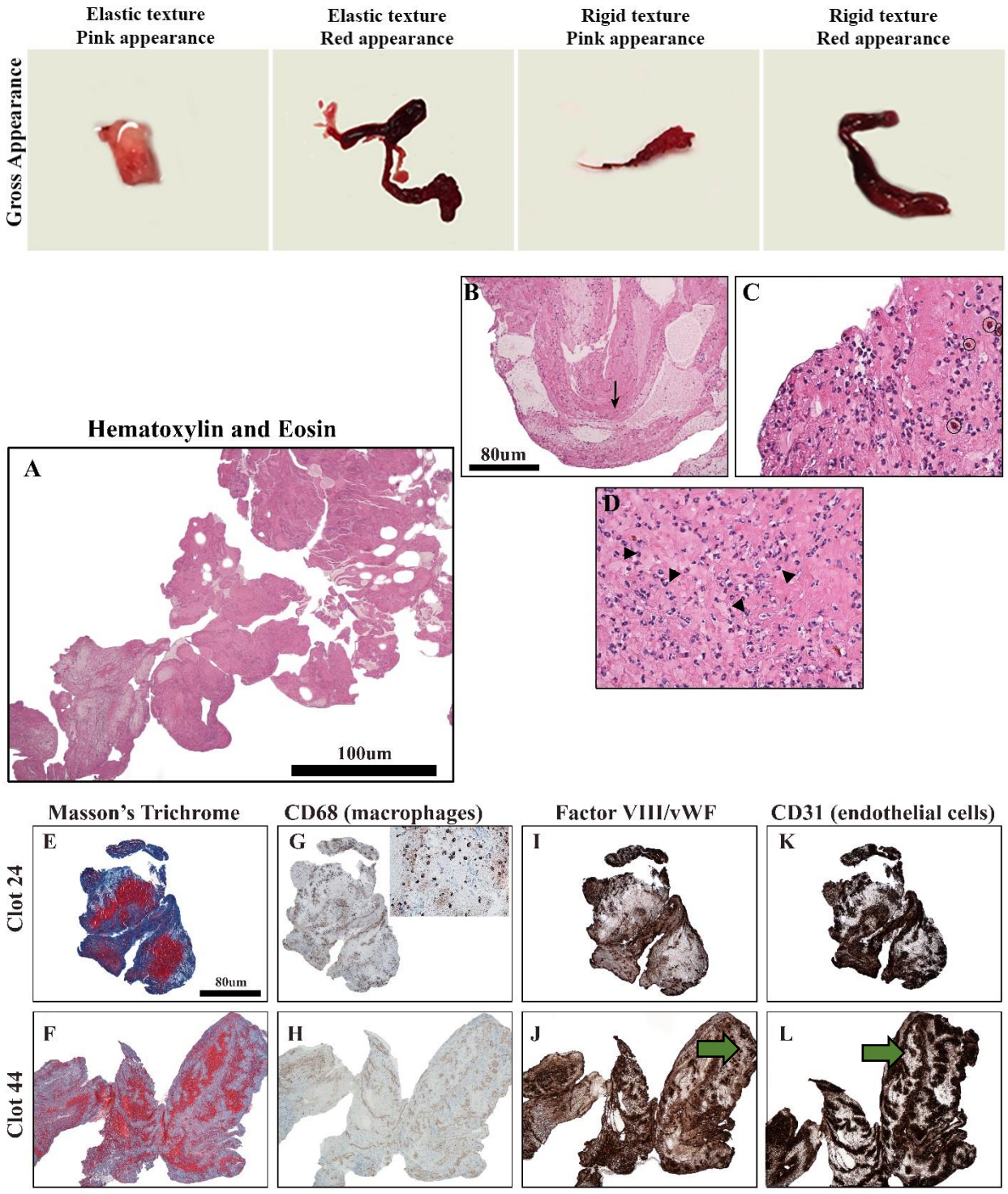

Figure 3-1: Histological examination of thrombi. The above panel represents a macroscopic view of the gross appearance and texture (1-4). 5µm thick, 10% formalin fixed paraffin embedded sections stained with Hematoxylin and Eosin (A-D) show organized fibrin layers indicated in black arrow (B), eosinophils (C), and neutrophils indicated in black arrowheads (D), Masson's trichrome show fibrin (stained blue) and RBCs (stained red) organized in layers (E-F),

anti-CD68 show macrophages (G-H) with a high magnification insert showing amorphous granular debris, Factor VIII/von Willebrand factor (vWF) show platelets (I-J), and anti-CD31 show endothelial cells (K-L) distributed and forming sinuous bands in fibrinous areas (green arrows). Images were acquired using the Nikon microscope. Scale bars: 100 μm (A), 80 μm (C-L).

3.3 Correlations between clinical variables and thrombus composition

3.3.1 Assessing the effects of stroke etiology on thrombus composition

To validate whether biological composition was altered in thrombi originating from the proximal arteries (artery-to-artery embolism) as opposed to the heart (cardioembolism), we correlated source of origin with the proportions of erythrocytes and fibrin, derived from ImageJ analysis. Since, the classification of an entire thrombus as red or white was not reliable based on just section analysis, we chose to represent the data using the mean percentage of erythrocytes and fibrin instead of correlating the etiology with the number of red/white thrombi. The data was normally distributed (Shapiro–Wilk test - % RBC: $p = 0.56$ *versus* % Fibrin: $p = 0.13$). Comparing proportion of erythrocytes and fibrin within each etiologic group independently, our results showed that thrombi in patients with cardioembolism had a significantly higher proportion of erythrocytes and a lower proportion of fibrin (59.03% ± SEM 4.59 *versus* 40.97% ± SEM 4.59; $p = 0.009$). Similarly, thrombi in patients with artery-to-artery embolism showed a higher proportion of erythrocytes and lower proportion of fibrin (53.02% ± SEM 5.68 *versus* 46.80% ± SEM 4.68; $p = 0.436$), however, the differences were not statistically significant in this group. In addition, cross-comparing proportions of erythrocytes and fibrin across the two etiologic groups, our findings showed higher proportion of erythrocytes in cardioemboli than artery-to-artery emboli (59.03% *versus* 53.20%), and higher proportion of fibrin in artery-to-artery emboli than cardioemboli (46.80% *versus* 40.97%), however, these differences were not statistically significant ($p = 0.437$) **(Fig. 3-2)**.

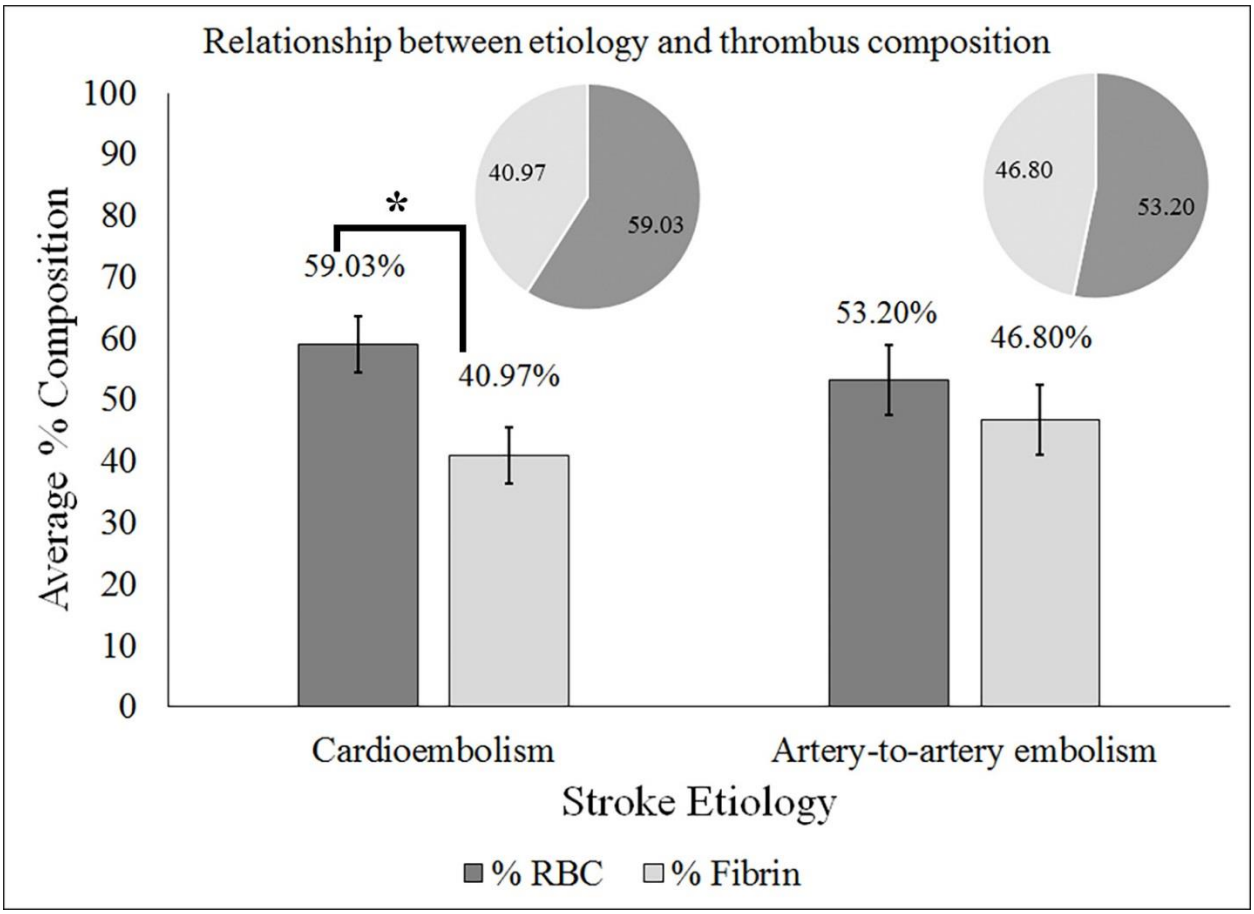

Figure 3-2: Correlation between stroke etiology and thrombus composition. Bar graph compares proportion of erythrocytes and fibrin present in thrombi arising from cardioembolism (heart) and artery-to-artery embolism (large artery). Pie graphs are included as an alternative representation to indicate that the proportions of erythrocytes and fibrin are complimentary percentages. RBC = red blood cells (erythrocytes). (*) *p = 0.009*

3.3.2 Accessing the effects of thrombus composition and occlusion location on stroke severity

Stroke severity was assessed using the NIHSS scores. Of the 28 patients who were scored on a range of 0-42 prior to thrombectomy (at admission), thrombi retrieved from 6 patients were excluded from further analysis as pre-admission NIHSS were not scored for 3 patients (#22, #26, and #28), and formalin-fixed samples of 4 patients were misplaced during transportation (#18, #22, #33, and #42), as mentioned previously. The NIH scores of 22 patients were recorded in one of the two groups; NIHSS ≤ 10 or NIHSS > 10, where 10 was used as a baseline score because it

differentiated a minor stroke from a moderate-to-severe stroke [142]. The data showed nothing against normality (Shapiro–Wilk test - NIHSS ≤ 10: $p = 0.754$ *versus* NIHSS > 10: $p = 0.278$). Comparing the percentages of erythrocytes and fibrin within each NIHSS groups, independently, our findings suggested that patients who suffered a minor stroke (NIHSS ≤ 10) had a significantly higher proportion of erythrocytes and lower proportions of fibrin (65.37% *versus* 34.63% ± SEM 4.53%, $p = 0.0014$) while patients that suffered a moderate to severe stroke (NIHSS > 10) had thrombi that statistically showed no difference in erythrocyte and fibrin percentages (53.30% *versus* 46.70% ± SEM 4.56%, $p = 0.3$). However, when we compared the percentages of erythrocytes and fibrin across the two NIHSS groups, patients who suffered a minor stroke (NIHSS ≤ 10) had higher proportions of erythrocytes (65.37% *versus* 53.30%) while patients who suffered a major stroke (NIHSS > 10) had higher proportions of fibrin (46.70% *versus* 34.63%) but the differences across the groups were insignificant ($p = 0.19$) **(Fig. 3-3)**.

Patients with occlusions in their left MCA usually show more severe stroke symptoms than patients with occlusions in their right MCA due to aphasia. Our findings however, showed that both right MCA occlusions and left MCA occlusions resulted in volumetrically equal underlying infarcts (right 15.8 ± 3.3 *versus* left 14.5 ± 7.4, $p = 0.61$).

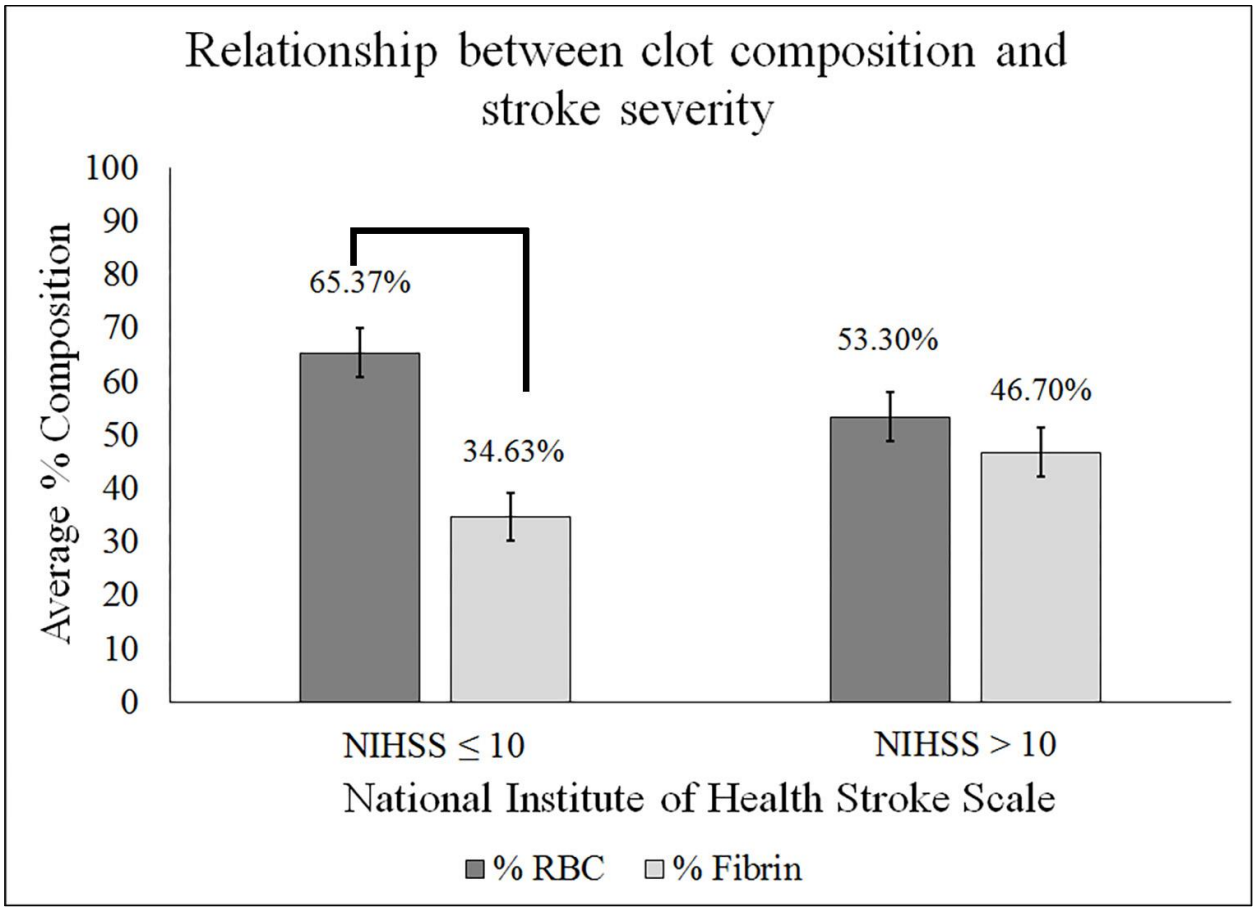

Figure 3-3: Correlation between stroke severity and thrombus composition. Bar graph compares proportion of erythrocytes and fibrin (%) in thrombi of patients that presented with either a minor stroke (NIHSS ≤ 10) or a severe stroke (NIHSS > 10), to determine whether thrombus composition affects stroke severity. The NIHSS scores were collected at admission prior to thrombectomy. The data does not include NIH scores for 3 patients who suffered a basilar stroke as the scores were not recorded at admission. NIHSS = the National Institute of Health Stroke Scale, RBC = red blood cells. The values represented above the error bars in graph are the mean percentages of thrombus composition.

3.3.3 Thrombus composition does not affect the choice of thrombectomy device used for achieving full recanalization.

Since, the goal of EVT is to achieve higher rates of complete recanalization and improve long-term health outcomes, it is important to determine if recanalization success and long-term outcomes are dependent on factors such as; thrombus composition or the choice of EVT device. The data was normally distributed (Shapiro–Wilk's test – ADAPT: $p = 0.617$ *versus* Stentriever: $p = 0.187$). Our findings suggested that thrombi retrieved by ADAPT had lower proportions of erythrocytes (55.81% ± SEM 6.49% *versus* 57.36% ± SEM 4.35%) and higher proportions of fibrin (44.19% *versus* 42.64%) than thrombi retrieved by stentrievers. However, the differences across the two groups were not statistically significant ($p = 0.833$). In the overall comparison between the two groups (ADAPT, Stentrievers), all samples indicated a higher percent of erythrocytes regardless of their retrieval device, suggesting that the choice of thrombectomy device used for retrieving the thrombus successfully did not correlate with the thrombus composition **(Fig. 3-4A)** and regardless whether a thrombus was composed of high erythrocytes or fibrin, it was equally well retrieved using either of the two techniques.

When expressing a correlation between thrombus composition and recanalization success, the data was normally distributed (Shapiro–Wilk test- TICI 1-2a *versus* TICI 2b-3: $p = 0.09$). Patients in whom incomplete recanalization (TICI 1-2a, n = 2) was achieved, had thrombi composed of higher proportion of fibrin and lower proportion of erythrocytes compared to thrombi of patients in whom near-to-complete recanalization (TICI 2b-3, n = 26) was obtained (fibrin: 48.31% *vs* 42.69%, erythrocytes: 51.69% *vs* 57.31% , $p = 0.67$). However, just analyzing thrombi from the TICI 2b-3 group, revealed that these thrombi were composed of significantly higher proportion of erythrocytes and lower proportion of fibrin (57.37% *vs* 42.69% ± SEM 3.81

%, *p = 0.01*). However, because the results were insignificant across the two TICI groups (*p = 0.657*), the data suggested no correlation between thrombus composition and recanalization outcomes **(Fig 3-4B)**. Additionally, it is important to keep in mind that, since TICI 1-2a had a small size (n = 2) the comparisons between the two groups were less powered.

TICI scores were also compared within the two groups of thrombectomy devices to assess whether the choice of thrombectomy device used for opening the occluded vessel influenced recanalization status. In the number of thrombectomy cases where near-to-complete recanalization was obtained (TICI 2b-3), *n = 14* were successfully treated with stentrievers while *n = 8* were successfully treated with ADAPT. Likewise, in the number of thrombectomy cases where minimal to incomplete recanalization was obtained (TICI 1-2a), *n =2* were successfully treated with stentrievers while we had no patients in this group that were treated with ADAPT. There was no significant correlation between EVT device and TICI scores (*p = 0.536*), suggesting that recanalization status was not dependent on the choice of thrombectomy device used for thrombus retrieval. These results would have to be validated using a larger sample size **(Fig. 3-4C)**.

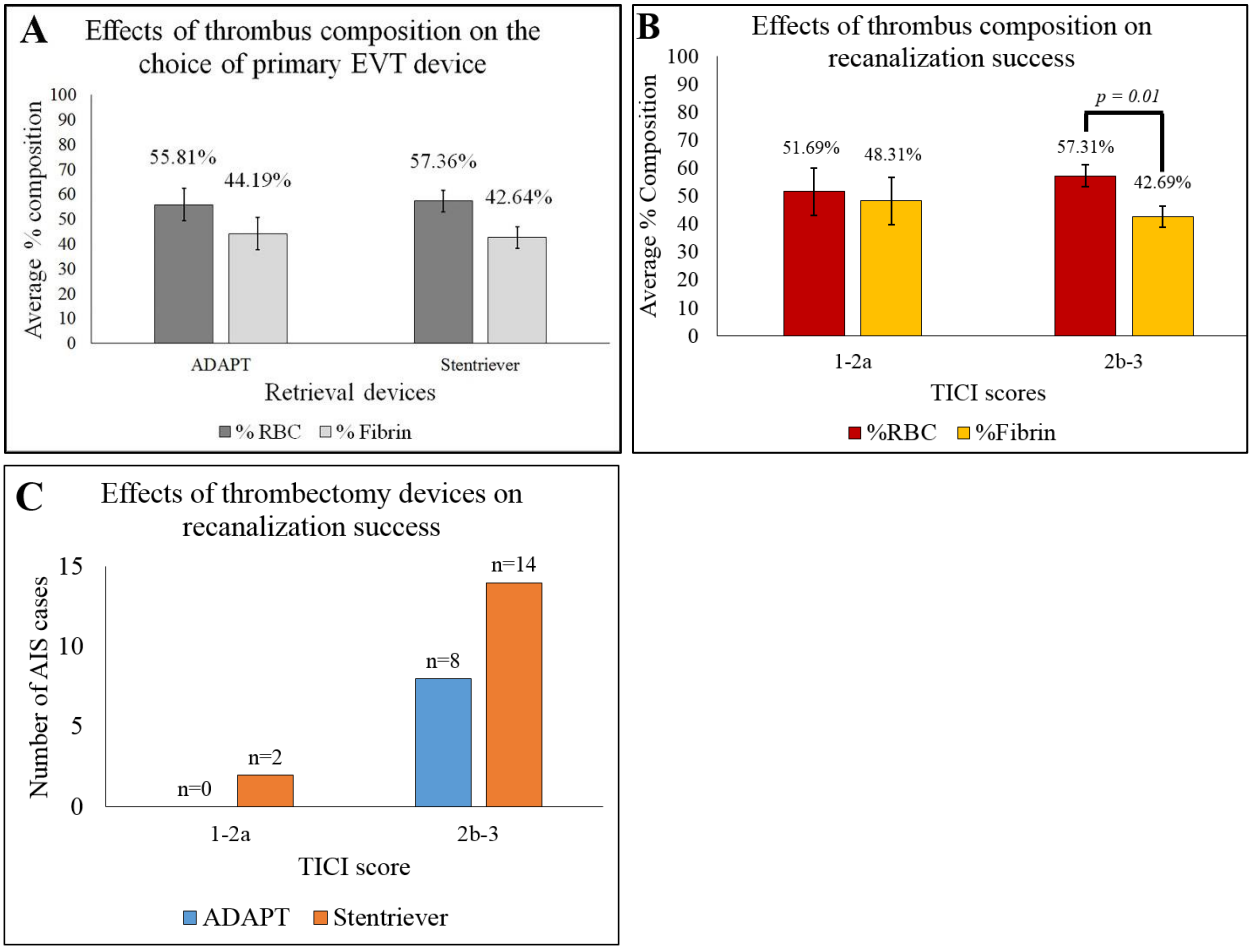

Figure 3-4: Correlation between thrombus composition, EVT device choice and recanalization success. Bar graphs shows comparisons between (A) thrombus composition and retrieval device, (B) thrombus composition and TICI scores to determine whether histological composition affects recanalization outcomes (C) TICI scores and retrieval device to determine whether the choice of devices (ADAPT or Stentrievers) affect recanalization outcomes (C). ADAPT = A Direct Aspiration First Pass Technique, TICI = Thrombolysis in Cerebral Infarction where 1-2a defines incomplete recanalization and a score of 2b-3 defines near-to-complete recanalization, AIS = Acute Ischemic Stroke, RBC= red blood cells. The values represented above the error bars in graph A and B are the mean percentages of thrombus composition.

3.3.4 Assessing the effects of thrombus composition, thrombectomy devices and recanalization status on 3-month functional outcomes

Studies have shown that the first 3-months after suffering a stroke are crucial, where the risks of poor health outcomes are higher and directly related to the stroke. In that context, we used three variables; histological composition, primary retrieval device that successfully retrieved the thrombus, and recanalization status to investigate if these factors influenced the prognosis of 3-month functional outcomes. Three-month functional outcomes were evaluated by mRS and NIHSS scores which were assigned by a neurologist during the "standard of care" 90-day visit.

Data analyzing the effects of thrombus composition on 90-day mRS (n = 24), was normally distributed (Shapiro–Wilk test- mRS 0-2: $p = 0.077$ *vs* mRS 3-5: $p = 0.875$ *vs* mRS 6: $p = 0.247$). Patients with thrombi composed of significantly higher proportions of erythrocytes and lower proportions of fibrin had moderate to severe disabilities (mRS 3-5: 65.75% *vs* 34.25% ± SEM 3.37%, $p = 0.003$); while patients who suffered minor disabilities also had thrombi with higher erythrocytes than fibrin, however the differences in composition were insignificant (mRS 0-2: 56.84% *vs* 43.16% ± SEM 5.5%, $p = 0.09$). This trend was also true for patients who died within 90-days as their thrombi had higher erythrocytes than fibrin, but the differences were statistically insignificant as well (mRS=6: 51.02% *vs* 46.98% ± SEM 4.92%, $p = 0.4$). Overall, the findings across all three groups suggested that the thrombi composition did not affect mRS outcomes ($p = 0.892$) (**Fig. 3-5A)**.

In addition, data analyzing the effects of thrombus composition on 90-day NIHSS (n = 16; 4 samples misplaced, 7 patients died within 90 days, and 1 patient was not scored), our results also showed that patients with severe NIH outcomes (NIHSS > 10), had thrombi composed of significantly higher percentage of erythrocytes and lower percentage of fibrin (68.55% *vs*

31.45% ± SEM 3.24%, *p = 0.01*) than thrombi of patients who suffered minor to no disabilities (NIHSS ≤ 10), where percentages of erythrocytes and fibrin were insignificantly different (57.74% *vs* 42.26% ± SEM 5.66%, *p = 0.06*). However, comparing proportions of erythrocytes and fibrin across the two groups, showed no significant differences (*p = 0.512*) **(Fig 3-5B).**

Data evaluating the effects of EVT devices on 90-day mRS, showed no differences across any of the groups (*p = 0.363*), mRS 0-2 (minor disabilities): ADAPT *n = 6 vs* Stentrievers *n = 8*, mRS 3-5 (moderate to severe disabilities): ADAPT *n = 1 vs* Stentrievers *n = 2*, and mRS=6 (dead): ADAPT *n = 1 vs* Stentrievers *n = 6*. Similarly, evaluating the effects of EVT device on 90-day NIHSS, showed no differences across both the groups (*p = 0.869*), NIHSS ≤ 10 (minor impairments): ADAPT *n = 5 vs* Stentrievers *n = 9*, and NIHSS > 10 (moderate impairments): ADAPT *n = 1 vs* Stentrievers *n = 1*. Thus, the results suggested that retrieval devices did not affect the degree of disability dependence **(Fig. 3-5C, D)**. Moreover, we also evaluated the correlation between TICI and mRS scores. Majority of the patients in whom near-to-complete recanalization was achieved (15 of the 26 patients) suffered minor disabilities while patients in whom minimal or incomplete recanalization was achieved either suffered severe disability or a fatal outcome **(table 3-3)**. Nevertheless, our data statistically showed that the correlation was insignificant, thereby suggesting that recanalization outcomes did not affect 3-month functionality (*p = 0.193*).

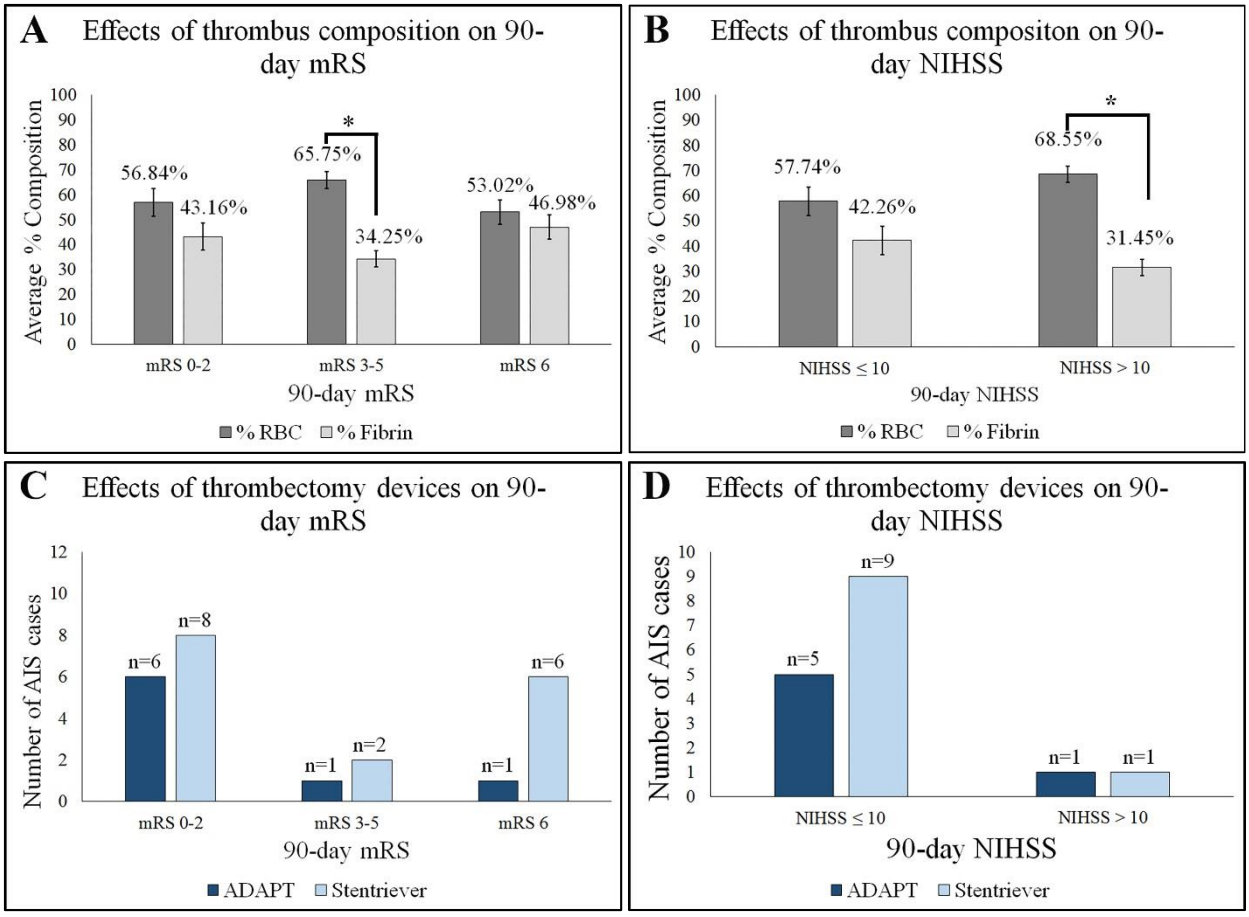

Figure 3-5: Correlation between the effects of various clinical parameters on 3-month functional outcomes. Graphs A and B show the effects of thrombus composition on mRS and NIHSS, respectively. Graphs C and D show the effects of EVT devices on mRS and NIHSS, respectively. mRS = Modified Rankin Scale (mRS 0-2: minor disabilities and no assistance required, mRS 3-5: moderate to severe disabilities with assistance required for daily activities, mRS 6: dead), NIHSS = National Institute of Health Stroke Scale (NIHSS ≤ 10 = minor stroke, NIHSS > 10 = severe stroke), AIS = Acute Ischemic Stroke, TICI = Thrombolysis in Cerebral Infarction. For graphs represented in the left panel, 2 pts were excluded from group (mRS 6) as they died of non-stroke related causes (GI bleeding and lung cancer), and for graphs represented in the right panel 8 pts had incomplete evaluation as they died within the 90 days with no 90-day NIHSS records. Significance: (A) $p = 0.003$, (B) $p = 0.01$. The values represented above the error bars in graph A and B are the mean percentages of thrombus composition.

Table 3-3: Comparison between TICI and mRS scores. Assessing the effects of recanalization outcomes on 3-month functionality.

Recanalization Score Total Sample (n = 28)	Functional Outcomes	P Value
TICI 1-2a (n = 2)	mRS 0-2 – 0 mRS 3-5 – 1 (50%) mRS 6 – 1 (50%)	*0.193*
TICI 2b-3 (n = 26)	mRS 0-2 – 15 (57.7%) mRS 3-5 – 3 (11.5%) mRS 6 – 8 (30.7%)	

It is important to consider other factors that are likely to correlate with poor prognostic outcomes such as the volume and duration of ischemia in neuroanatomically eloquent tissue, length of the thrombectomy procedure, procedural delays in initiation, and once underway, the number of retrieval attempts made. Additionally any possible procedural complications that might occur including distal embolization, vessel perforations and occurrence of ICH will contribute to outcome. We did not test for every potential factor involved in poor patient outcomes, but we did correlate the effects of longer procedural times and the number of retrieval attempts with 3-month functional outcomes. We found that as length of the thrombectomy procedure increased, the outcomes worsened. Of the 15 patients who suffered minor disabilities (mRS 0-2) after their EVT procedure, 66% (10/15) of those patients had their thrombus retrieved within 30 mins. On the other hand, of the 8 patients who died (mRS 6), 75% (6/8) of those patients had a longer procedural time, > 30 mins. Furthermore, 86.7% (13/15) of the patients with mRS 0-2, had their thrombus retrieved within ≤ 2 attempts. Despite these trends observed, statistical significance was not reached when correlating either of the two variables with the mRS scores *(p = 0.162 and 0.504)*, respectively.

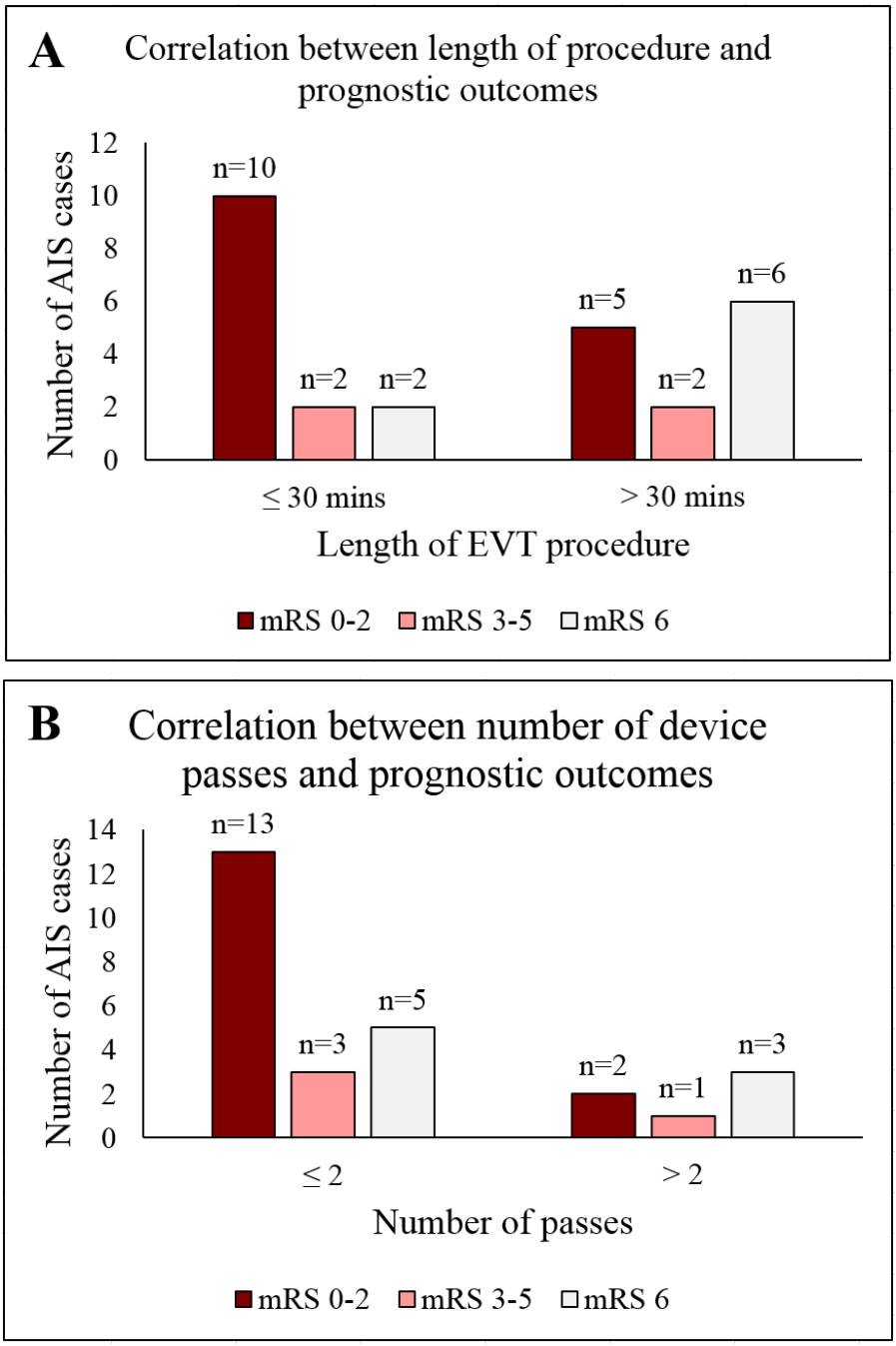

Figure 3-6: Correlation between procedural and functional outcomes. Bar graphs show a correlation between (A) the length of EVT procedure and mRS scores and (B) the number of retrieval attempts and mRS scores. AIS = acute ischemic stroke, EVT = endovascular therapy, mRS = Modified Rankin Scale.

3.4 Correlations between elemental distribution, thrombus composition and clinical parameters

Since the histological composition of a thrombus is not known pre-operatively, we aimed to identify thrombi using elemental markers, whereby we correlated elemental concentrations with their histological classifications to determine if elements distributed differently in erythrocyte-rich thrombi as opposed to fibrin-rich thrombi. The analysis of 16 thrombi on beamline 10-2 indicated statistically insignificant differences between elements found in erythrocyte-rich thrombi and fibrin-rich thrombi: P (*p = 0.945*), S (*p = 0.181*), Cl (*p = 0.534*), K (*p = 0.366*), Ca (*p = 1.000*), Fe (*p = 1.000*), Cu (*p = 0.051*) and Zn (*p = 0.073*) **(Fig 3-7)**.

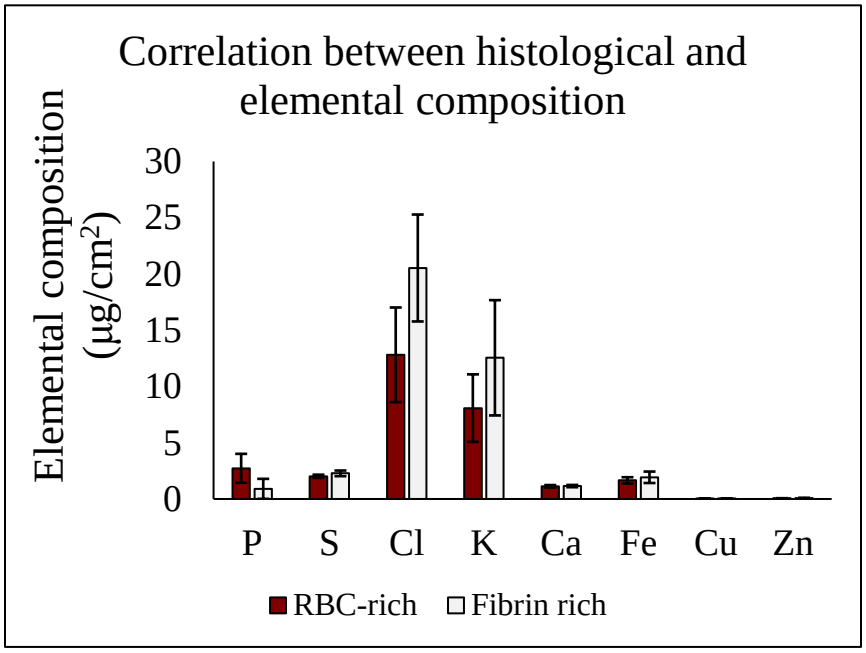

Figure 3-7: Correlation between histological and elemental composition. Bar graph compares concentration of various biological elements including phosphorous (P), sulfur (S), chlorine (Cl), potassium (K), calcium (Ca), iron (Fe), copper (Cu) and zinc (Zn) in RBC-rich and fibrin-rich thrombi. Elements were quantified from XFI maps produced on BL 10-2 at SSRL using Sam's Microprobe Analysis Kit (SMAK) software.

3.4.1 XFI distribution maps

XFI heat maps generated on beamline 10-2, characterizing the distribution of S, Cl, K, Ca, Fe, and Zn showed similar distribution patterns to XFI heat maps generated on beamline 14-3. Both maps revealed S and Cl to be abundant in the core and peripheral regions of the thrombi. Furthermore, K and Fe were elevated in erythrocyte-rich areas; whereas, Ca was dispersed in higher concentration in fibrin-rich areas of the thrombus. Cu and Zn levels were detected at trace

levels **(Fig. 3-8A and Fig. 3-9)**. Moreover, high resolution images collected for thrombus 24 on beamline 2-3 indicated elevated levels of K and Fe and reduced levels of Cl and Ca in the erythrocyte-areas of the thrombus, thereby revealing the same distribution pattern as observed on XFI maps produced on beamline 10-2 **(Fig. 3-8B)**.

Sulfur maps produced for 2 thrombi on BL 14-3 showed a strong difference between the distribution patterns of the three sulfur species. Sulfonic acid indicative of taurine was highly concentrated in fibrin-rich areas compared to erythrocyte-rich areas, sulfoxide indicative of methionine sulfoxide was abundantly dispersed throughout the thrombi while O-linked sulfate esters were barely detected (**Fig. 3-10)**.

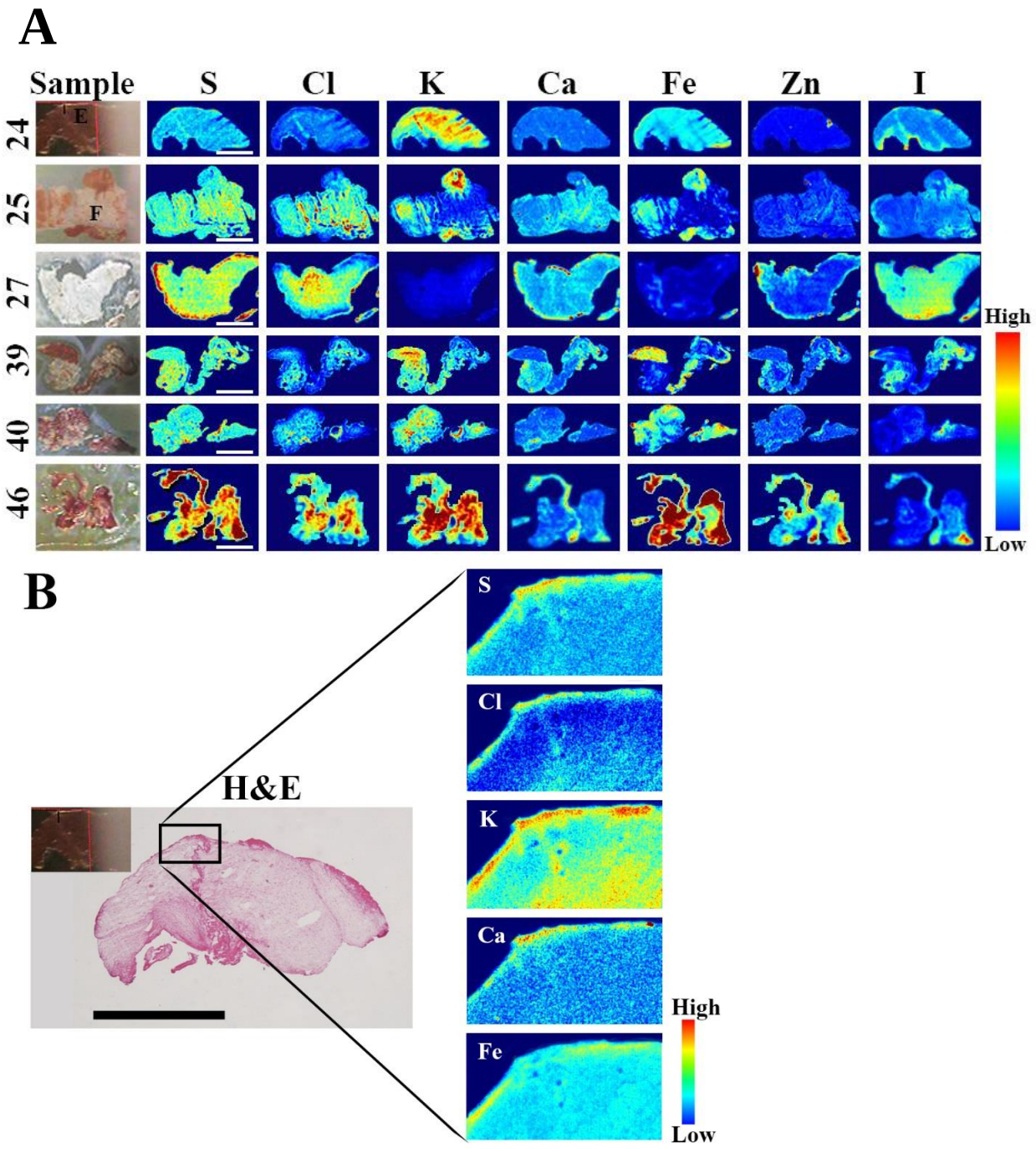

Figure 3-8: XFI elemental distribution pseudo coloured maps. (A) BL 10-2 generated heat maps show elemental distribution patterns for sulfur–S, chlorine–Cl, potassium–K, calcium–Ca, iron–Fe, zinc–Zn and iodine–I, present within the samples where rainbow matrix pseudo-colours are added to indicate high concentrations in red and low concentrations in blue. The left panel contains images of the untreated sample to indicate erythrocyte-rich (E) and fibrin-rich (F) regions of the thrombus. (B) BL 2-3 generated high resolution heat map for thrombus #24 shows the distribution of S, Cl, K, Ca and Fe in thrombus 24. Scale bar = 1mm (A), 80 μm (B).

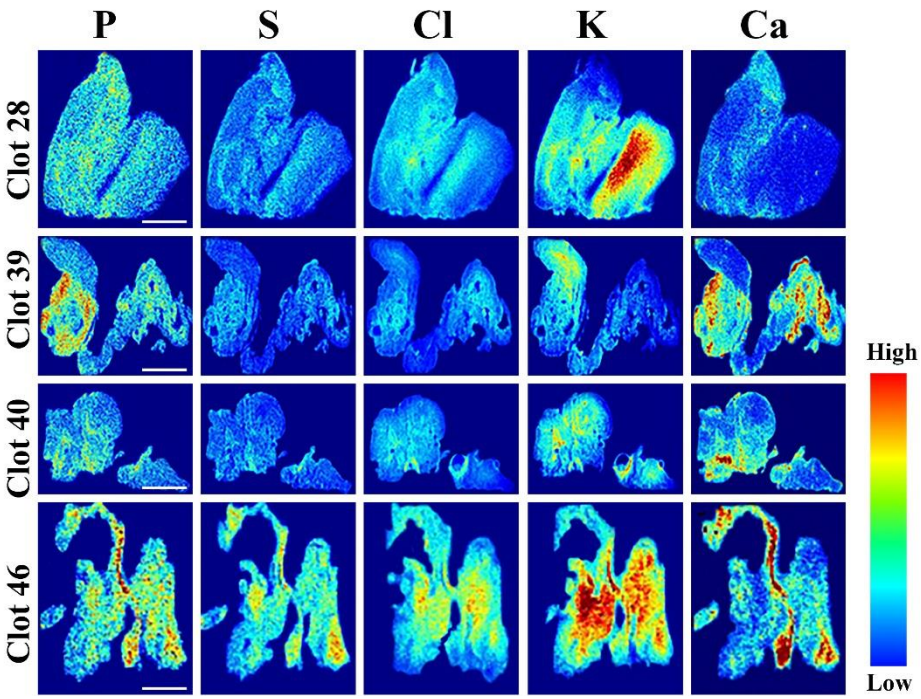

Figure 3-9: BL 14-3 XFI maps representing low Z elements. X-ray fluorescence imaging heat maps show elemental distribution patterns for phosphorous (P), sulfur (S), chlorine (Cl), potassium (K), calcium (Ca) where rainbow matrix pseudo-colours are added to indicate high concentrations in red and low concentrations in blue. Scale bar: 1mm.

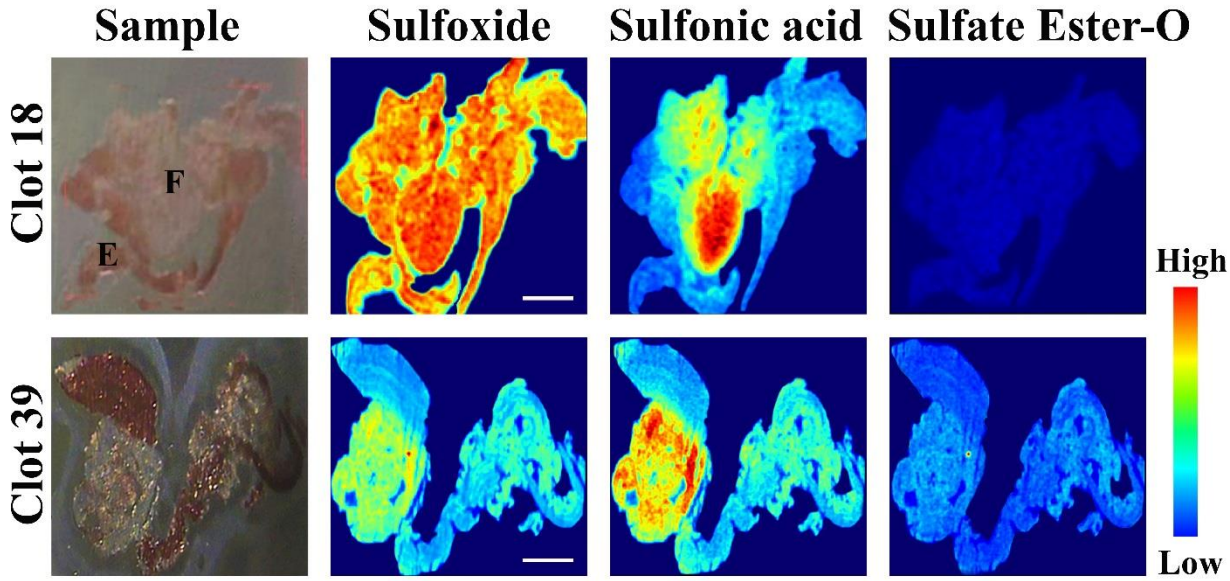

Figure 3-10: BL 14-3 XFI sulfur distribution pseudo coloured map. X-ray fluorescence imaging heat maps show different sulfur species, sulfoxide (methionine sulfoxide), sulfonic acid (taurine) and O-linked sulfate ester, present within the samples represented using rainbow matrix pseudo-colours to indicate high concentrations in red and low concentrations in blue. The left panel contains images of the untreated samples mounted on thermox coverslips indicating erythrocyte-rich (E) and fibrin-rich (F) areas. Scale bar: 2mm.

3.4.2 Spectroscopy: XAS and FTIR maps

Analysis of the normalized Fe spectra generated by XAS for 4 thrombi samples, presented the Fe pre-edge spectral peaks at 7,112.7 eV **(Fig. 3-11A)**. When these peaks were compared to various Fe standard compounds of different oxidation states, the spectral peaks derived from the thrombus samples were similar to the peak indicative of oxygenated hemoglobin characterized at 7,113 eV **(Fig. 3-11B)** [164]. However, to validate if the Fe pre-edge spectra represents oxygenated hemoglobin, peak fitting would have to be performed in the future.

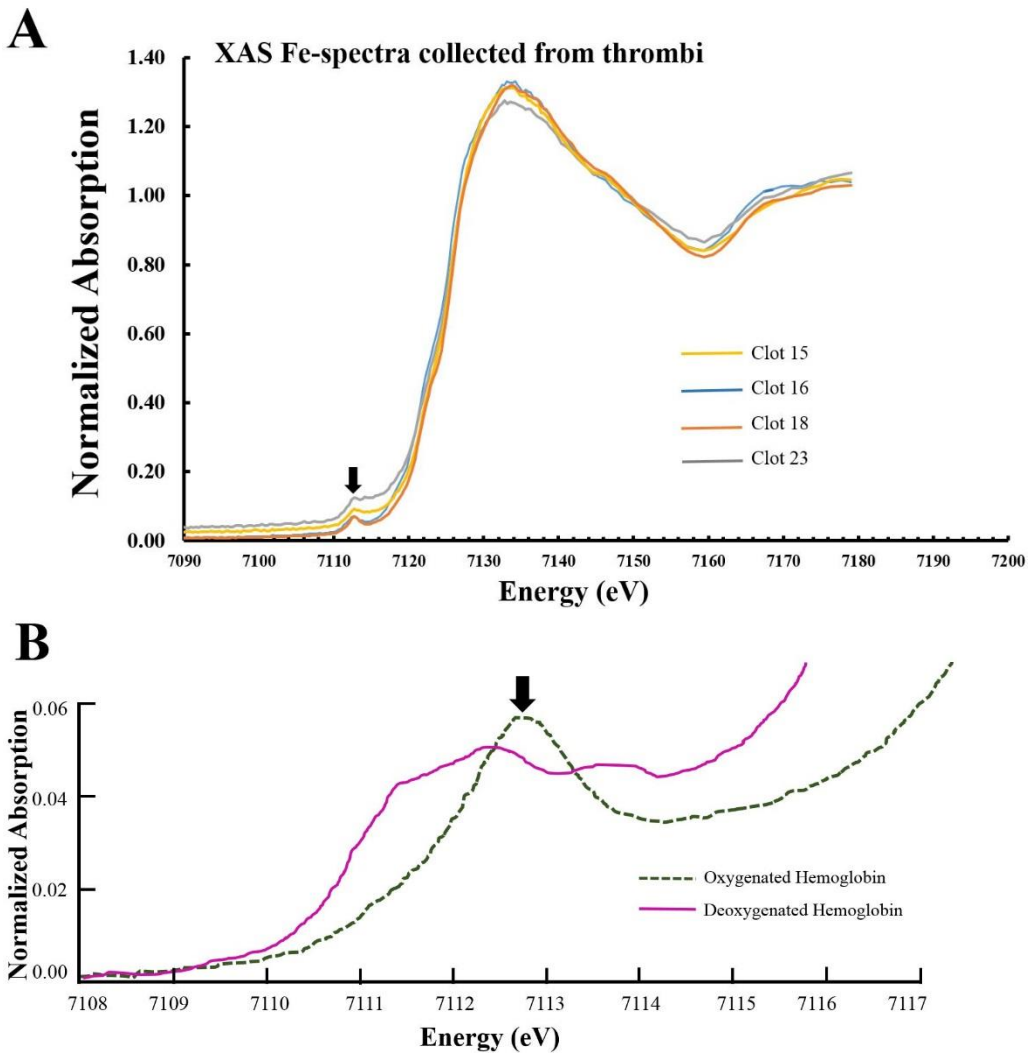

Figure 3-11: Fe Spectroscopy. (A) Normalized Fe K-edge XAS spectra collected from thrombus samples on beamline 7-3 at SSRL. (B) The Fe K-edge reference spectra of oxygenated and deoxygenated hemoglobin redrawn from Wilson SA *et al.* [164]. The pre-edge spectral peak at ~7,113 eV in thrombus samples represents oxygenated hemoglobin (black arrow).

The distribution maps produced by infrared spectroscopy on Mid-IR beamline indicated a higher presence of amide I and amide II bands in the erythrocyte-rich regions, platelets to be co-localized in the fibrin-rich regions whereas, fibrinogen, glutamate and cholesterol esters to be present throughout the thrombi with no specific distribution patterns **(Fig. 3-12)**.

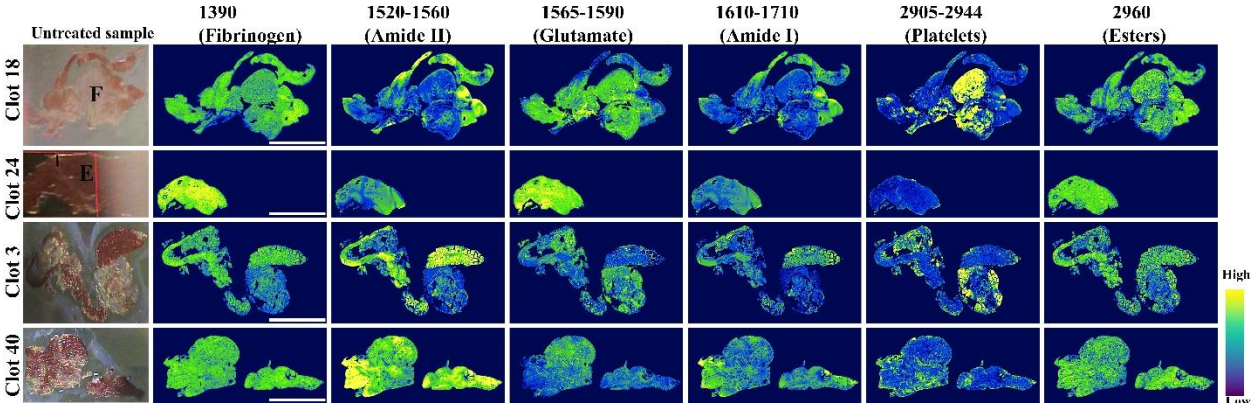

Figure 3-12: FTIR distribution map. Spatiotemporal comparison of organic biomolecules distributed in the fibrin-rich (F) and erythrocyte-rich (E) regions of the cerebral thrombi represented using bgy (blue green yellow) pseudo-colours to indicate high concentrations in yellow and low concentrations in blue. Scale bar = 1mm.

3.4.3 Effects of stroke etiology on elemental composition and organic molecules in thrombi

XFI analysis of 16 samples revealed that elemental composition of thrombi was not altered by stroke etiology such that, the differences in areal concentration (μg/cm^2) of all elements of interest between artery-to-artery emboli and cardioemboli were statistically insignificant: P ($p = 1.000$), S ($p = 0.792$), Cl ($p = 0.958$), K ($p = 0.792$), Ca ($p = 0.428$), Fe ($p = 0.562$), Cu ($p = 0.713$), and Zn ($p = 0.958$) **(Fig. 3-13A)**.

Similarly, FTIR analysis for 15 of the 16 samples (1 sample was damaged) collected adjacent to XFI samples, showed that thrombi originating from either of the two sources, artery-to-artery embolism or cardioembolism were insignificantly different in their biochemical composition (measured by area under the curve, units: A.U.) of lipids ($p = 0.56$), platelets ($p = 0.48$), glutamate ($p = 0.41$), amide I ($p = 0.09$), amide II ($p = 0.13$), cholesterol esters ($p = 0.72$), and

fibrinogen ($p = 0.64$), suggesting that stroke etiology had no effect on organic molecules characterizing thrombus composition **(Fig. 3-13B-C)**.

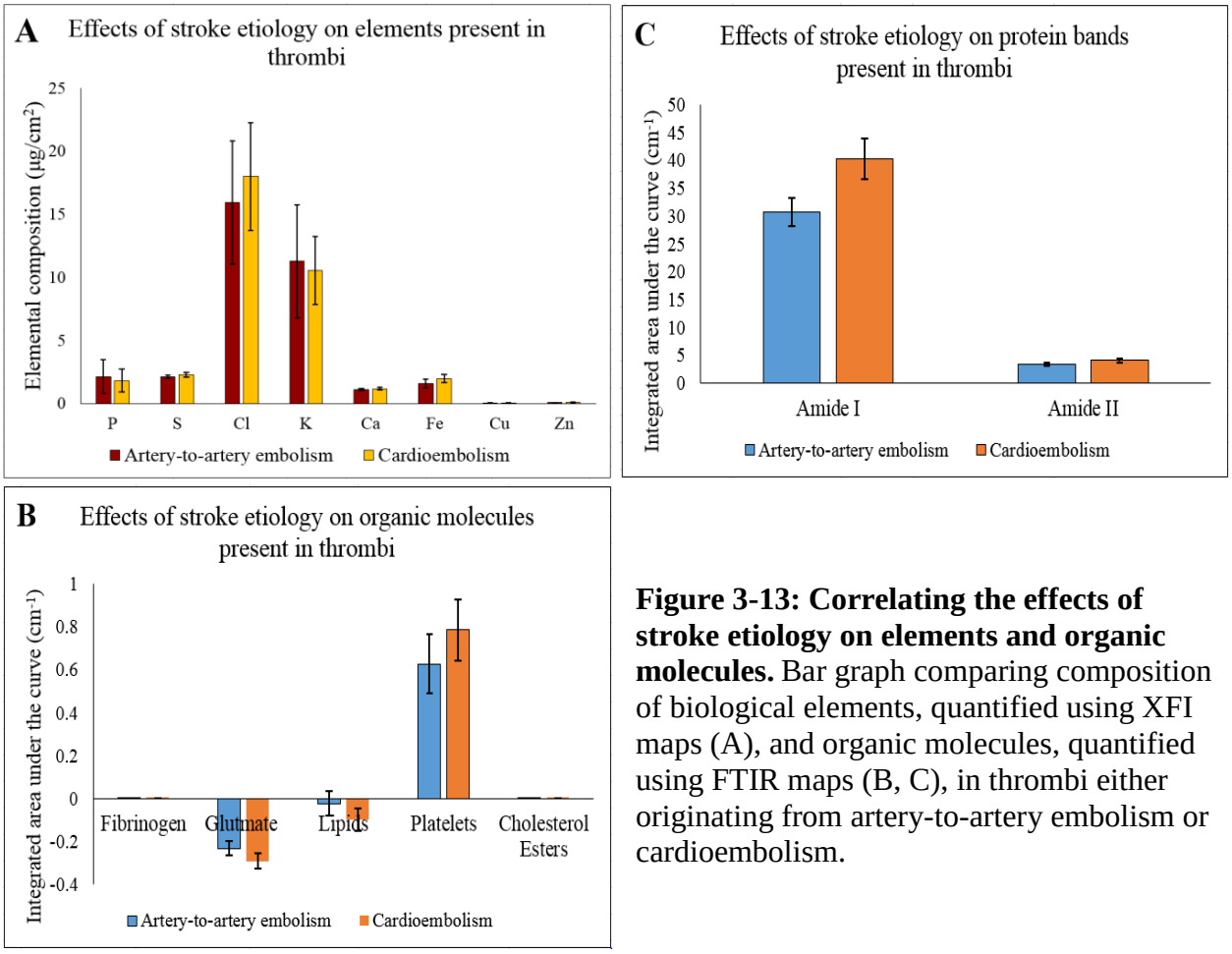

Figure 3-13: Correlating the effects of stroke etiology on elements and organic molecules. Bar graph comparing composition of biological elements, quantified using XFI maps (A), and organic molecules, quantified using FTIR maps (B, C), in thrombi either originating from artery-to-artery embolism or cardioembolism.

3.4.4 Effects of elemental composition and organic molecules on recanalization and 3-month functional outcomes

Thrombi that resulted in either partial or incomplete recanalization (TICI 1-2a) had higher concentration of Cl and K than thrombi that resulted in near-to-complete recanalization (TICI 2b-3). However, there was no statistical significance observed when elemental concentrations were compared across the two groups, TICI 1-2a and TICI 2b-3: P ($p = 0.998$), S ($p = 0.999$), Cl ($p = 0.999$), K ($p = 0.998$), Ca ($p = 0.999$), Fe ($p = 0.998$), Cu ($p = 0.998$), and Zn ($p = 0.998$) **(Fig. 3-14A)**. Similarly, when mRS scores were compared with elemental composition to assess

if elements within the thrombi contributed to severe functional outcomes, there were no statistically significant differences observed within the three mRS groups for any of the elements of interest **(Fig. 3-14B)**, suggesting that biological elements were not a contributory factor in determining long-term functionality.

FTIR results showed no significant relationship between organic biochemical composition and recanalization success in either of the two groups, TICI 1-2a and TICI 2b-3: lipids ($p = 0.510$), glutamate ($p = 0.475$), platelets ($p = 0.361$), cholesterol esters ($p = 0.760$), fibrinogen ($p = 0.473$) and amide I ($p = 0.426$) **(Fig. 3-15A-C)**. Similarly, there was no significant relationship between organic biochemical composition and mRS score in either of the three groups, mRS 0-2, mRS 3-5, and mRS 6: lipids ($p = 0.621$), glutamate ($p = 0.436$), platelets ($p = 0.887$), cholesterol esters ($p = 0.881$), fibrinogen ($p = 0.892$) and amide I ($p = 0.777$) **(Fig. 3-15D-F)**.

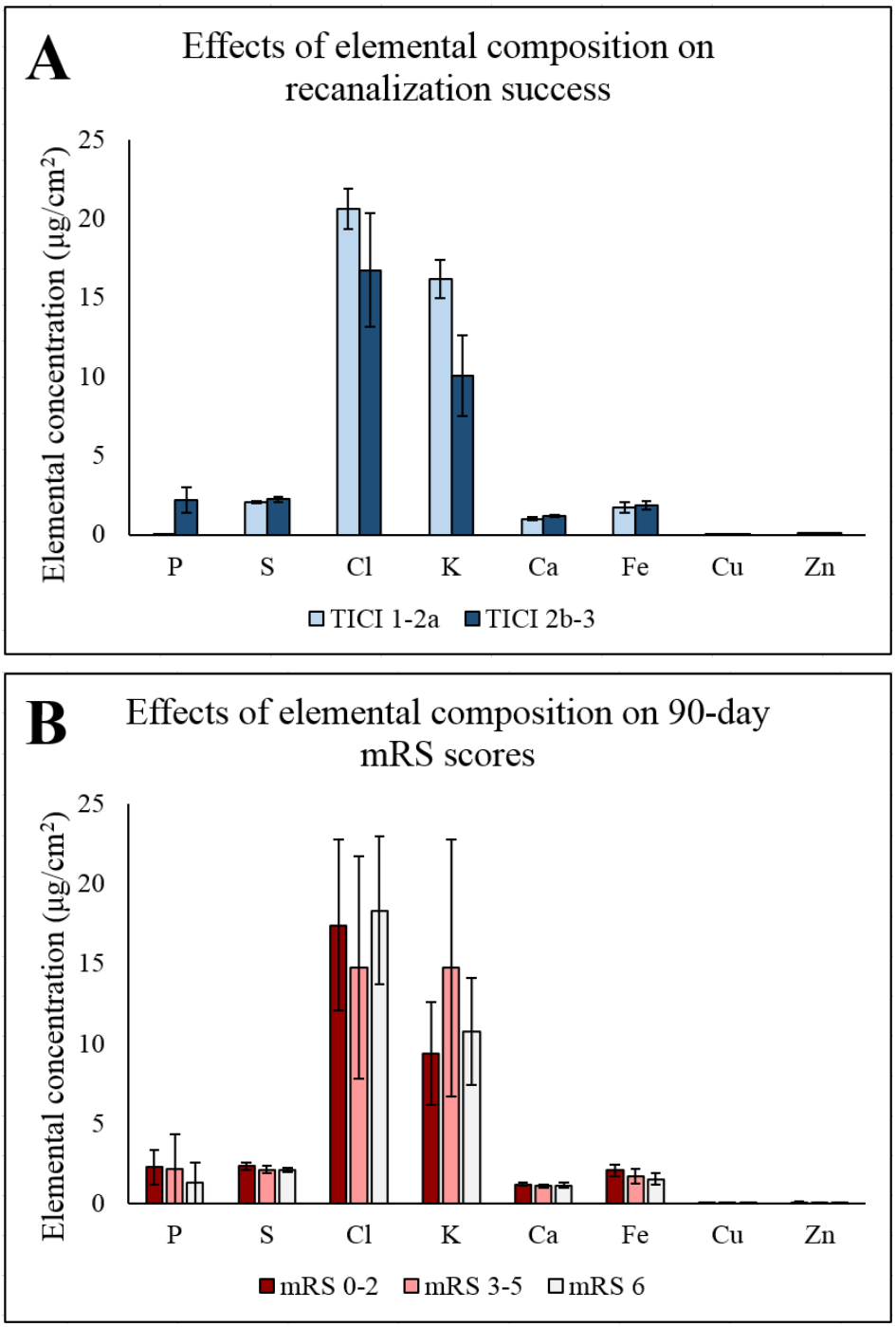

Figure 3-14: Correlating elemental with clinical outcomes. Bar graphs comparing the effects of various biological elements, quantified using XFI maps, on recanalization success (A) and 3-month functional outcomes (B). TICI = Thrombolysis in Cerebral Infarction (TICI 1-2a: partial/incomplete recanalization, TICI 2b-3: near to complete recanalization), mRS = Modified Rankin Scale (mRS 0-2: minor disabilities, mRS 3-5: moderate to severe disabilities, mRS 6: dead).

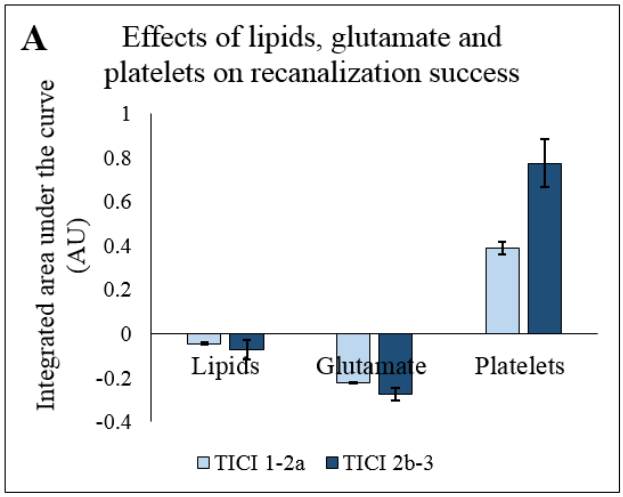
A
Effects of lipids, glutamate and platelets on recanalization success
Integrated area under the curve (AU)
1
0.8
0.6
0.4
0.2
0
-0.2
-0.4
Lipids
Glutamate
Platelets
TICI 1-2a
TICI 2b-3

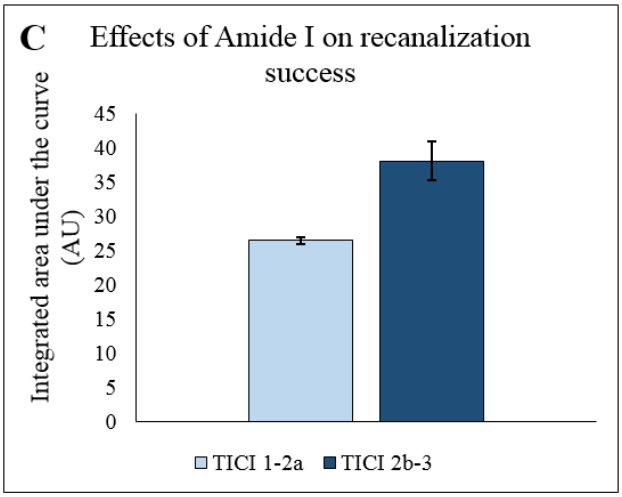
C
Effects of Amide I on recanalization success
Integrated area under the curve (AU)
45
40
35
30
25
20
15
10
5
0
TICI 1-2a
TICI 2b-3

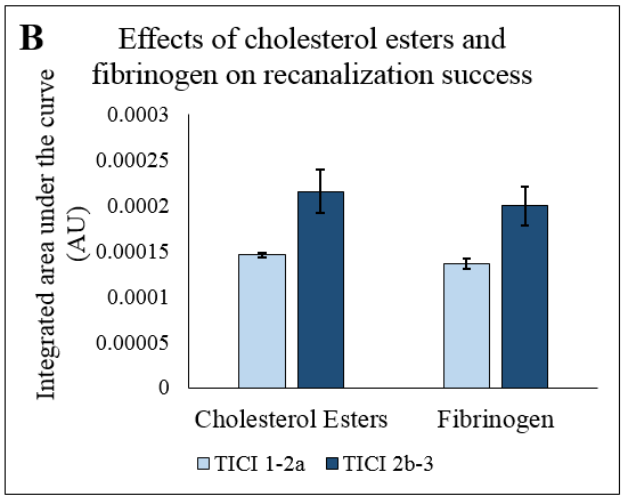
B
Effects of cholesterol esters and fibrinogen on recanalization success
Integrated area under the curve (AU)
0.0003
0.00025
0.0002
0.00015
0.0001
0.00005
0
Cholesterol Esters
Fibrinogen
TICI 1-2a
TICI 2b-3

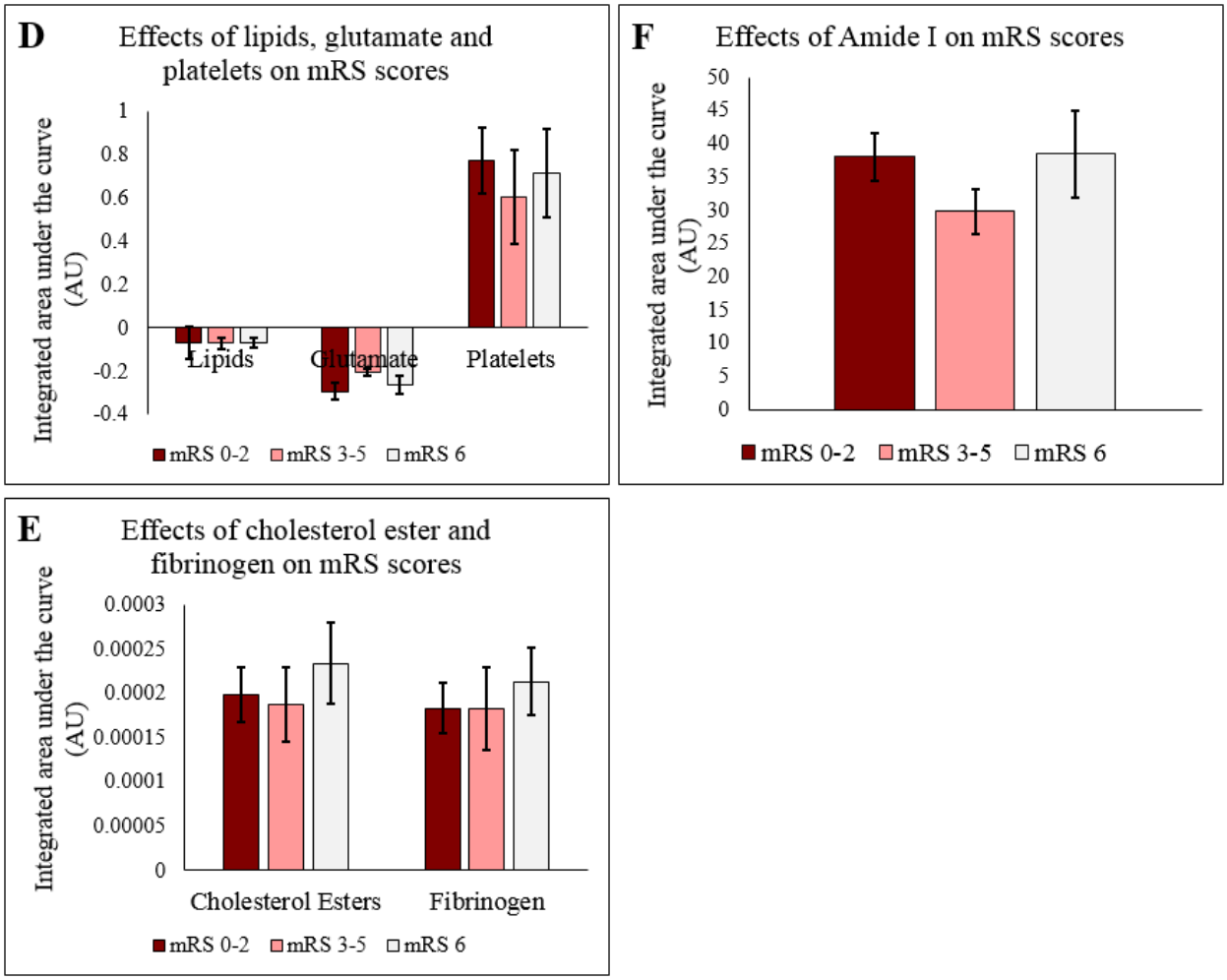

Figure 3-15: Correlating biochemical composition with clinical outcomes. Bar graphs comparing the effects of various organic molecules, quantified using FTIR maps, on recanalization success (A-C) and 3-month functional outcomes (D-F). TICI = Thrombolysis in Cerebral Infarction (TICI 1-2a: partial/incomplete recanalization, TICI 2b-3: near-to-complete recanalization), mRS = Modified Rankin Scale (mRS 0-2: minor disabilities, mRS 3-5: moderate to severe disabilities, mRS 6: dead), A.U. = Absorbance Units.

3.5 Thrombus perviousness

The presence of iodine was used as a biomarker to measure thrombus perviousness. Qualitative assessment of XFI distribution maps generated on beamline 10-2 revealed that iodine levels were elevated in fibrinous regions of the thrombus and did not penetrate regions containing high erythrocyte proportions, thereby suggesting that fibrin-rich clots were more pervious than erythrocyte-rich thrombi **(Fig. 3-16A)**.

Additionally, to determine if stroke etiology correlated with thrombus perviousness and whether thrombus perviousness correlated with clinical outcomes, we measured the amount of contrast agent in the thrombus and correlated the total iodine concentration (μg/cm^2) with stroke etiology and recanalization outcomes. Our data showed that thrombi originating from artery-to artery emboli had higher iodine concentration than cardioemboli (*p = 0.958*) **(Fig. 3-16B)**. Also, patients in whom a score of TICI 1-2a was achieved had lower iodine concentration than patients in whom a score of TICI 2b-3 was achieved (*p = 0.834*) **(Fig. 3-16C)**, suggesting that thrombi that resulted in near-to-complete recanalization were more pervious than thrombi that resulted in minimal-to-incomplete recanalization; however, we did not achieve statistical significance at n = 16

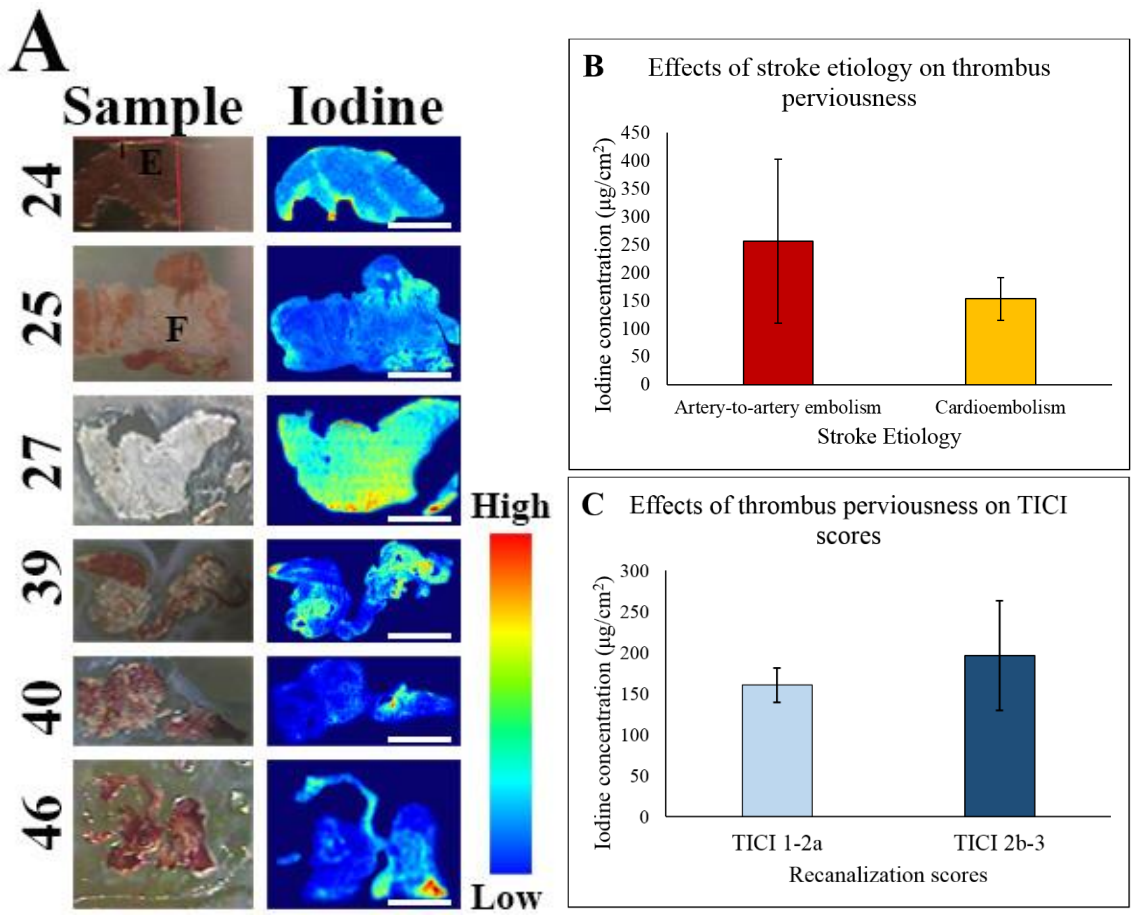

Figure 3-16: Effects of thrombus perviousness on clinical outcomes. (A)XFI distribution map represents iodine permeability with elevated iodine levels in fibrin rich areas and lower

permeability of iodine in erythrocyte rich areas, denoted by letter F and E, respectively. Graphs B and C correlate iodine concentration ($\mu g/cm^2$) quantified from X-ray fluorescence imaging distribution maps with stroke etiology and recanalization outcomes, respectively.

3.6 Summary of the results

In summary, our findings suggest the following:

1) The dichotomous classification of thrombi as red or white based on just histological constituents and stroke etiology is an oversimplified and invalid classification paradigm.

2) Thrombus composition was not affected by stroke etiology. Even though cardioemboli were composed of significantly higher proportion of erythrocytes than fibrin ($p = 0.009$), comparing proportions of erythrocytes between cardioemboli and artery-to-artery emboli revealed insignificant differences ($p = 0.437$).

3) Patients with NIHSS $\leq$ 10 had significantly higher erythrocytes than fibrin in their thrombi ($p = 0.0014$). However, comparing proportions of RBCs and fibrin across the two NIHSS groups revealed that thrombus composition had no effect on the pre-treatment NIHSS scores. Even though the area occupied by erythrocytes was greater in patients with NIHSS $\leq$ 10 (65.37% *vs* 53.30%) and the area occupied by fibrin was greater in patients with NIHSS > 10 (46.70% *vs* 34.63%), the differences were statistically insignificant ($p = 0.19$) suggesting no correlation between histological thrombus composition and baseline severity.

4) The effectiveness of a thrombectomy device was not associated with histological composition. Patients treated with stentrievers had thrombi composed of higher proportions of erythrocytes than patients treated with ADAPT (57.36% *vs* 55.81%). Accordingly, the area occupied by fibrin was higher in patients treated with ADAPT than patients who were treated with stentrievers (44.19% *vs* 43.64%). However, these differences were statistically insignificant ($p = 0.833$).

5) Patients with near-to-complete recanalization (TICI 2b-3) had thrombi composed of significantly higher proportions of erythrocytes and lower proportions of fibrin (57.37% *vs* 42.69%, $p = 0.01$) than patients with incomplete recanalization (TICI 1-2a) but, comparisons of erythrocyte or fibrin proportions across the two TICI groups revealed statistically insignificant differences ($p = 0.657$).

6) Thrombus composition had no effect on 3-month functional outcomes assessed by 90-day mRS and 90-day NIHSS. In fact, regardless of the mRS group the patient belonged to, mRS 0-2, mRS 3-5 or mRS 6, the composition revealed higher proportions of erythrocytes than fibrin in each of the three groups (56.84% *vs* 43.16, 65.75% *vs* 34.25%, 53.02% *vs* 46.98%) with overall non-significant differences ($p = 0.892$). Similarly, for the 90-day NIHSS categories, thrombi of patients in either of the NIHSS categories (≤ 10, > 10) revealed higher proportions of erythrocytes than fibrin (57.74% *vs* 42.26%, 68.55% *vs* 34.45%) with non-significant differences overall ($p = 0.512$).

7) The choice of thrombectomy device did not influence recanalization ($p = 0.536$), 90-day mRS ($p = 0.363$) or 90-day NIHSS outcomes ($p = 0.869$).

8) There was no association between recanalization success and 3-month functional outcomes. Even though a majority of the patients in whom near-to-complete recanalization (TICI 2b-3) was obtained had mRS ≤ 2 than those patients in whom recanalization was not obtained, the overall differences were statistically insignificant ($p = 0.193$).

9) XFI heat maps collected on beamline 10-2 revealed abundant presence of S and Cl in all samples. On the other hand, K and Fe were elevated in erythrocyte-rich regions while Ca was concentrated in fibrin-rich regions of the thrombus. Cu and Zn were detected at very low

quantities. Nevertheless, quantification of elements from XFI heat maps revealed insignificant differences between RBC-rich and fibrin-rich thrombi: P ($p = 0.775$), S ($p = 0.317$), Cl ($p = 0.568$), K ($p = 0.475$), Ca ($p = 0.668$), Fe ($p = 0.668$), Cu ($p = 0.199$) and Zn ($p = 0.063$). Furthermore, XFI heat maps collected on beamline 14-3 revealed distribution differences in sulfur species wherein, sulfonic acid (taurine) was highly concentrated in fibrin-rich areas of the thrombi.

10) Analysis of the X-ray absorption spectroscopy data revealed that the Fe pre-edge spectra was representative of oxygenated hemoglobin present in the thrombi. However, pre-edge peak fitting is required to validate this finding.

11) Stroke etiology did not alter the elemental or biochemical composition of thrombi. Moreover, elemental and biochemical composition of thrombi did not correlate with recanalization or 3-month functional outcomes.

12) Patients in whom near-to-complete recanalization was obtained, had elevated concentration of iodine in their thrombi, but the data was statistically insignificant ($p = 0.834$). Subsequently, XFI distribution maps illustrated high iodine permeability through fibrinous regions of the thrombus. There was no statistical difference between stroke etiology and thrombus perviousness ($p = 0.958$).

Chapter Four: Discussion

Endovascular techniques have improved tremendously over the last two decades, from catheter-dependent intracranial delivery of thrombolytic drugs to the development of 2nd generation stent-retrievers [64]. Positive results from randomized controlled trials conducted worldwide demonstrated superior efficacy of EVT compared to IV-tPA treatment alone, and led endovascular therapy to be the standard of care for AIS patients [60], [62], [73], [75], [76]. However, studies have suggested the following: more than the specific device, rapid and safe recanalization might depend on other factors too, such as; pre- and post-treatment management, local *versus* general anaesthesia [59], anatomy of large vessel occlusions (LVO), mechanism of occlusion formation, size and location of vessel occlusion, collateral flow status, high rates of fragmentation and thrombus characteristics including composition, density/burden and length of the thrombus [165]. While all the above listed factors play a dynamic role in determining the clinical outcomes of stroke treatment, we were particularly interested in investigating the correlation between thrombus characteristics and interventional parameters as well as long-term clinical outcomes, as thrombi are the proximate cause of ischemic strokes and the primary target of current stroke treatments [81]. Hence, we aimed to investigate the histological, elemental and biochemical composition within retrieved thrombi to determine the clinical impact of composition on endovascular efficacy, interventional parameters and clinical outcomes in patients with acute ischemic stroke (AIS). To answer the research questions proposed in this study, we used a multitude of techniques including conventional histology and immunohistochemistry, X-ray fluorescence imaging and Fourier-transform infrared spectroscopy.

4.1 Validity of classifying thrombi as red and white based on histopathology and etiology

Analysis of the histological composition revealed that all thrombi were composed of similar structural components including; erythrocytes, platelets (vWF/Factor VIII), endothelial cells (CD31), fibrin, neutrophils, and eosinophils which were constituted into unique histological entities and proportions with each demonstrating a distinct pattern. For instance, in some thrombi, erythrocytes were present abundantly within the core, while fibrin/platelets and endothelial cells were distributed in the periphery. On the other hand, in some thrombi, erythrocytes were distributed in the periphery while the core was interspersed with fibrin and polymorphonulcear cells. In addition to the predominant components, all thrombi had abundant macrophage infiltration and presence of granular debris which we speculate were either byproducts or metabolites produced by macrophages. The first histopathological evaluation of cerebral thrombo-emboli was conducted in 1964 by Torvik and Jörgensen [84]. They conducted analysis on <1.5 months old vascular obstruction in post-mortem cases and reported the histopathological components of thrombi within the occluded vessel emphasizing on the process of thrombus organization. For instance, red blood cells packed closely together were attributed to vascular stasis, while organizing fibrin-platelet materials were attributed to the age of the cerebral infarct [166]. They were also the earliest to experimentally study histological differences in arterial and venous thrombi of varying age [167]. However, Marder *et al.* performed the first systematic histological analysis in freshly retrieved thrombi to identify fibrin, platelets and nucleated cells [85]. Almekhlafi *et al.* were the first to identify the presence of calcium and endothelial cells in freshly retrieved thrombi [86]. Despite many previous works that have reported the presence of common histological components of fibrin, platelets, erythrocytes and white blood cells, every thrombus is comprised of a different histological pattern as well as

ratios of these components [168], and it remains controversial whether either of these components predominantly affects clinical parameters [163].

In this study, thrombi that had a predominance of red blood cells were classified as erythrocyte-rich while thrombi that had a predominance of fibrin were classified as fibrin-rich. However, the terminology used for distinguishing thrombi based on their predominant histological component is quite contradictory within literature. For instance, some previous studies have termed erythrocyte-rich thrombi as red while fibrin-rich thrombi as white [85], [87]. On the other hand, some studies have defined red thrombi as being rich in erythrocytes and fibrin while white thrombi being rich in platelets and fibrin [169], [170]. However, since we found that platelets and endothelial cells only co-localized in fibrin-rich areas [171], we defined the two dominant components of thrombi as erythrocytes and fibrin rather than erythrocytes and platelets.

Sheer number of studies have focused on histological characterization of thrombus. Yet, the studies are limited by a lack of uniformity in histologically characterizing thrombi [172]. In fact, discrepancies observed in the classification of thrombi may be attributed to non-standardized assessment tools leading to biases induced by specimen fixation, processing, staining, interpreting results and measuring levels of each component using different methods [163]. In fact, some studies have quantified thrombi as red or erythrocyte-rich if RBCs outnumbered fibrin/collagen by > 15% [87], [173] while some others have used a Positive Pixel Count Algorithm or other semi-qualitative analysis tools and applied a semi-automated colour segmentation [163], [91], [95]. Furthermore, even though most semi-quantitative or semi-qualitative methods have utilized PhotoShop and ImageJ to measure erythrocytes, leukocytes, and fibrin/platelet composition within thrombi, researchers have not adhered to standardized

colour and intensity parameters during analysis. Lastly, some papers do not mention the parameters used in their study [95], [174].

Histological characterization of thrombi using conventional stains and immunohistochemical tools has been retrospective in nature. Thus, some studies have suggested an approach in delineating thrombotic occlusions by using non-invasive imaging techniques. In fact, for over 30 years, studies have utilized non-invasive modalities for identifying early vessel signs indicative of occlusive thrombus such as Hyperdense Middle Cerebral Artery Signs (HMCAS) [175]. However, some of these older studies have not corroborated the histopathology of the underlying thrombus [81]. Liebeskind *et al.* was the first study to correlate HMCAS and Blooming Artifact (BA) using non-contrast computed tomography (NCCT) and echo-gradient MRI with thrombus histopathology to determine its effects on clinical outcomes in patients who underwent thrombectomy. They found that HMCAS and BA were indicative of thrombi composed of higher proportions of erythrocytes than fibrin [162]. This finding was later supported by another study in which they associated increased thrombus attenuation (> HU) with the presence of high amounts of erythrocytes in the thrombus [173]. Thrombus attenuation (*i.e.* Hounsfield Units, HU) has shown to have a linear correlation with hemoglobin and weak negative correlation with platelets in the thrombi [173], [176]. Thus, platelet-rich thrombi have been identified as isodense on NCCT [177].

Historically, thrombi were also classified as red/erythrocyte-rich or white/fibrin and platelet-rich based on their source of origin or etiology. While it is true that thrombi vary in architecture, rigidity, and morphology based on their predominant cellular component (erythrocyte or fibrin), it is not necessarily true that these features are also affected by their source of origin. This study showed that there was no correlation between thrombus composition and stroke etiology [85]. In

fact, regardless of where the thrombi were dislodged from, heart or the proximal arteries, the percent of erythrocytes in all thrombi were higher than the percent of fibrin. Many studies in the past have revealed that thrombi originating from a cardiac source led to the development of fibrin-rich thrombi while thrombi originating from proximal arteries led to the development of erythrocyte-rich thrombi [178], [171], [95], [179]. On the contrary, authors of some studies have also credited the distinctive proportions in composition to the chaotic forces of blood flow, shear and turbulence at sights of thrombus initiation and growth suggesting that, thrombi originating from a cardiac source with low blood flow led to the development of red or erythrocyte-rich thrombi while thrombi originating from an arterial source with high blood flow led to the development of *in situ* arterial thrombosis mediated by platelet-aggregated white or fibrin-rich thrombi [87], [169], [173]. With such discrepancies in the previous studies as well as the present study revealing a nonsignificant correlation between thrombus composition and stroke etiology, it is clear that the histological composition of thrombus is not altered by its source of origin. Observing such heterogeneity of thrombus composition, the conventional classification of red *versus* white thrombi seems truly inapplicable [168].

Moreover, as shown in table 3-1, the predominant component defining the histological category of the thrombus changes from section-to-section, wherein for instance, if one section collected from the proximal end shows higher proportions of erythrocytes, the next section collected from the distal end shows higher proportions of fibrin, thereby challenging the classification of a thrombus based on its dominant composition. To avoid such biases in section-analysis, studies have suggested total thrombus analysis (*i.e.* bulk analysis) [163]. However, there are two drawbacks to this method including: 1) limiting the use of alternative staining tools required for characterizing other cellular entities and 2) thrombus fragmentation that occurs during the

procedure whereby some smaller fragments are lost or eliminated from bulk analysis. A previous study reported that in > 90% of the cases, primary occlusions occur due to a single thrombus [180] and any occlusions distal from the primary occlusion site are considered to occur due to periprocedural thrombus fragmentation [181]. That being said, why some thrombi are more prone to fragmentation – remains unclear. Some studies have attributed higher proportions of red blood cells in causing thrombus mobilization and fragmentation [92] while some have suggested the role of neutrophil invasion [181], even though white blood cells only make up 3.9% of the histological composition [177]. Qualitative assessment of neutrophil distribution in this study indicated a higher presence of neutrophils in fibrin-rich areas than erythrocyte-rich areas. This finding was expected, as neutrophils are known to exhibit fibrinolytic activity that potentially weaken thrombus stability and promote fragmentation [181]. But since we did not perform a quantitative analysis of neutrophil infiltration, we could not determine the role of neutrophils in promoting fragmentation.

4.2 Data trends and literature overview

Our study showed no correlation between thrombus composition and pre-treatment NIHSS scores. To date, very few studies have investigated the effects of thrombus composition on pre-treatment NIHSS. Similar to this study, Kim *et al.* reported no correlation between histologic composition and initial stroke severity [174]; however, the authors of the study did not provide data for this correlation. Boeckh-Behrens *et al*. revealed that post-treatment NIHSS was influenced by percentage of leukocytes but not erythrocytes or fibrin where higher percentage of white blood cells were associated with less favourable post-treatment NIHSS scores [182]. Choi *et al.* reported a significant increase in baseline NIHSS scores as the RBC fractions increased ($p = 0.043$) [91] which contradicted our data showing significantly higher RBCs in patients with

decreasing NIHSS scores (NIHSS ≤ 10). Prochazka *et al.* indirectly investigated the correlation between thrombus composition and patient outcomes by assessing biomarkers such as vWF and ADAMTS13 (vWF-cleaving protease) in 131 retrieved thrombi. They found patients with increasing NIHSS scores (NIHSS ≥ 15) had significantly higher levels of vWF [183]. Similarly, Schuhmann *et al.* also reported a positive correlation between high pre-treatment NIHSS scores and the presence of increased vWF [87].

When engaging a thrombus with a thrombectomy device, optimal interventional outcomes are likely best achieved when the entire thrombus is engaged with the device and retrieved in one pass, preventing distal fragmentation [172]. When this does not happen, it is possible that the mechanical properties (texture, stiffness, and adherence) of the thrombus play a role in the choice of device as well as the success of achieving favourable outcomes. However, it is still debatable whether choice of therapies ought to take into consideration thrombus composition and its role in predicting interventional and clinical outcomes [168]. Our data showed no correlation between thrombus composition and the thrombectomy device that resulted in successful retrieval. Likewise, another study supported similar findings and revealed no association between thrombus composition and retrieval device [177]. On the other hand, our data contradicted previous work by Shin *et al.* in which retrospective analysis revealed that thrombi retrieved by ADAPT had higher percentage of red blood cells while thrombi retrieved via stentrievers were composed with higher proportions of fibrin [163]. Another study showed that thrombi rich in erythrocytes were retrieved more successfully via stentrievers alone and required reduced number of maneuvers [95]. This was likely due to the fact that fibrin-rich thrombi had a higher coefficient of friction and thereby adhered strongly to the vessel wall [184]. Another study reported that fibrin-rich thrombi required higher number of attempts during EVT as well as

contributed to higher rates of incomplete reperfusion than RBC-rich thrombi. Authors attributed these outcomes to fibrin structure suggesting the influence of fibrinous rigidity on thrombus engagement and its tendency to disengage at the tip of the guiding catheter [92].

Moreover, this study also revealed no correlation between thrombus composition and recanalization outcomes when comparing erythrocyte and fibrin proportions among the two TICI groups. However, comparing erythrocyte and fibrin proportions only for patients in whom TICI 2b-3 was achieved, the data revealed that the thrombi in this group had significantly higher erythrocytes than fibrin. Some studies have reported similarly where patients with thrombi composed of higher proportions of erythrocytes had higher success rate for complete recanalization [163], [185] while some have contradicted this finding and suggested RBC-rich thrombi to result in low recanalization success due to the ability of RBC-rich thrombi to induce distal migration [186] or increase the risk of thrombosis by increasing blood viscosity [187]. Some studies utilizing non-enhanced computed tomography (NECT) and NCCT revealed a strong significant correlation between increased thrombus density, *i.e.* hyperdense thrombus, and increased recanalization success [172], [176], [188], while other studies suggested otherwise, revealing no correlation between thrombus density or thrombus burden with recanalization outcomes [189], [190]. Furthermore, our data showed no correlation between thrombus composition and 3-month functional outcomes which were assessed by 90-day mRS and 90-day NIHSS scores. Similarly, a previous study supported our findings showing no correlation between histological composition of thrombus and functional outcomes [95] as well as no correlation between thrombus density measured on NCCT and functional outcomes [189].

Even though the effectiveness of EVT has been proven beyond reasonable doubt, the key challenge is to implement it safely when maneuvering through tortuous or ectatic vessels with

unfolded aortic arch or redundant cervical loops [64]. Thus, we hypothesized that longer procedural time and increased case complexity, may result in poorer clinical status and higher complication rates. However, our data rejected that hypothesis, revealing no association between choice of thrombectomy device and recanalization success or 90-day functional outcomes measured by mRS and NIHSS. On the contrary, Prochazka *et al.* showed that patients treated with ADAPT had significantly better recanalization outcomes while patients treated primarily with stent-retriever had significantly better 3-month mRS scores [72]. One study proposed that the use of multiple device types during solitary thrombectomy resulted in significantly low rate of recanalization success [181] while another, retrospective study suggested a strong correlation between increased number of maneuver counts (> 2 maneuvers) and decreased recanalization success [191]. Studies have also suggested other factors besides thrombus composition and choice of thrombectomy device to play a role in failed recanalization attempts including challenging anatomical access, resistant occlusion and procedural complications [192].

While a majority of the patients in whom near-to-complete recanalization (TICI 2b-3) was obtained had mRS scores between 0-2 and NIHSS ≤ 10 (*i.e.* 15 of the 28 patients) compared to those patients in whom recanalization was not obtained, the differences were statistically insignificant. In a meta-analysis performed by Rha *et al.* which combined findings from 33 studies, it was revealed that patients in whom complete recanalization was achieved had 4- to 5-fold improvement in functionality and low fatality outcomes than patients in whom no recanalization was achieved [193]. Although our study showed that 3-month functional outcomes did not significantly depend on thrombus composition, choice of thrombectomy device, or recanalization success, we assume that there are several other factors that could explain why some patients in whom good interventional outcomes were achieved, still had poor functionality.

For instance, in the 4 patients who suffered moderate-to-severe disabilities (mRS > 3 and 90-day NIHSS > 10), successful recanalization (TICI 2c-3) was achieved in 3 of those 4 patients. Likewise, in the 9 patients who died (mRS 6), successful recanalization was achieved in 8 of those 9 patients. This phenomenon where successful recanalization fails to achieve favourable prognostic outcomes, has been defined as futile recanalization [194]. Interestingly, our data suggested that, 8 of the 11 patients who suffered severe disabilities or died despite successful recanalization, had thrombi composed of significantly higher proportions of erythrocytes than fibrin. This finding thereby associated the presence of high proportions of erythrocytes with poor prognostic outcomes despite the fact that high proportions of erythrocytes were also significantly correlated with good recanalization outcomes. Nevertheless, along with histopathological composition of thrombi, there could be several other potential factors contributing to futile recanalization such as:

1) *Delayed reperfusion*. Several different target times for mechanical thrombectomy have been reported to date, including onset-to-treatment, where a study indicated that the odds of good outcomes reduced by 6% for every hour of delay from onset-to-treatment [195], onset-to-reperfusion, where achieving long-term good outcomes after reperfusion were significantly time-dependent [196] whereby, the odds of good outcomes decreased by 12-21% for every 30 min delay from onset-to-reperfusion [197]. Similarly, delayed time between door-to-puncture [198] and imaging-to-puncture [199] also significantly reduced the probabilities for good outcomes;

2) *Occlusion location (i.e. left versus right hemisphere tissue damage)*. A previous study described the mechanistic differences in functionality, severity, mortality and frequency of left- and right-hemisphere strokes. They found that patients with left occlusions had significantly higher pre-admission NIHSS, worse Glasgow coma scale, higher mortality rates and increased

occurrence of mechanical thrombectomy [200]. The severity associated with left hemisphere strokes could be due to that fact that left vessel occlusions affect more modalities, including right hemiplegia (stroke affecting motor cortices), Broca's aphasia (stroke affecting speech production) or Wernicke's aphasia (stroke affecting speech comprehension), facial droop, and memory problems, as opposed to right vessel occlusions where patients are affected mostly by spatial disorientation [201], [202];

3) *Blood pressure.* A small study with a cohort of 378 patients showed that high mean systolic blood pressure post-EVT were associated with poorer mRS scores [203]. This trend was also true for patients that received IVT treatment alone [204];

4) *Age and sex differences.* A study by Hedna *et al.* suggested that patients ≥ 75 years had higher occurrence of mortality than patients < 75 years of age [200]. Likewise, another study revealed patients < 70 years of age to have better mRS scores [205]. As for sex differences, a study by Madsen *et al.* revealed that females were less likely to be independent at 90 days than males [206];

5) *Peri- and post-procedural complication*. Studies have suggested that re-occlusion of the vessel by distal embolization after achieving recanalization of the primary occlusion site contribute to neurologic deterioration [181], [194]. Along with distal embolism, the occurrence of ICH remains one of the prominent complications after successful EVT [62]. A study by Nawabi *et al*. identified lower ASPECTS, low collateral score and high CT-based quantitative net water uptake as statistically significant independent predictors of ICH after successful thrombectomy [207];

6) *Efficacy of combined treatment*. Some researchers believe that rtPA contribute neurotoxic effects by damaging the blood brain barrier and vessels, consequently downregulating cerebral

autoregulation and inducing distal embolization [181], [194]. While some studies have reported that patients administered with IV-tPA prior to thrombectomy required less EVT attempts, had better mRS, higher recanalization success, and lower mortality rates [208]. Thus, with such contradictory findings, the effects of combined treatment on futile recanalization remain controversial. And lastly,

7) *Previously prescribed drugs (anticoagulants and thrombolytics).* A study by Myint *et al.* found that patients who were on prescribed anti-thrombotics prior to their stroke onset, had better long-term outcomes [209]. Likewise, in an observational study of 94,474 patients, they found that patients who were on anticoagulants, warfarin or non-vitamin K dependent antagonists, prior to their stroke onset, had significantly less severe strokes and decreased mortality rates [210].

4.3 Innovative contribution of this study

The novel contribution of this study was the use of synchrotron-based imaging technique and FTIR which were utilized for identifying elemental and biochemical composition of thrombi. To the best of our knowledge, we are the only study to report such findings. Although the elemental and biochemical composition of blood components in normal blood samples have been under investigation for over a century, the exact concentration and distribution of bioelements and organic biomolecules present in blood under pathological conditions such as thrombosis are not well-known.

Previous studies have reported the presence of sodium, potassium, magnesium, zinc, calcium, and copper in normal human red blood cells [211] as well as platelets [212], [213]. However, these studies have utilized basic laboratory-based techniques, including emission spectrophotometry [211], absorption spectroscopy [213] and neutron activation analysis [212], respectively, to report the concentration of these elements. On the contrary, in our study we were

able to not only measure elemental quantities, but also visually illustrate how elements distributed within the tissue sections. The elemental distribution observed in the tissues are a true representation of the elements present in the samples as we ensure tissue thickness consistency, use exact same beamline settings during each beamtime, normalize quantified data by correcting for I_0 flux, normalize fluorescence peak differences and use the same scale to threshold intensities.

For years, researchers have reported distinctive histological patterns formed by fibrin, erythrocytes, platelets and polymorphonuclear cells. However, we are the first to report how elements are distributed and co-localized in fibrin and erythrocyte-rich regions of the thrombus. The XFI distribution maps showed an abundant presence of chlorine, potassium and sulfur within the core as well as the peripheral regions of the thrombi, whereas iron as predicted, was only dispersed in the erythrocyte-rich areas. Calcium on the other hand, had elevated distribution in the fibrinous regions. Calcium is an integral element in the coagulation cascade because it acts as a tissue factor (factor IV) and also plays several important roles including activating other downstream tissue factors, stabilizing factor VIII and linking tenase/prothrombinase complexes [42]. Other elements including copper and zinc also play an important role in the coagulation cascade. Zn is released by platelets to modulate thrombus strength and stability, and potentiate thrombus formation [214]. In cerebral ischemia, generation of significant amounts of free oxygen radicals and their derivatives contribute to oxidative stress and induce brain damage. Therefore, to control oxidative damage, antioxidant enzymes alternatively metabolize oxidative toxic substrates in the presence of cofactors that enhance catalysis. For instance, superoxide dismutase catalyzes the dismutation of superoxide radicals in the presence of Cu and Zn cofactors [215]. Despite the important roles of Cu and Zn, these two elements were only detected at trace levels.

Furthermore, under ischemic conditions, several proteins undergo reversible methionine oxidation to perceive oxidative stress whereby methionine residues are post-transitionally oxidized to methionine sulfoxide [216]. Some of the possible targets of protein methionine oxidation in the coagulation cascade include vWF, factor VII, antithrombin, α_2-antiplasmin and fibrinogen [216]. Distribution maps generated to characterize the presence of different sulfur species revealed copiously dispersion of methionine sulfoxide throughout the thrombi. Additionally, the distribution maps also demonstrated a high presence of sulfonic acid (*i.e.* taurine). Taurine, unlike other amino acids is not utilized in protein synthesis [217] and is found in most of the biological tissues to regulate osmoregulation, anti-inflammation, calcium homeostasis *etc*. [218]. In fact, supplementation of taurine with tPA has shown to improve long-term clinical outcomes, reduce tPA-induced ICH and improve vascular patency [218]. Moreover, studies have shown taurine to stabilize against platelets [219] such that it exerts inhibitory effects on platelet aggregation [217]. This explains why we observed such high taurine distribution in the fibrin-rich areas.

Previous literature has also reported the presence of Mg^{2+} and Na^{+} in blood constituents. In an *in vitro* study, Sekiya *et al.* showed that, in the presence of Mg^{2+}, lower amounts of factor VIII were required to activate factor X than those needed with Ca^{2+} alone. They revealed that Mg^{2+} stabilized factor IX and accelerated all factor IX-dependent activities in the cascade [214]. On the other hand, Na^{+} is crucial for maintaining a hemodynamic balance. Along with being an important electrolyte, Na^{+} has shown to allosterically modulate the activity of thrombin by increasing its proteolytic activity for cleaving prothrombotic substrates [41]. Even though Mg^{2+} and Na^{+} are important elements in the coagulation cascade, it is difficult to detect them using hard-X-ray beamlines because they attenuate before the detector can pick up any photons. Thus,

Mg and Na are imaged on a soft X-ray beamline (BL 6-2) that uses a low incident energy (below 5 keV). Additionally, in order for soft X-ray beamlines to operate ideally and offer high spatial resolution, high energy resolution and high spectral brightness, imaging is performed in a helium or vacuum environment that prevents high attenuation of photons [127]. In this study we also quantified elements and organic biomolecules of interest and retrospectively correlated the concentrations ($\mu g/cm^2$) with TICI and mRS scores. Our study revealed that the elemental and biochemical composition of thrombi did not correlate with the recanalization or 3-month functional outcomes. However, these findings need to be validated further using bulk-analysis and a larger sample size.

Several studies have used thrombus perviousness as a biomarker to predict recanalization and functional outcomes. These studies have revealed that increased thrombus perviousness (measured via contrast agent penetration on CTA and thrombus attenuation on NCCT) resulted in better recanalization rates and improved functional outcomes [220], [221], [222]. We were able to show that the contrast agent (iodine) only penetrated the fibrin-rich areas using the XFI distribution maps. The contrast agent, Isovue-300, is a hydrophilic non-ionic contrast agent that contains 3 iodine atoms and has a molecular weight of 0.777 kDa. Our finding supported the results of a previous study that found thrombi permeable to the contrast agent had low fractions of red blood cells [223]. To date, we are the first to visually illustrate and quantify contrast agent-based thrombus perviousness by combining XFI and thrombus histology, directly using the thrombi samples as opposed to measuring thrombus density. Correlating iodine concentration with stroke etiology, we found no significant correlation between thrombus perviousness and stroke etiology. It is important to note that, the permeability measured and described in this study refers to the amount of contrast agent used during the thrombectomy procedure unlike other

studies that have predicted the outcomes based on the amount of contrast agent used during MRI or CTA imaging prior to thrombectomy. Additionally, we have yet to statistically prove if thrombus perviousness affects clinical and interventional outcomes. To validate correlations between thrombus perviousness and clinical outcomes in future studies, future studies would need to take into account how much and for how long was the contrast agent administered during imaging prior to EVT as well as during the thrombectomy procedure.

Considerable research involving thrombus perviousness, describes the impacts of thrombus permeability on the efficacy of IV-tPA. For instance, one of the studies showed that erythrocyte-rich thrombi allowed tPA penetration through the fibrin networks, consequently resulting in effective thrombolysis compared to that in fibrin-rich thrombi [91]. On the contrary, another study revealed that the presence of erythrocytes provided fibrin with lytic resistance to tPA by downregulating tPA-induced plasminogen activation of the fibrinolytic pathway [224]. A majority of the research has targeted fibrin as a key player for poor clinical outcomes where higher percentage of fibrin has been associated with lower recanalization rates [92], increased EVT failures [94], and increased resistance to plasmin drugs [89, 90]. Retrospective analysis in our study revealed that, the 4 patients who underwent EVT after unsuccessful IV-tPA thrombolysis, had erythrocyte-rich thrombi. Moreover, even though Isovue-300 is a relatively smaller molecule than tPA (0.777 kDA *vs* 70 kDA), our data demonstrated lack of Isovue-300 permeability through the RBC areas of the thrombus, suggesting that erythrocyte-rich thrombi were less permeable than fibrin-rich thrombi. That said, it is important to keep in mind that the iodine concentration in the thrombus is also dependent on other factors. For instance, longer procedural times would naturally result in increased iodine accumulation. Furthermore, during thrombectomy any amount of contrast agent administered intra-arterially would potentially

accumulate more in the thrombus due to blood stagnation. Moreover, since the half-life of iosvue-300 is approximately 2 hours, the amount of contrast agent administered during pre-procedural imaging as well as during the EVT procedure would cumulatively increase the iodine, thereby affecting the iodine distribution in the clotted thrombus.

4.4 Limitations of this study

There were several limitations in this study. For instance, even though all thrombi were histopathologically classified using the same threshold values in ImageJ-based trainable WEKA segmentation plugin, there were certain discrepancies observed from sample to sample stained with Masson's Trichrome, wherein some sections were stained darker than the others. Consequently, this made it difficult for us to identify and highlight lighter stained pixels using consistent intensity parameters. Furthermore, we also had limitations beyond the common ones of a retrospective study design. Sometimes in retrospective studies, challenges of inherent selection bias or misclassification bias can be eliminated with a larger sample size. However, the sample size in this study was relatively small (n = 25) which potentially introduced false positives as well as decreased the validity and statistical power for correlations where a trend was observed but statistical significance was not reached.

Another limitation of this study was the lack of histopathological analysis on frozen sections. We were eager to correlate XFI distribution patterns with cellular morphology on serially collected frozen sections. However, we could not achieve good histological results on frozen sections and therefore, elemental and histological correlations were derived from frozen and paraffin sections, respectively even though the sections belonged to different fragments of the same thrombus. Moreover, patterns and ratios of histological components changed from distal to the proximal end of the thrombus. This weakened the categorization of thrombi due to the lack of total

thrombus analysis in this study. Overcoming this issue in the future would require inclusion of inductively coupled plasma mass spectrometry (ICPMS)-based bulk spectroscopy.

Conclusions and Future Direction

In conclusion, we were able to show that thrombus composition was not affected by etiology. Additionally, thrombus composition did not affect stroke severity, choice of thrombectomy device, recanalization outcomes or three-month functional outcomes. Importantly, our results refuted the traditional paradigm of classifying a thrombus as red and white. To further our insights into thrombus composition, we used advanced imaging techniques, XFI and FTIR, to evaluate distribution patterns for biological elements and biomolecules. However, even these powerful techniques revealed no significant findings in elemental and biochemical composition of thrombi and their effects on interventional and clinical parameters. An interesting finding worth exploring in the future is the correlation between thrombus perviousness, etiology and thrombus composition which suggested that erythrocyte-rich thrombi are less pervious than fibrin rich thrombi. To date, a majority of the research has targeted fibrin as a key player in poor prognostic outcomes, however, our combined histology and XFI data reveals erythrocytes to be the new potential target for poor prognostic outcomes and ineffectiveness of tPA.

Future direction could elaborate certain aspects of this study and include a larger cohort. Correlation of puncture-to-reperfusion time with thrombus composition to determine whether a specific type of thrombus increases procedural time and worsen outcomes may be worthwhile. In the second phase of this study, we would like to combine X-ray mass attenuation coefficients of each biological element with thrombus density measured on CTA and certain parameters from patients' blood work to further our insights on classifying thrombi on CTA using elemental information instead of histological biomarkers. And lastly, to avoid selection biases in FTIR

analysis, we would include K-mean clustering to quantify the presence of biomolecules in the entire tissue section rather than using concentration values from selected ROIs.

References

1. Martini, F.H., M.J. Timmons, and R.B. Tallitsch, *Human Anatomy, Books a La Carte Edition*. 2014: Benjamin-Cummings Publishing Company.
2. Xing, C.Y., et al., *Distribution of cardiac output to the brain across the adult lifespan.* J Cereb Blood Flow Metab, 2017. **37**(8): p. 2848-2856.
3. Williams, L.R. and R.W. Leggett, *Reference values for resting blood flow to organs of man.* Clin Phys Physiol Meas, 1989. **10**(3): p. 187-217.
4. Mergenthaler, P., et al., *Sugar for the brain: the role of glucose in physiological and pathological brain function.* Trends Neurosci, 2013. **36**(10): p. 587-97.
5. Tucker, W.D. and K. Mahajan, *Anatomy, Blood Vessels*, in *StatPearls*. 2019, StatPearls Publishing LLC.: Treasure Island (FL).
6. Blumenfeld, H., *Neuroanatomy Through Clinical Cases*. 2010: Sinauer Associates.
7. Ravensbergen, J., Krijger, J. K. B., Hillen, B and Hoogstraten, H.W, *Merging flows in an arterial confluence: the vertebro-basilar junction.* Journal of Fluid Mechanics 1995. **304**: p. 119-141.
8. Konan, L.M. and F.B. Mesfin, *Neuroanatomy, Cerebral Blood Supply*, in *StatPearls*. 2019, StatPearls Publishing LLC.: Treasure Island (FL).
9. Vrselja, Z., et al., *Function of circle of Willis.* J Cereb Blood Flow Metab, 2014. **34**(4): p. 578-84.
10. Caceres, J.A. and J.N. Goldstein, *Intracranial hemorrhage.* Emerg Med Clin North Am, 2012. **30**(3): p. 771-94.
11. Sutherland, G.R. and R.N. Auer, *Primary intracerebral hemorrhage.* J Clin Neurosci, 2006. **13**(5): p. 511-7.
12. Gravanis, I. and S.E. Tsirka, *Tissue-type plasminogen activator as a therapeutic target in stroke.* Expert Opin Ther Targets, 2008. **12**(2): p. 159-70.
13. Kang, D.H. and J. Park, *Endovascular Stroke Therapy Focused on Stent Retriever Thrombectomy and Direct Clot Aspiration: Historical Review and Modern Application.* J Korean Neurosurg Soc, 2017. **60**(3): p. 335-347.
14. Ovbiagele, B. and M.N. Nguyen-Huynh, *Stroke epidemiology: advancing our understanding of disease mechanism and therapy.* Neurotherapeutics, 2011. **8**(3): p. 319-29.
15. Jorgensen, H.S., et al., *Intracerebral hemorrhage versus infarction: stroke severity, risk factors, and prognosis.* Ann Neurol, 1995. **38**(1): p. 45-50.
16. Andersen, K.K., et al., *Hemorrhagic and ischemic strokes compared: stroke severity, mortality, and risk factors.* Stroke, 2009. **40**(6): p. 2068-72.
17. Krueger, H., et al., *Prevalence of Individuals Experiencing the Effects of Stroke in Canada: Trends and Projections.* Stroke, 2015. **46**(8): p. 2226-31.
18. Benjamin, E.J., et al., *Heart Disease and Stroke Statistics-2019 Update: A Report From the American Heart Association.* Circulation, 2019. **139**(10): p. e56-e528.
19. O'Donnell, M.J., et al., *Risk factors for ischaemic and intracerebral haemorrhagic stroke in 22 countries (the INTERSTROKE study): a case-control study.* Lancet, 2010. **376**(9735): p. 112-23.
20. Adams, H.P., Jr., et al., *Classification of subtype of acute ischemic stroke. Definitions for use in a multicenter clinical trial. TOAST. Trial of Org 10172 in Acute Stroke Treatment.* Stroke, 1993. **24**(1): p. 35-41.

21. Kolominsky-Rabas, P.L., et al., *Epidemiology of ischemic stroke subtypes according to TOAST criteria: incidence, recurrence, and long-term survival in ischemic stroke subtypes: a population-based study.* Stroke, 2001. **32**(12): p. 2735-40.
22. Caplan, L.R., *Atrial Fibrillation, Past and Future: From a Stroke Non-Entity to an Over-Targeted Cause.* Cerebrovasc Dis, 2018. **45**(3-4): p. 149-153.
23. Insull, W., Jr., *The pathology of atherosclerosis: plaque development and plaque responses to medical treatment.* Am J Med, 2009. **122**(1 Suppl): p. S3-s14.
24. Murtagh, B. and R.W. Smalling, *Cardioembolic stroke.* Curr Atheroscler Rep, 2006. **8**(4): p. 310-6.
25. Arboix, A. and J. Alio, *Cardioembolic stroke: clinical features, specific cardiac disorders and prognosis.* Curr Cardiol Rev, 2010. **6**(3): p. 150-61.
26. *Global, regional, and national burden of stroke, 1990-2016: a systematic analysis for the Global Burden of Disease Study 2016.* Lancet Neurol, 2019. **18**(5): p. 439-458.
27. Yang, Y., et al., *The Disability Rate of 5-Year Post-Stroke and Its Correlation Factors: A National Survey in China.* PLoS One, 2016. **11**(11): p. e0165341.
28. Kumar, D.R., et al., *Virchow's contribution to the understanding of thrombosis and cellular biology.* Clin Med Res, 2010. **8**(3-4): p. 168-72.
29. Bagot, C.N. and R. Arya, *Virchow and his triad: a question of attribution.* Br J Haematol, 2008. **143**(2): p. 180-90.
30. Jerjes-Sanchez, C., *Venous and arterial thrombosis: a continuous spectrum of the same disease?* Eur Heart J, 2005. **26**(1): p. 3-4.
31. Palta, S., R. Saroa, and A. Palta, *Overview of the coagulation system.* Indian J Anaesth, 2014. **58**(5): p. 515-23.
32. Gale, A.J., *Continuing education course #2: current understanding of hemostasis.* Toxicol Pathol, 2011. **39**(1): p. 273-80.
33. Thon, J.N. and J.E. Italiano, *Platelet formation.* Semin Hematol, 2010. **47**(3): p. 220-6.
34. Ribatti, D. and E. Crivellato, *Giulio Bizzozero and the discovery of platelets.* Leuk Res, 2007. **31**(10): p. 1339-41.
35. Ruggeri, Z.M.a.J., Shaun P, *Platelet Thrombus Formation in Flowing Blood*. 3rd ed. Platelets. 2013, Cambridge, USA: Academic Press.
36. Lam, F.W., K.V. Vijayan, and R.E. Rumbaut, *Platelets and Their Interactions with Other Immune Cells.* Compr Physiol, 2015. **5**(3): p. 1265-80.
37. Kahr, W.H., *Granules and thrombus formation.* Blood, 2009. **114**(5): p. 932-3.
38. Whiteheart, S.W., *Platelet granules: surprise packages.* Blood, 2011. **118**(5): p. 1190-1.
39. Kumar, V., et al., *Robbins & Cotran Pathologic Basis of Disease E-Book*. 2009: Elsevier Health Sciences.
40. Koupenova, M., et al., *Circulating Platelets as Mediators of Immunity, Inflammation, and Thrombosis.* Circ Res, 2018. **122**(2): p. 337-351.
41. Huntington, J.A., *How Na+ activates thrombin--a review of the functional and structural data.* Biol Chem, 2008. **389**(8): p. 1025-35.
42. Sibinga, C.T.S., P.C. Das, and P.M. Mannucci, *Coagulation and Blood Transfusion: Proceedings of the Fifteenth Annual Symposium on Blood Transfusion, Groningen 1990, organized by the Red Cross Blood Bank Groningen-Drenthe*. 2012: Springer US.
43. Dong, J., et al., *Diagnostic implication of fibrin degradation products and D-dimer in aortic dissection.* Sci Rep, 2017. **7**: p. 43957.
44. Hepner, M. and V. Karlaftis, *Antithrombin.* Methods Mol Biol, 2013. **992**: p. 355-64.

45. Bansal, S., K.S. Sangha, and P. Khatri, *Drug treatment of acute ischemic stroke.* Am J Cardiovasc Drugs, 2013. **13**(1): p. 57-69.
46. Mekaj, Y.H., et al., *New oral anticoagulants: their advantages and disadvantages compared with vitamin K antagonists in the prevention and treatment of patients with thromboembolic events.* Ther Clin Risk Manag, 2015. **11**: p. 967-77.
47. Zivin, J.A., *Acute stroke therapy with tissue plasminogen activator (tPA) since it was approved by the U.S. Food and Drug Administration (FDA).* Ann Neurol, 2009. **66**(1): p. 6-10.
48. Pena, C., et al., *Update to Food and Drug Administration Regulation of Stroke Neurological Devices.* Stroke, 2019. **50**(2): p. 524-528.
49. Cheng, N.T. and A.S. Kim, *Intravenous Thrombolysis for Acute Ischemic Stroke Within 3 Hours Versus Between 3 and 4.5 Hours of Symptom Onset.* Neurohospitalist, 2015. **5**(3): p. 101-9.
50. Hacke, W., et al., *Thrombolysis with alteplase 3 to 4.5 hours after acute ischemic stroke.* N Engl J Med, 2008. **359**(13): p. 1317-29.
51. Fugate, J.E. and A.A. Rabinstein, *Absolute and Relative Contraindications to IV rt-PA for Acute Ischemic Stroke.* Neurohospitalist, 2015. **5**(3): p. 110-21.
52. Nadeau, J.O., et al., *TPA use for stroke in the Registry of the Canadian Stroke Network.* Can J Neurol Sci, 2005. **32**(4): p. 433-9.
53. Yip, T.R. and B.M. Demaerschalk, *Estimated cost savings of increased use of intravenous tissue plasminogen activator for acute ischemic stroke in Canada.* Stroke, 2007. **38**(6): p. 1952-5.
54. Castano, C., et al., *Mechanical thrombectomy with 'ADAPT' technique by transcervical access in acute ischemic stroke.* Neuroradiol J, 2015. **28**(6): p. 617-22.
55. O'Carroll, C.B., M.N. Rubin, and B.W. Chong, *What is the Role for Intra-Arterial Therapy in Acute Stroke Intervention?* Neurohospitalist, 2015. **5**(3): p. 122-32.
56. Nogueira, R.G., L.H. Schwamm, and J.A. Hirsch, *Endovascular approaches to acute stroke, part 1: Drugs, devices, and data.* AJNR Am J Neuroradiol, 2009. **30**(4): p. 649-61.
57. Smith, W.S. and A.J. Furlan, *Brief History of Endovascular Acute Ischemic Stroke Treatment.* Stroke, 2016. **47**(2): p. e23-6.
58. Riedel, C.H., et al., *The importance of size: successful recanalization by intravenous thrombolysis in acute anterior stroke depends on thrombus length.* Stroke, 2011. **42**(6): p. 1775-7.
59. Evans, M.R.B., et al., *Revolution in acute ischaemic stroke care: a practical guide to mechanical thrombectomy.* Pract Neurol, 2017. **17**(4): p. 252-265.
60. Jovin, T.G., et al., *Thrombectomy within 8 hours after symptom onset in ischemic stroke.* N Engl J Med, 2015. **372**(24): p. 2296-306.
61. Goyal, M., et al., *Endovascular Therapy in Acute Ischemic Stroke: Challenges and Transition From Trials to Bedside.* Stroke, 2016. **47**(2): p. 548-53.
62. Goyal, M., et al., *Endovascular thrombectomy after large-vessel ischaemic stroke: a meta-analysis of individual patient data from five randomised trials.* Lancet, 2016. **387**(10029): p. 1723-31.
63. Furlan, A., et al., *Intra-arterial prourokinase for acute ischemic stroke. The PROACT II study: a randomized controlled trial. Prolyse in Acute Cerebral Thromboembolism.* Jama, 1999. **282**(21): p. 2003-11.

64. Pierot, L., et al., *Techniques for endovascular treatment of acute ischemic stroke: from intra-arterial fibrinolytics to stent-retrievers.* Stroke, 2015. **46**(3): p. 909-14.
65. Broderick, J.a.T., T, *The IMS Trials: How a combined IV and IA approach utilizing an ultrasound-assisted, drug-delivery microcatheter increases recanalization rates over IV thrombolytic therapy alone.* Endovascular Today, 2006.
66. Boyle, K., Joundi, Raed A and Aviv, Richard I, *An historical and contemporary review of endovascular therapy for acute ischemic stroke.* Neurovascular Imaging 2017. **3**(1): p. 1-12.
67. Broderick, J.P. and G. Schroth, *What the SWIFT and TREVO II trials tell us about the role of endovascular therapy for acute stroke.* Stroke, 2013. **44**(6): p. 1761-4.
68. Kidwell, C.S., et al., *A trial of imaging selection and endovascular treatment for ischemic stroke.* N Engl J Med, 2013. **368**(10): p. 914-23.
69. Ciccone, A., et al., *Endovascular treatment for acute ischemic stroke.* N Engl J Med, 2013. **368**(10): p. 904-13.
70. Qureshi, A.I., et al., *Endovascular Treatment versus Best Medical Treatment in Patients with Acute Ischemic Stroke: A Meta-Analysis of Randomized Controlled Trials.* AJNR Am J Neuroradiol, 2016. **37**(6): p. 1068-73.
71. Turk, A.S., et al., *Comparison of endovascular treatment approaches for acute ischemic stroke: cost effectiveness, technical success, and clinical outcomes.* J Neurointerv Surg, 2015. **7**(9): p. 666-70.
72. Prochazka, V., et al., *Comparison of Mechanical Thrombectomy with Contact Aspiration, Stent Retriever, and Combined Procedures in Patients with Large-Vessel Occlusion in Acute Ischemic Stroke.* Med Sci Monit, 2018. **24**: p. 9342-9353.
73. Berkhemer, O.A., et al., *A randomized trial of intraarterial treatment for acute ischemic stroke.* N Engl J Med, 2015. **372**(1): p. 11-20.
74. Goyal, M., et al., *Randomized assessment of rapid endovascular treatment of ischemic stroke.* N Engl J Med, 2015. **372**(11): p. 1019-30.
75. Campbell, B.C., et al., *Endovascular therapy for ischemic stroke with perfusion-imaging selection.* N Engl J Med, 2015. **372**(11): p. 1009-18.
76. Saver, J.L., et al., *Stent-retriever thrombectomy after intravenous t-PA vs. t-PA alone in stroke.* N Engl J Med, 2015. **372**(24): p. 2285-95.
77. Nogueira, R.G., et al., *Thrombectomy 6 to 24 Hours after Stroke with a Mismatch between Deficit and Infarct.* N Engl J Med, 2018. **378**(1): p. 11-21.
78. Fan, L., et al., *Endovascular Therapy Demonstrates Benefit over Intravenous Recombinant Tissue Plasminogen Activator Based on Repeatedly Measured National Institutes of Health Stroke Scale.* Interv Neurol, 2017. **6**(1-2): p. 25-30.
79. Raychev, R. and J.L. Saver, *Mechanical thrombectomy devices for treatment of stroke.* Neurol Clin Pract, 2012. **2**(3): p. 231-235.
80. Saver, J.L., *Time is brain--quantified.* Stroke, 2006. **37**(1): p. 263-6.
81. Minnerup, J. and C. Kleinschnitz, *Visualization of clot composition in ischemic stroke: do we get what we see?* Stroke, 2011. **42**(5): p. 1193-4.
82. Hann, S., et al., *Comparison of neurologic and radiographic outcomes with Solitaire versus Merci/Penumbra systems for acute stroke intervention.* Biomed Res Int, 2013. **2013**: p. 715170.
83. Tennuci, C., et al., *Comparison of the Effectiveness of Three Methods of Recanalization in a Model of the Middle Cerebral Artery: Thrombus Aspiration via a 4F Catheter,*

Thrombus Aspiration via the GP Thromboaspiration Device, and Mechanical Thrombectomy Using the Solitaire Thrombectomy Device. Stroke Res Treat, 2011. **2011**: p. 186424.
84. Torvik, A.a.J., L., *Thrombotic and Embolic Occlusions of the Carotid Arteries in an Autopsy Material Part 1. Prevalence, Location and Associated Diseases.* Journal of the Neurological Sciences, 1964. **1**(1): p. 24-39.
85. Marder, V.J., et al., *Analysis of thrombi retrieved from cerebral arteries of patients with acute ischemic stroke.* Stroke, 2006. **37**(8): p. 2086-93.
86. Almekhlafi, M.A., et al., *Calcification and endothelialization of thrombi in acute stroke.* Ann Neurol, 2008. **64**(3): p. 344-8.
87. Schuhmann, M.K., et al., *Immunohistochemical Analysis of Cerebral Thrombi Retrieved by Mechanical Thrombectomy from Patients with Acute Ischemic Stroke.* Int J Mol Sci, 2016. **17**(3): p. 298.
88. Fineschi, V., et al., *Histological age determination of venous thrombosis: a neglected forensic task in fatal pulmonary thrombo-embolism.* Forensic Sci Int, 2009. **186**(1-3): p. 22-8.
89. Bach, N., et al., *Study on the effect of streptokinase-activated plasmin (fibrinolysin) on clots in various stages of organization.* J Clin Invest, 1958. **37**(6): p. 864-71.
90. Kirchhof, K., et al., *[Does the result of thrombolysis with recombinant tissue-type plasminogen activator (rt-PA) in rabbits depend on the erythrocyte- and fibrin-content of a thrombus?]*. Rofo, 2004. **176**(1): p. 98-105.
91. Choi, M.H., et al., *Erythrocyte Fraction Within Retrieved Thrombi Contributes to Thrombolytic Response in Acute Ischemic Stroke.* Stroke, 2018. **49**(3): p. 652-659.
92. Yuki, I., et al., *The impact of thromboemboli histology on the performance of a mechanical thrombectomy device.* AJNR Am J Neuroradiol, 2012. **33**(4): p. 643-8.
93. Nogueira, R.G., et al., *The Trevo device: preclinical data of a novel stroke thrombectomy device in two different animal models of arterial thrombo-occlusive disease.* J Neurointerv Surg, 2012. **4**(4): p. 295-300.
94. Kim, B.M., *Causes and Solutions of Endovascular Treatment Failure.* J Stroke, 2017. **19**(2): p. 131-142.
95. Maekawa, K., et al., *Erythrocyte-Rich Thrombus Is Associated with Reduced Number of Maneuvers and Procedure Time in Patients with Acute Ischemic Stroke Undergoing Mechanical Thrombectomy*. Cerebrovasc Dis Extra, 2018. **8**(1): p. 39-49.
96. Srinivasan, M., D. Sedmak, and S. Jewell, *Effect of fixatives and tissue processing on the content and integrity of nucleic acids.* Am J Pathol, 2002. **161**(6): p. 1961-71.
97. Bakhach, J., *The cryopreservation of composite tissues: Principles and recent advancement on cryopreservation of different type of tissues.* Organogenesis, 2009. **5**(3): p. 119-26.
98. Cunningham, M.a.B.-N., Kimberly J. *Freezing Biological Samples*. 2019; Available from: https://www.leicabiosystems.com/pathologyleaders/freezing-biological-samples/.
99. Jang, T.H., et al., *Cryopreservation and its clinical applications.* Integr Med Res, 2017. **6**(1): p. 12-18.
100. Compound, T.-T.O.C.T.O.C.T., *MSDS No. 0000582-03*, S. Finetek, Editor. 2008: California, USA.
101. Culling, C.F.A., R.T. Allison, and W.T. Barr, *Cellular Pathology Technique*. 2014: Elsevier Science.

102. Kiernan, J., *Formaldehyde, Formalin, Paraformaldehyde And Glutaraldehyde: What They Are And What They Do.* Microscopy Today, 2000. **8**(1): p. 8-13.
103. Sompuram, S.R., et al., *A molecular mechanism of formalin fixation and antigen retrieval.* Am J Clin Pathol, 2004. **121**(2): p. 190-9.
104. Clark, G., F.H. Kasten, and H.J. Conn, *History of staining*. 1983: Williams & Wilkins.
105. Titford, M., *Progress in the Development of Microscopical Techniques for Diagnostic Pathology* Journal of Histotechnology, 2009. **32**(1): p. 9-19.
106. Winkelmann, A., *Wilhelm von Waldeyer-Hartz (1836-1921): an anatomist who left his mark.* Clin Anat, 2007. **20**(3): p. 231-4.
107. Myers, R. *The Basic Chemistry of Hematoxylin*. 2019; Available from: https://www.leicabiosystems.com/pathologyleaders/the-basic-chemistry-of-hematoxylin/.
108. Renshaw, S. 4th ed. 2013, Netherlands: Elsevier Science.
109. Wittekind, D., *Traditional staining for routine diagnostic pathology including the role of tannic acid. 1. Value and limitations of the hematoxylin-eosin stain.* Biotechnic & Histochemistry, 2003. **78**(5): p. 261-270.
110. Flint, M.H., Lyons, Mary F, Meaney M.F, and Williams, D.E, *The Masson staining of collagen - an explanation of an apparent paradox.* Histochemical Journal, 1975. **7**(6): p. 529-546.
111. Bancroft, J.D. and M. Gamble, *Theory and Practice of Histological Techniques*. 2008: Churchill Livingstone.
112. Shariff, S.a.K., Amrit Kaur, *Principles & Interpretation of Laboratory Practices in Surgical Pathology*. 2016, Delhi, India: Jaypee Brothers Medical Publishers.
113. Lipman, N.S., et al., *Monoclonal versus polyclonal antibodies: distinguishing characteristics, applications, and information resources.* Ilar j, 2005. **46**(3): p. 258-68.
114. Bishop, D.P., et al., *A guide to integrating immunohistochemistry and chemical imaging.* Chem Soc Rev, 2018. **47**(11): p. 3770-3787.
115. Kim, S.W., J. Roh, and C.S. Park, *Immunohistochemistry for Pathologists: Protocols, Pitfalls, and Tips.* J Pathol Transl Med, 2016. **50**(6): p. 411-418.
116. Chen, X., D.B. Cho, and P.C. Yang, *Double staining immunohistochemistry.* N Am J Med Sci, 2010. **2**(5): p. 241-5.
117. K, R.V., D. Jones, and V. Udupa, *A simple and effective heat induced antigen retrieval method.* MethodsX, 2016. **3**: p. 315-9.
118. Ramos-Vara, J.A., *Technical aspects of immunohistochemistry.* Vet Pathol, 2005. **42**(4): p. 405-26.
119. Fung, K.M., et al., *A novel modification of the avidin-biotin complex method for immunohistochemical studies of transgenic mice with murine monoclonal antibodies.* J Histochem Cytochem, 1992. **40**(9): p. 1319-28.
120. Matos, L.L., et al., *Immunohistochemistry as an important tool in biomarkers detection and clinical practice.* Biomark Insights, 2010. **5**: p. 9-20.
121. Nakane, P.K. and G.B. Pierce, Jr., *Enzyme-labeled antibodies: preparation and application for the localization of antigens.* J Histochem Cytochem, 1966. **14**(12): p. 929-31.
122. Sternberger, L.A., et al., *The unlabeled antibody enzyme method of immunohistochemistry: preparation and properties of soluble antigen-antibody complex (horseradish peroxidase-antihorseradish peroxidase) and its use in identification of spirochetes.* J Histochem Cytochem, 1970. **18**(5): p. 315-33.

123. Manickavasagan, A. and H. Jayasuriya, *Imaging with Electromagnetic Spectrum: Applications in Food and Agriculture*. 2014: Springer Berlin Heidelberg.
124. Willmott, P., *An Introduction to Synchrotron Radiation: Techniques and Applications*. 2011: Wiley.
125. Russo, P., *Handbook of X-ray Imaging: Physics and Technology*. 2017: CRC Press.
126. Verma, H.R., *Atomic and Nuclear Analytical Methods: XRF, Mössbauer, XPS, NAA and Ion-Beam Spectroscopic Techniques*. 2007: Springer Berlin Heidelberg.
127. Pushie, M.J., et al., *Elemental and chemically specific X-ray fluorescence imaging of biological systems.* Chem Rev, 2014. **114**(17): p. 8499-541.
128. Morishige, A.E., Laine, Hannu S, Looney, Erin E, Jensen, Mallory A, Vogt, S, Li, Joel B, Lai, Barry, Savin, Hele, and Tonio, Buonassisi *Increased Throughput and Sensitivity of Synchrotron-Based Characterization for Photovoltaic Materials.* IEEE Journal of Photovoltaics, 2017. **7**: p. 763-771.
129. Suvarna, K.S., C. Layton, and J.D. Bancroft, *Bancroft's Theory and Practice of Histological Techniques E-Book*. 2018: Elsevier Health Sciences.
130. Kopittke, P.M., et al., *Synchrotron-Based X-Ray Fluorescence Microscopy as a Technique for Imaging of Elements in Plants.* Plant Physiol, 2018. **178**(2): p. 507-523.
131. Ortega, R., et al., *X-ray absorption spectroscopy of biological samples. A tutorial.* Journal of Analytical Atomic Spectrometry, 2012. **27**(12): p. 2054-2065.
132. van Bokhoven, J.A. and C. Lamberti, *X-Ray Absorption and X-Ray Emission Spectroscopy: Theory and Applications*. 2016: Wiley.
133. Teo, B.K. and D.C. Joy, *EXAFS Spectroscopy: Techniques and Applications*. 2013: Springer US.
134. Brown, G.E.a.W., G.A. *X-ray Absorption Spectroscopy: Introduction to Experimental Procedures*. 2004; Available from: https://www-ssrl.slac.stanford.edu/mes/xafs/xas_intro.html.
135. Smith, B.C., *Fundamentals of Fourier Transform Infrared Spectroscopy*. 1995: Taylor & Francis.
136. Harris, D.C.a.B., Michael D, *Symmetry and Spectroscopy: An Introduction to Vibrational and Electronic Spectroscopy* 1978, New York, USA: Dover Publications. 550.
137. Ushasree, U., Jaleeli, KA and Ahmad A *A Study on Infrared Spectroscopy of Human Blood.* International Journal of Sciene, Environment and Technology 2016. **5**(3): p. 1189-1192.
138. Miller, L.M.a.S., Randy J, *Synchrotrons versus globars, point-detectors versus focal plane arrays: Selecting the best source and detector for specific infrared microspectroscopy and imaging applications.* Vibrational Spectroscopy 2005. **38**(1-2): p. 237-240.
139. McNaughton, D., *Synchrotron Infrared Spectroscopy in Biology and Biochemistry.* Australian Biochemist, 2005. **36**(1): p. 55-58.
140. Harrison, J.K., K.S. McArthur, and T.J. Quinn, *Assessment scales in stroke: clinimetric and clinical considerations.* Clin Interv Aging, 2013. **8**: p. 201-11.
141. Fischer, U., et al., *NIHSS score and arteriographic findings in acute ischemic stroke.* Stroke, 2005. **36**(10): p. 2121-5.
142. Mihindu, E., et al., *Patients with moderate to severe strokes (NIHSS score >10) undergoing urgent carotid interventions within 48 hours have worse functional outcomes.* J Vasc Surg, 2019. **69**(5): p. 1471-1481.

143. Barber, P.A., et al., *Validity and reliability of a quantitative computed tomography score in predicting outcome of hyperacute stroke before thrombolytic therapy. ASPECTS Study Group. Alberta Stroke Programme Early CT Score.* Lancet, 2000. **355**(9216): p. 1670-4.
144. Gaillard, F.a.S., Haris. *Alberta stroke program early CT score (ASPECTS).* 2019; Available from: https://radiopaedia.org/articles/alberta-stroke-program-early-ct-score-aspects-1.
145. Molina, C.A., et al., *REVASCAT: a randomized trial of revascularization with SOLITAIRE FR device vs. best medical therapy in the treatment of acute stroke due to anterior circulation large vessel occlusion presenting within eight-hours of symptom onset.* Int J Stroke, 2015. **10**(4): p. 619-26.
146. Fugate, J.E., A.M. Klunder, and D.F. Kallmes, *What is meant by "TICI"?* AJNR Am J Neuroradiol, 2013. **34**(9): p. 1792-7.
147. Spiotta, A.M., Fargen, K.M., Chaudry, I, Turner, R.D. and Turk, A.S, *ADAPT: A Direct Aspiration First Pass Technique.* Endovascular Today, 2016. **15**(2): p. 68-70.
148. Rolls, G. *An Introduction to Specimen Processing*. 2019; Available from: https://www.leicabiosystems.com/pathologyleaders/an-introduction-to-specimen-processing/.
149. Pushie, M.J., et al., *Revealing the Penumbra through Imaging Elemental Markers of Cellular Metabolism in an Ischemic Stroke Model.* ACS Chem Neurosci, 2018. **9**(5): p. 886-893.
150. Hackett, M.J., et al., *Imaging Taurine in the Central Nervous System Using Chemically Specific X-ray Fluorescence Imaging at the Sulfur K-Edge.* Anal Chem, 2016. **88**(22): p. 10916-10924.
151. George, G.N., et al., *X-ray-induced photo-chemistry and X-ray absorption spectroscopy of biological samples.* J Synchrotron Radiat, 2012. **19**(Pt 6): p. 875-86.
152. Hackett, M.J., et al., *Concurrent Glycogen and Lactate Imaging with FTIR Spectroscopy To Spatially Localize Metabolic Parameters of the Glial Response Following Brain Ischemia.* Anal Chem, 2016. **88**(22): p. 10949-10956.
153. Omair, A., *Selecting the appropriate study design for your research: Descriptive study designs.* Journal of Health Specialties, 2015. **3**(3): p. 153-156.
154. Song, J.W. and K.C. Chung, *Observational studies: cohort and case-control studies.* Plast Reconstr Surg, 2010. **126**(6): p. 2234-42.
155. Mircioiu, C. and J. Atkinson, *A Comparison of Parametric and Non-Parametric Methods Applied to a Likert Scale.* Pharmacy (Basel), 2017. **5**(2).
156. Winters, R., A. Winters, and R.G. Amedee, *Statistics: a brief overview.* Ochsner J, 2010. **10**(3): p. 213-6.
157. Hopkins, S., J.R. Dettori, and J.R. Chapman, *Parametric and Nonparametric Tests in Spine Research: Why Do They Matter?* Global Spine J, 2018. **8**(6): p. 652-654.
158. Parab, S. and S. Bhalerao, *Choosing statistical test.* Int J Ayurveda Res, 2010. **1**(3): p. 187-91.
159. Hoekstra, R., H.A. Kiers, and A. Johnson, *Are assumptions of well-known statistical techniques checked, and why (not)?* Front Psychol, 2012. **3**: p. 137.
160. Kitchen, C.M., *Nonparametric vs parametric tests of location in biomedical research.* Am J Ophthalmol, 2009. **147**(4): p. 571-2.
161. Chin, R.a.L., B.Y., *Principles and Practice of Clinical Trial Medicine: Chapter 15-Analysis of Data* Cambridge, USA: Academic Press.

162. Liebeskind, D.S., et al., *CT and MRI early vessel signs reflect clot composition in acute stroke.* Stroke, 2011. **42**(5): p. 1237-43.
163. Shin, J.W., et al., *High red blood cell composition in clots is associated with successful recanalization during intra-arterial thrombectomy.* PLoS One, 2018. **13**(5): p. e0197492.
164. Wilson, S.A., et al., *X-ray absorption spectroscopic investigation of the electronic structure differences in solution and crystalline oxyhemoglobin.* Proc Natl Acad Sci U S A, 2013. **110**(41): p. 16333-8.
165. Alves, H.C., et al., *Associations Between Collateral Status and Thrombus Characteristics and Their Impact in Anterior Circulation Stroke.* Stroke, 2018. **49**(2): p. 391-396.
166. L, T.A.a.J., *Thrombotic and Embolic Occlusions of the Carotid Arteries in an Autopsy Series Part 2. Cerebral Lesions and Clinical Course.* Journal of the Neurological Sciences, 1966. **3**(4): p. 410-432.
167. Jorgensen, L., *EXPERIMENTAL PLATELET AND COAGULATION THROMBI. A HISTOLOGICAL STUDY OF ARTERIAL AND VENOUS THROMBI OF VARYING AGE IN UNTREATED AND HEPARINIZED RABBITS.* Acta Pathol Microbiol Scand, 1964. **62**: p. 189-223.
168. Singh, P., R. Kaur, and A. Kaur, *Clot composition and treatment approach to acute ischemic stroke: The road so far.* Ann Indian Acad Neurol, 2013. **16**(4): p. 494-7.
169. Chaves, C.J. and L.R. Caplan, *Heparin and oral anticoagulants in the treatment of brain ischemia.* J Neurol Sci, 2000. **173**(1): p. 3-9.
170. Simons, N., et al., *Thrombus composition in acute ischemic stroke: a histopathological study of thrombus extracted by endovascular retrieval.* J Neuroradiol, 2015. **42**(2): p. 86-92.
171. Ahn, S.H., et al., *Histologic features of acute thrombi retrieved from stroke patients during mechanical reperfusion therapy.* Int J Stroke, 2016. **11**(9): p. 1036-1044.
172. Brinjikji, W., et al., *Correlation of imaging and histopathology of thrombi in acute ischemic stroke with etiology and outcome: a systematic review.* J Neurointerv Surg, 2017. **9**(6): p. 529-534.
173. Niesten, J.M., et al., *Histopathologic composition of cerebral thrombi of acute stroke patients is correlated with stroke subtype and thrombus attenuation.* PLoS One, 2014. **9**(2): p. e88882.
174. Kim, S.K., et al., *Histologic Analysis of Retrieved Clots in Acute Ischemic Stroke: Correlation with Stroke Etiology and Gradient-Echo MRI.* AJNR Am J Neuroradiol, 2015. **36**(9): p. 1756-62.
175. Tomsick, T.A., et al., *Hyperdense middle cerebral artery: incidence and quantitative significance.* Neuroradiology, 1989. **31**(4): p. 312-5.
176. Moftakhar, P., et al., *Density of thrombus on admission CT predicts revascularization efficacy in large vessel occlusion acute ischemic stroke.* Stroke, 2013. **44**(1): p. 243-5.
177. Fitzgerald, S.T., et al., *Platelet-rich clots as identified by Martius Scarlet Blue staining are isodense on NCCT.* J Neurointerv Surg, 2019.
178. Dobrocky, T., et al., *Thrombectomy of calcified emboli in stroke. Does histology of thrombi influence the effectiveness of thrombectomy?* J Neurointerv Surg, 2018. **10**(4): p. 345-350.
179. Sporns, P.B., et al., *Ischemic Stroke: What Does the Histological Composition Tell Us About the Origin of the Thrombus?* Stroke, 2017. **48**(8): p. 2206-2210.

180. Gratz, P.P., et al., *Whole-Brain Susceptibility-Weighted Thrombus Imaging in Stroke: Fragmented Thrombi Predict Worse Outcome.* AJNR Am J Neuroradiol, 2015. **36**(7): p. 1277-82.
181. Kaesmacher, J., et al., *Risk of Thrombus Fragmentation during Endovascular Stroke Treatment.* AJNR Am J Neuroradiol, 2017. **38**(5): p. 991-998.
182. !!! INVALID CITATION !!! [160].
183. Prochazka, V., et al., *The Role of von Willebrand Factor, ADAMTS13, and Cerebral Artery Thrombus Composition in Patient Outcome Following Mechanical Thrombectomy for Acute Ischemic Stroke.* Med Sci Monit, 2018. **24**: p. 3929-3945.
184. Gunning, G.M., et al., *Clot friction variation with fibrin content; implications for resistance to thrombectomy.* J Neurointerv Surg, 2018. **10**(1): p. 34-38.
185. Bang, O.Y., et al., *Endovascular Therapy for Acute Ischemic Stroke of Intracranial Atherosclerotic Origin-Neuroimaging Perspectives.* Front Neurol, 2019. **10**: p. 269.
186. Maegerlein, C., et al., *Impact of histological thrombus composition on preinterventional thrombus migration in patients with acute occlusions of the middle cerebral artery.* Interv Neuroradiol, 2018. **24**(1): p. 70-75.
187. Gersh, K.C., C. Nagaswami, and J.W. Weisel, *Fibrin network structure and clot mechanical properties are altered by incorporation of erythrocytes.* Thromb Haemost, 2009. **102**(6): p. 1169-75.
188. Mokin, M., et al., *Thrombus density predicts successful recanalization with Solitaire stent retriever thrombectomy in acute ischemic stroke.* J Neurointerv Surg, 2015. **7**(2): p. 104-7.
189. Spiotta, A.M., et al., *Hounsfield unit value and clot length in the acutely occluded vessel and time required to achieve thrombectomy, complications and outcome.* J Neurointerv Surg, 2014. **6**(6): p. 423-7.
190. Jagani, M., D.F. Kallmes, and W. Brinjikji, *Correlation between clot density and recanalization success or stroke etiology in acute ischemic stroke patients.* Interv Neuroradiol, 2017. **23**(3): p. 274-278.
191. Seker, F., et al., *Correlation of Thrombectomy Maneuver Count with Recanalization Success and Clinical Outcome in Patients with Ischemic Stroke.* AJNR Am J Neuroradiol, 2017. **38**(7): p. 1368-1371.
192. Leischner, H., et al., *Reasons for failed endovascular recanalization attempts in stroke patients.* J Neurointerv Surg, 2019. **11**(5): p. 439-442.
193. Rha, J.H. and J.L. Saver, *The impact of recanalization on ischemic stroke outcome: a meta-analysis.* Stroke, 2007. **38**(3): p. 967-73.
194. Nie, X., et al., *Futile Recanalization after Endovascular Therapy in Acute Ischemic Stroke.* Biomed Res Int, 2018. **2018**: p. 5879548.
195. Fransen, P.S., et al., *Time to Reperfusion and Treatment Effect for Acute Ischemic Stroke: A Randomized Clinical Trial.* JAMA Neurol, 2016. **73**(2): p. 190-6.
196. Khatri, P., et al., *Good clinical outcome after ischemic stroke with successful revascularization is time-dependent.* Neurology, 2009. **73**(13): p. 1066-72.
197. Mazighi, M., et al., *Impact of onset-to-reperfusion time on stroke mortality: a collaborative pooled analysis.* Circulation, 2013. **127**(19): p. 1980-5.
198. Sun, C.H., et al., *Door-to-puncture: a practical metric for capturing and enhancing system processes associated with endovascular stroke care, preliminary results from the rapid reperfusion registry.* J Am Heart Assoc, 2014. **3**(2): p. e000859.

199. Sun, C.H., et al., *"Picture to puncture": a novel time metric to enhance outcomes in patients transferred for endovascular reperfusion in acute ischemic stroke.* Circulation, 2013. **127**(10): p. 1139-48.
200. Hedna, V.S., et al., *Hemispheric differences in ischemic stroke: is left-hemisphere stroke more common?* J Clin Neurol, 2013. **9**(2): p. 97-102.
201. Foerch, C., et al., *Difference in recognition of right and left hemispheric stroke.* Lancet, 2005. **366**(9483): p. 392-3.
202. Portegies, M.L., et al., *Left-sided strokes are more often recognized than right-sided strokes: the Rotterdam study.* Stroke, 2015. **46**(1): p. 252-4.
203. Cho, B.H., et al., *Associations of various blood pressure parameters with functional outcomes after endovascular thrombectomy in acute ischaemic stroke.* Eur J Neurol, 2019. **26**(7): p. 1019-1027.
204. Malhotra, K., et al., *Association of Elevated Blood Pressure Levels with Outcomes in Acute Ischemic Stroke Patients Treated with Intravenous Thrombolysis: A Systematic Review and Meta-Analysis.* J Stroke, 2019. **21**(1): p. 78-90.
205. Ota, T., et al., *Impact of onset-to-groin puncture time within three hours on functional outcomes in mechanical thrombectomy for acute large-vessel occlusion.* Interv Neuroradiol, 2018. **24**(2): p. 162-167.
206. Madsen, T.E., et al., *Sex differences in 90-day outcomes after mechanical thrombectomy for acute ischemic stroke.* J Neurointerv Surg, 2019. **11**(3): p. 221-225.
207. Nawabi, J., et al., *Hemorrhage After Endovascular Recanalization in Acute Stroke: Lesion Extent, Collaterals and Degree of Ischemic Water Uptake Mediate Tissue Vulnerability.* Front Neurol, 2019. **10**: p. 569.
208. Mistry, E.A., A.M. Mistry, and M.R. Fusco, *Response by Mistry et al to Letter Regarding Article, "Mechanical Thrombectomy Outcomes With and Without Intravenous Thrombolysis in Stroke Patients: A Meta-Analysis".* Stroke, 2017. **48**(11): p. e334.
209. Myint, P.K., et al., *Prior Antithrombotic Use Is Associated With Favorable Mortality and Functional Outcomes in Acute Ischemic Stroke.* Stroke, 2016. **47**(8): p. 2066-74.
210. Xian, Y., et al., *Association of Preceding Antithrombotic Treatment With Acute Ischemic Stroke Severity and In-Hospital Outcomes Among Patients With Atrial Fibrillation.* Jama, 2017. **317**(10): p. 1057-1067.
211. Valberg, L.S., et al., *SPECTROCHEMICAL ANALYSIS OF SODIUM, POTASSIUM, CALCIUM, MAGNESIUM, COPPER, AND ZINC IN NORMAL HUMAN ERYTHROCYTES.* J Clin Invest, 1965. **44**: p. 379-89.
212. Kiem, J., et al., *Elemental composition of platelets. Part II. Water content of normal human platelets and measurements of their concentrations of Cu, Fe, K, and Zn by neutron activation analysis.* Clin Chem, 1979. **25**(5): p. 705-10.
213. Makino, T., *K, Ca, Mg, and Zn in platelets, as determined by atomic absorption spectrometry with use of a sealed decomposition bomb and discrete nebulization.* Clin Chem, 1985. **31**(4): p. 609-12.
214. Henderson, S.J., et al., *Zinc promotes clot stability by accelerating clot formation and modifying fibrin structure.* Thromb Haemost, 2016. **115**(3): p. 533-42.
215. Chen, H., et al., *Oxidative stress in ischemic brain damage: mechanisms of cell death and potential molecular targets for neuroprotection.* Antioxid Redox Signal, 2011. **14**(8): p. 1505-17.

216. Gu, S.X., J.W. Stevens, and S.R. Lentz, *Regulation of thrombosis and vascular function by protein methionine oxidation.* Blood, 2015. **125**(25): p. 3851-9.
217. Miglis, M., et al., *Effect of taurine on platelets and the plasma coagulation system.* Platelets, 2002. **13**(1): p. 5-10.
218. Jin, R., et al., *Taurine Reduces tPA (Tissue-Type Plasminogen Activator)-Induced Hemorrhage and Microvascular Thrombosis After Embolic Stroke in Rat.* Stroke, 2018. **49**(7): p. 1708-1718.
219. Hayes, K.C., et al., *Taurine modulates platelet aggregation in cats and humans.* Am J Clin Nutr, 1989. **49**(6): p. 1211-6.
220. Santos, E.M., et al., *Thrombus Permeability Is Associated With Improved Functional Outcome and Recanalization in Patients With Ischemic Stroke.* Stroke, 2016. **47**(3): p. 732-41.
221. Chen, Z., et al., *Thrombus Permeability on Dynamic CTA Predicts Good Outcome after Reperfusion Therapy.* AJNR Am J Neuroradiol, 2018. **39**(10): p. 1854-1859.
222. Dutra, B.G., et al., *Thrombus Imaging Characteristics and Outcomes in Acute Ischemic Stroke Patients Undergoing Endovascular Treatment.* Stroke, 2019. **50**(8): p. 2057-2064.
223. Berndt, M., et al., *Thrombus Permeability in Admission Computed Tomographic Imaging Indicates Stroke Pathogenesis Based on Thrombus Histology.* Stroke, 2018. **49**(11): p. 2674-2682.
224. Wohner, N., et al., *Lytic resistance of fibrin containing red blood cells.* Arterioscler Thromb Vasc Biol, 2011. **31**(10): p. 2306-13.